

The Discovery and Characterization of a Novel Family of Anti-Cancer Compounds

Dilan Boodhai Jaunky

A Thesis

In the Department

of

Biology

Presented in Fulfilment of the Requirements

For the Degree of

Doctor of Philosophy in Biology at Concordia University

Montreal, Quebec, Canada

September 2020

© Dilan Boodhai Jaunky, 2020

CONCORDIA UNIVERSITY
SCHOOL OF GRADUATE STUDIES

This is to certify that the thesis prepared

By: Dilan Boodhai Jaunky

Entitled: The Discovery and Characterization of a Novel Family of Anti-Cancer Compounds

and submitted in partial fulfillment of the requirements for the degree of

Doctor Of Philosophy (Biology)

complies with the regulations of the University and meets the accepted standards with respect to originality and quality.

Signed by the final examining committee:

Dr. Jennifer McGrath Chair

Dr. Adam Hendricks External Examiner

Dr. Paul Joyce External to Program

Dr. Michael Sacher Examiner

Dr. Vladimir Titorenko Examiner

Dr. Alisa Piekny Thesis Supervisor

Approved by

Dr. Robert Weladji, Graduate Program Director

November 5, 2020

Dr. Pascale Sicotte, Dean
Faculty of Arts and Science

Abstract

The Discovery and characterization of a novel family of anti-cancer compounds

Dilan Boodhai Jaunky, Ph.D.

Concordia University, 2020

Cancer is amongst the leading causes of death in the world and has plagued humanity for far longer than some would expect. We have come a long way in understanding the physiological changes that correlate with cancer progression, but treatment options remain limited. In this thesis, I developed a high-throughput pipeline to screen thienoisouquinoline derivatives synthesized by Dr. Forgione's laboratory for their efficacy in reducing cancer cell viability. These derivatives were strategically designed to share a common scaffold and have three functional groups amenable to modifications. From >40 derivatives, we identified our lead compound C75. We characterized the mechanism of action of C75 at a molecular and cellular level to develop a better understanding of its efficacy, and selectivity for some cell types over others. Through in vitro assays, we found that C75 prevents microtubule polymerization, destabilizes microtubules, and binds to tubulin at the same site as colchicine (another microtubule-targeting drug). In line with its effects on microtubules, C75 causes mitotic arrest and spindle phenotypes in multiple cancer cell lines in the nanomolar range. However, through comparative studies with colchicine, we found that while colchicine causes a gradual decrease in microtubules and spindle pole collapse in cells, similar concentrations of C75 cause a rapid loss of microtubules and spindle pole fragmentation followed by microtubule re-growth to form multipolar spindles. In addition, C75 and colchicine synergize for reduced viability and spindle phenotypes. Importantly, the phenotypes caused by C75 are similar to those caused by the depletion of ch-TOG, a microtubule polymerase, and tubulin and

ch-TOG are displaced and oscillate in C75-treated cells. This suggests that C75 directly causes microtubule depolymerization in cells, or indirectly causes this via inhibiting ch-TOG. We also discovered that C75 has higher efficacy in triple negative breast cancer (TNBC) cells compared to other cell types, suggesting that this could be an ideal group of cancers to explore a potential use for. It will be important to determine if C75 retains its efficacy in TNBCs that are resistant to Taxol, which arises in patients after repeated Taxol use leaving them with few alternative treatment options. We also identified a new derivative that has even higher efficacy in TNBCs compared to C75, and we are determining if this will be a new lead compound. With a strong understanding of how these compounds work at the molecular and cellular level, we are positioned to carry out *in vivo* studies to determine their potential for use for treating TNBCs.

Acknowledgements

I would like to thank Dr. Alisa Piekny for being a great mentor and supervisor during the course of my graduate studies. I started in your lab doing my undergraduate thesis project and since then have developed a whole new way of thinking critically and understanding the scientific method. You have without a doubt been a major influence in my education and in the completion of my PhD, and for that I am truly grateful. I would also like to thank Dr. Michael Sacher and Dr. Vladimir Titorenko for following my progress throughout my graduate studies and for their invaluable feedback.

I would like to give thanks to Dr. Chloë van Oostende and Dr. Chris Law who trained me in microscopy and were always patient and insightful. You both have made my experience with the Center of Microscopy and Cellular Imaging a fulfilling one.

A lot of great memories were made over the years with my fellow lab mates. It has definitely enhanced my experience during my studies. To Karina, Danny and Samantha, you guys are the best and I hope one day we all get to realize our little agreement of working together once again (JSMB). I would like to thank the remaining members of the Piekny lab for your time and feedback you have given me over the years.

I'd like to give a special thanks to two other teachers, Maurille St-Louis and Emmanuel St-Louis who thought me discipline and focus during my years of practicing martial arts. The lessons learnt during those times have grounded me through good and bad times and will never be forgotten.

I'd like to thank my parents for all of their love and support during my degree, you've always known how to keep me motivated and enabled all of my many pursuits throughout my life. I'd like to also thank Vinesh and Brandon for your support and for being the brothers I am proud

to celebrate this achievement with. I'd also like to tip my hat to my "other half" and a great friend Dr. Younes Medkour. We've come a long way since we were kids at our dojo and we've always enjoyed challenging one another since then. As a response to your message to me in your thesis; I don't know what we will tackle next but I'm sure it'll be another memorable one for the books. Still thinking of going to medical school?

Dedications

I'd like to dedicate this thesis to my mother, Haemwatee Boodhai, you were my first teacher, and this body of work serves as a testament to how great of a teacher you were and still are. You are my drive and my motivation, thank you for instilling passion in everything that I am. I'd also like to dedicate this thesis to my father, Horil Jaunky, you've thought me how to be a problem solver and to apply thought before action. You've both guided and encouraged me to always become a better version of my previous self and to always persevere. I love you both.

Contribution of Authors

Figure 9. Christian Sanchez-Espinoza built the software and the workflow for the GUI.

Figure 10. The compounds were synthesized in Dr. Pat Forgione's lab. Jiang Tian Liu provided the chemical structures for each derivative and their cLogP values. Matthew Collard helped to screen the compounds to determine their IC₅₀ in A549 cells.

Figure 13. Kevin Larocque performed the microtubule polymerization assay shown in B.

Figure 14. Sajinth Thampipillai performed the microtubule destabilization assay shown in A.

Kevin Larocque and Sajinth Thampipillai performed the C75 competition assay with colchicine shown in B and C.

Figure 16. Dan Yang helped to count the proportion of mitotic cells shown in A. Mathieu Husser performed the experiment shown in B and C. Kevin Larocque performed the experiment in D.

Figure 18. Mathieu Husser performed the experiments.

Figure 24. Christian Sanchez-Espinoza performed the experiments in A and B.

Figure 25. Matthew Collard helped perform the viability assays in B.

Figure 26. Christian Sanchez-Espinoza helped in making the paclitaxel-resistant cell lines in A.

Table of Contents

LIST OF FIGURES.....	XIII
LIST OF ABBREVIATIONS	XV
CHAPTER 1: INTRODUCTION	1
1.1 CANCER'S FOOTPRINT.....	1
<i>1.1.1 A historical perspective</i>	1
<i>1.1.2 Global overview and statistics.....</i>	2
<i>1.1.3 How to move forward</i>	2
1.2 THE INTRICACIES OF CELL DIVISION	5
<i>1.2.1 Cell Cycle</i>	5
<i>1.2.2 Mitotic regulation.....</i>	8
<i>1.2.3 Mitotic spindle – centrosomes and microtubules</i>	12
<i>1.2.4 The Spindle Assembly Checkpoint (SAC)</i>	23
1.3 WHEN A HEALTHY CELL LOSES ITS WAY	28
<i>1.3.1 Hallmarks of cancer</i>	28
<i>1.3.2 Loss of controlled cell proliferation.....</i>	28
<i>1.3.3 Genetic Changes that affect mitotic spindles</i>	30
<i>1.3.4 Chemotherapy – microtubule targeting agents</i>	32

1.3.4.1 Taxol	33
1.3.4.2 Vinblastine.....	35
1.3.4.3 Colchicine.....	36
<i>1.3.5 Resistance to Chemotherapy</i>	39
1.4 DRUG DISCOVERY	40
<i>1.4.1 The need to find new drugs.....</i>	40
<i>1.4.2 “Bottom-up” approach to drug discovery</i>	40
<i>1.4.3 “Top down” approach to drug discovery</i>	41
1.4.3.1 Summary of thesis objectives.....	42
CHAPTER 2: MATERIAL AND METHODS	44
2.1 CELL CULTURE.....	44
2.2 DRUG TREATMENTS.....	44
2.3 VIABILITY ASSAYS.....	45
2.4 MICROTUBULE ASSAYS	45
2.5 FLOW CYTOMETRY	46
2.6 IMMUNOFLUORESCENCE STAINING	47
2.7 MICROSCOPY	48
2.8 ANALYSIS	49
2.9 METABOLISM PROFILE OF C75.....	52

2.10 DEVELOPING TAXOL-RESISTANT CELL LINES	52
2.11 ILLUSTRATIONS AND CARTOON SCHEMATICS	53
CHAPTER 3: DISCOVERING A NOVEL ANTI-CANCER COMPOUND	54
3.1 DEVELOPING A HIGH-THROUGHPUT SCREENING (HTS) PIPELINE	54
3.2 DETERMINING DERIVATIVES THAT AFFECT THE VIABILITY OF CANCER CELLS.....	64
3.3 CHARACTERIZING THE ANTI-CANCER PROPERTIES OF C75	72
CHAPTER 4: A NOVEL COMPOUND THAT DISRUPTS MITOTIC SPINDLE POLES IN HUMAN CELLS	79
4.1 PREAMBLE	79
4.2 COMPOUND 75 CAUSES CELLS TO ARREST IN G2/M PHASE	80
4.3 C75 CAUSES SPINDLE POLE PHENOTYPES	88
4.4 COMBINING C75 AND COLCHICINE ENHANCE SPINDLE PHENOTYPES.....	91
4.5 C75 AND COLCHICINE HAVE DIFFERENT EFFECTS ON MICROTUBULE POLYMERS IN CELLS	97
CHAPTER 5: CHARACTERIZING THE <i>IN VIVO</i> POTENTIAL OF C75.....	109
5.1 IDENTIFYING TNBCs AS A TARGET CANCER FOR C75	109
5.2 EFFICACY OF C75 IN TAXOL-RESISTANT TNBCs	117
5.3 DETERMINING THE CHANGES IN METABOLIC ENZYMES AFTER C75 TREATMENT.....	123
5.4 FINDING NEW LEAD COMPOUNDS	127

CHAPTER 6: DISCUSSION.....	131
6.1 SUMMARY.....	131
6.2 DEVELOPING HIGH-THROUGHPUT METHODOLOGY	132
6.3 DETERMINING C75'S MECHANISM OF ACTION IN CELLS	134
6.4 EXPLORING THE POTENTIAL OF OUR NEW COMPOUNDS FOR IN VIVO USE TO TREAT TNBCs	137
6.5 CONCLUSIONS.....	140
REFERENCES	142

List of Figures

Figure 1. Cancer statistics on a global scale.

Figure 2. The cell cycle.

Figure 3. The microtubule organizing center (MTOC) in mammalian somatic cells.

Figure 4. Microtubule dynamics.

Figure 5. The spindle assembly checkpoint (SAC).

Figure 6. The chemical structures of well-known microtubule targeting agents (MTAs).

Figure 7. Low-throughput workflow to determine cell viability.

Figure 8. High-throughput workflow to determine cell viability.

Figure 9. An overview of the GUI design to organize images.

Figure 10. Structures show the thienoisoquinoline derivatives synthesized for this study.

Figure 11. C75 causes HeLa cells to arrest in mitosis with disorganized spindles.

Figure 12. C75 causes mitotic spindle phenotypes in a broad range of cells and causes spindle pole fragmentation.

Figure 13. C75 is a thienoisoquinoline compound that causes G2/M arrest in cultured human cells.

Figure 14. C75 depolymerizes microtubules and competes with colchicine for tubulin-binding *in vitro*.

Figure 15. C75 causes cultured human cells to arrest in G2/M.

Figure 16. C75 causes cells to arrest in mitosis with multipolar spindles.

Figure 17. Combining C75 with colchicine enhances lethality and shows a synergistic interaction.

Figure 18. Combining C75 with colchicine enhances spindle phenotypes in HeLa and HCT 116 cells.

Figure 19. C75 and colchicine cause different spindle phenotypes.

Figure 20. Microtubules and spindle poles recover in the presence of C75.

Figure 21. Spindle poles recover in the presence of C75.

Figure 22. ch-TOG knockdown phenocopies C75, and ch-TOG oscillates in C75-treated cells.

Figure 23. C75 has high efficacy for TNBCs and causes multipolar spindles to form in MDA-MB-231 cells.

Figure 24. C75 causes mitotic phenotypes in Hs578t cells.

Figure 25. A subthreshold dose of C75 lowers the IC₅₀ for paclitaxel in different cell lines.

Figure 26. Paclitaxel resistant cell lines.

Figure 27. Metabolite profiles of C75.

Figure 28. Identifying C140 as a new lead compound.

List of Abbreviations

γ -TuRC	gamma-Tubulin Ring Complex
a.u.	Arbitrary Units
ACA	Anti-Centromere Antibody
APC	Anaphase Promoting Complex
BCRP	Breast Cancer Resistance Protein
CDK	Cyclin Dependent Kinase
Ch-TOG	Colonic and Hepatic Tumor Overexpressed Gene
CI	Combination Index
CIN	Chromosomal Instability Index
CLogP	Calculated Logarithm Partition Coefficient
DMSO	Dimethyl Sulfoxide
DOI	Declaration of Invention
Eg5	Kinesin-5 motor protein
EGF	Epithelial Growth Factor
ER	Estrogen Receptor
FBS	Fetal Bovine Serum
FDA	Food and Drug Administration
GAP	GTPase-Activating Proteins
GDP	Guanine Diphosphate
GEF	Guanine Exchange Factor
GTP	Guanine Triphosphate
GUI	Graphical User Interface

HEAT	Huntingtin, Elongation Factor 3, Protein Phosphatase 3A, Target of Rapamycin 1
HER2	Human Epidermal Growth Factor Receptor 2
HLM	Human Liver Microsomes
HTS	High-Throughput Screening
IARC	International Agency for Research on Cancer
ILK	Integrin-Linked Kinase
KIF2C	Kinesin family member 2C (or MCAK)
LDV	Low Dead Volume
LINC	Linker of Nucleocytoskeleton and Cytoskeleton
MAD	Mitotic Arrest Deficient
MAP	Microtubule Associated Proteins
MCAK	Mitotic Centromere-Associated Kinesin
MCC	Mitotic Checkpoint Complex
MEK	Mitogen-Activated Protein Kinase
MLM	Mice Liver Microsomes
MRP1	Multidrug-Resistant Protein-1
MRP8	Multidrug-Resistant Protein-8
MT	Microtubule
MTA	Microtubule Targeting Agent
NCI	National Cancer Institute
NE	Nuclear Envelop
NEBD	Nuclear Envelop Breakdown
NPC	Nuclear Pore Complex

NSCLC	Non-Small Cell Lung Cancer
PAGE	Polyacrylamide Gel Electrophoresis
PBS	Phosphate Buffer Solution
PCD	Programmed Cell Death
PCM	Pericentriolar Material
PCNT	Pericentrin
PD	Pharmacodynamic
PDT	Population Doubling Time
PI	Propidium Iodide
PK	Pharmacokinetic
Plk1	Polo-like Kinase 1
Plk4	Polo-like Kinase 4
PP2A	Protein Phosphatase 2A
PR	Progesterone Receptor
RAF	Rapidly Accelerated Fibrosarcoma
RCC1	Regulator of Chromosome Condensation 1
S&C	Search and Capture
SAC	Spindle Assembly Complex
SD	Standard Deviation
SEM	Standard Error of the Mean
siRNA	Short Interfering Ribonucleic Acids
TACC3	Transforming Acidic Coiled-Coil Protein 3
TCA	Trichloroacetic Acid

TNBC	Triple Negative Breast Cancer
TPX2	Targeting Protein for Xkhp2
USDA	United States Department of Agriculture
VA	Vinca Alkaloid
VBL	Vinblastine
WHO	World Health Organization

Chapter 1: Introduction

1.1 Cancer's footprint

1.1.1 A historical perspective

While we have made significant progress learning the molecular, cellular and physiological changes that arise during cancer progression, this ailment has plagued humanity for far longer than some would imagine. Cancer was first described in the Edwin Smith Papyrus, dating back to 3000 BC (**Johnson 1948**). This earliest known documentation described a disease that produced a bulge on the breast and was deemed to have no effective treatment. Various forms of treatments were devised and improvised under the name “Egyptian ointment”, often involving cautery (the fire drill), knives, salt and arsenic paste (**Johnson 1948**). Over time, other cancers were documented, and these descriptions contribute to our holistic understanding of what comprises cancer. With years of research, we have gained extensive knowledge of the genetic changes that arise in cancers and have identified those that may be more causative vs. correlative. This has led to the development of targeted therapies with improved outcomes, and multi-pronged approaches to minimize side-effects and resistance. We have also made significant advancements in developing diagnostic tools and screening programs for early detection, particularly for breast, colorectal and prostate cancers, which has reduced the mortality caused by these cancers. However, despite these advances, there are a limited number of therapies for most cancers, and patients can gain resistance to these therapies leaving them with few treatment options. Thus, there is a need to broaden the repertoire of anti-cancer drugs.

1.1.2 Global overview and statistics

Cancer has made an impact on our lives in one way or another. According to the International Agency for Research on Cancer (IARC) and World Health Organization (WHO), 18,078,957 individuals around the world were diagnosed with some form of cancer in 2018, and 9,555,027 lives were lost to the disease (**Figure 1A, B; Bray et al. 2018; Ferlay et al. 2019**). These gruesome numbers place cancer as the second leading cause of death globally, with every 1 in 6 deaths due to cancer (**Bray et al. 2018; Ferlay et al. 2019**). The most prevalent cancers for men and women are lung, colorectal, and prostate (men) or breast (women) cancers (**Figure 1C**). In Canada, an estimated 1 in 2 people will be diagnosed with cancer at some point in their lifetime, and 1 in 4 will die from cancer (**Smith et al. 2018, Canadian Cancer Statistics Report 2019**). In addition to the loss of life, cancer causes severe repercussions on a patient's quality of life and imposes a heavy financial cost to society. The estimated cost for treating cancer in Canada has risen from \$2.9 Billion in 2005 to \$7.9 Billion in 2012, with chemotherapy and radiotherapy contributing the most to this increase (**Oliveira et al. 2018**). Thus, there is a need to search for novel treatments and solutions to improve patient care and decrease the overall financial burden cancer places on society.

1.1.3 How to move forward

The way to find new anti-cancer drugs is to harness the physiological changes that arise in cancers, as a means of selectively targeting these cells, and reducing their effect on healthy cells. As outlined by Hanahan and Weinberg (2011), most cancers acquire certain hallmarks over time, which allows them to progress to a metastatic state (**Hanahan and Weinberg 2011**).

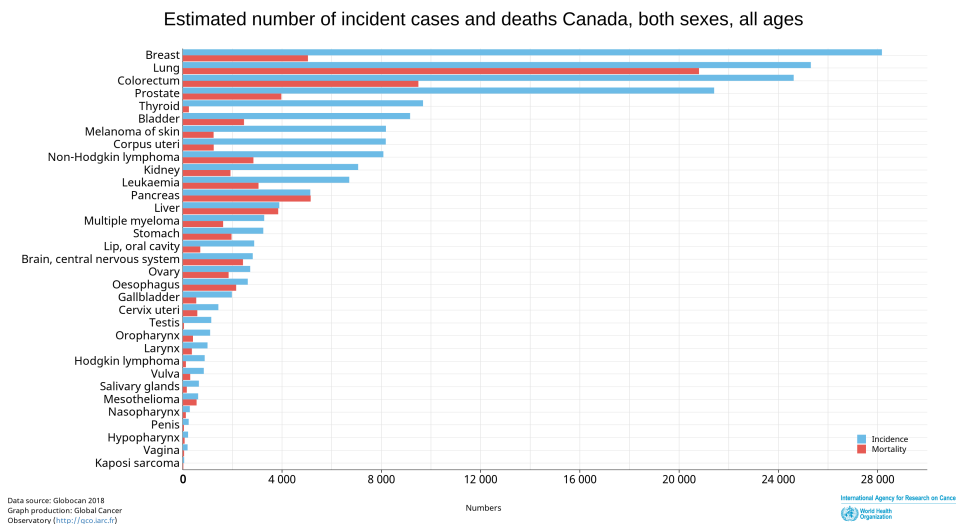
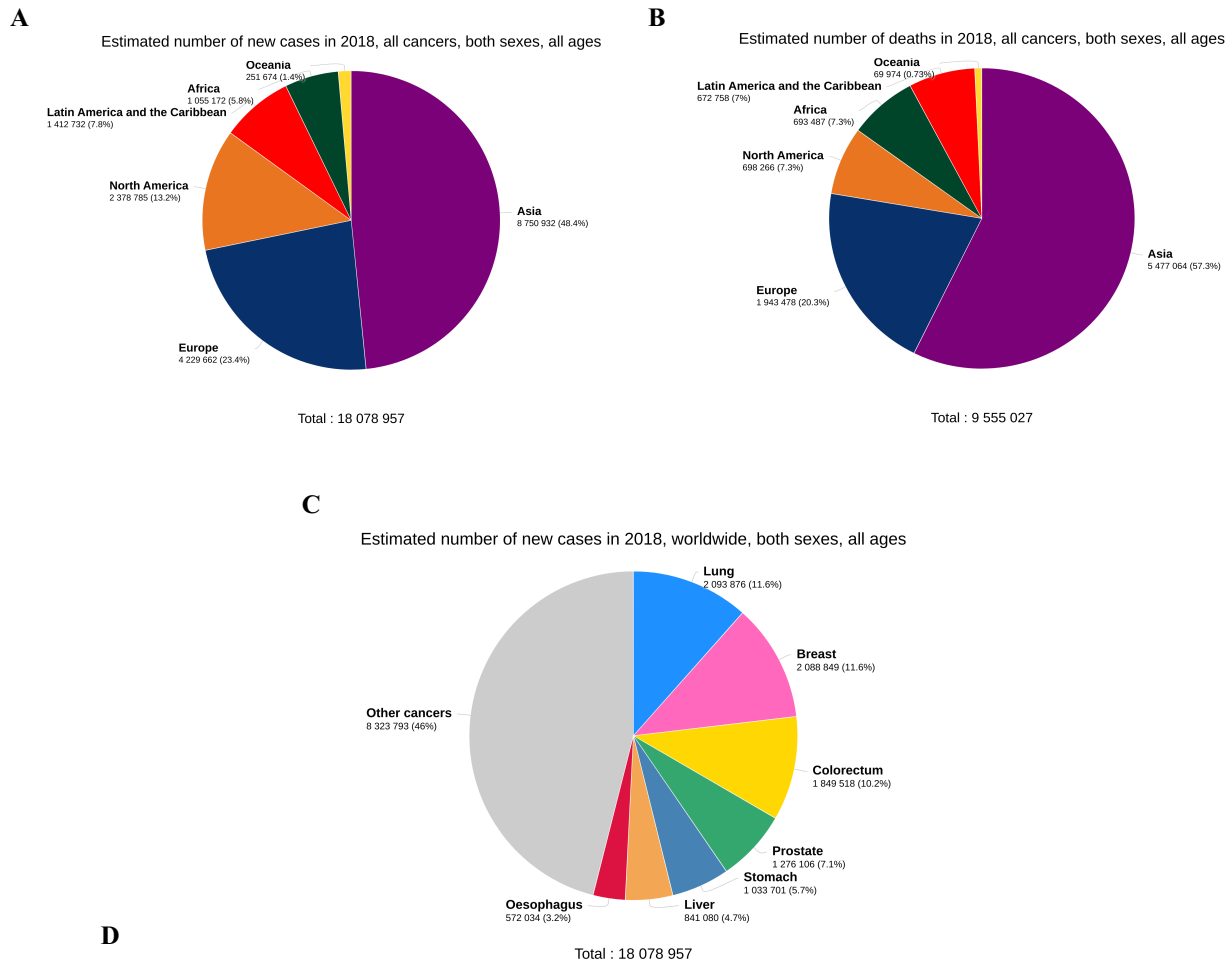


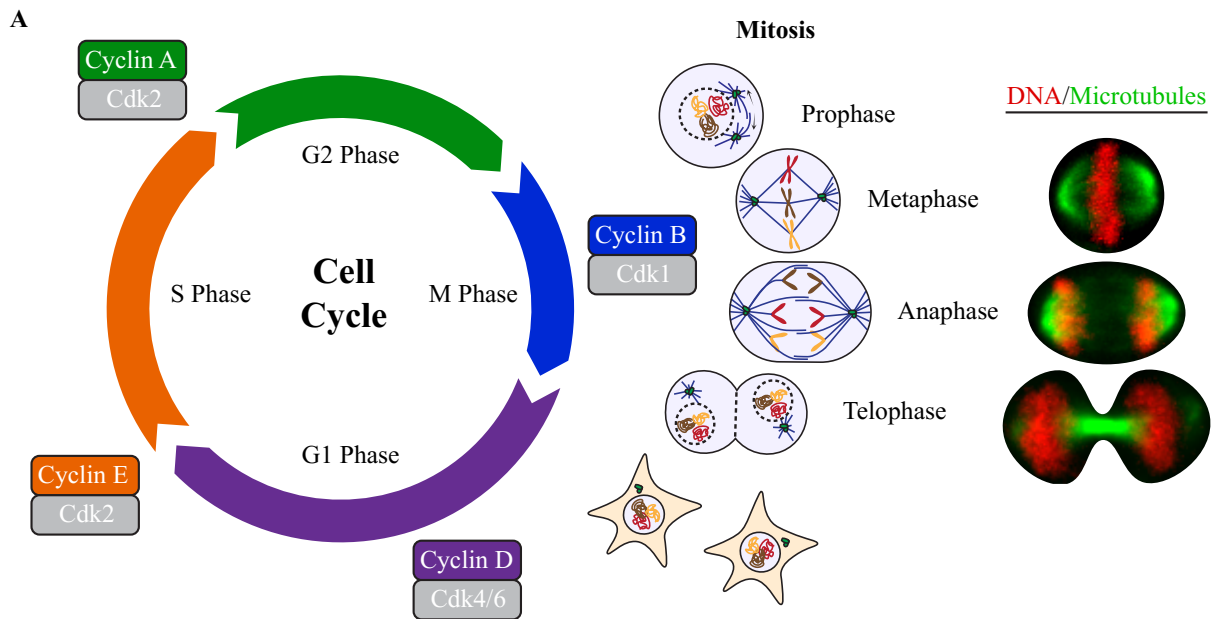
Figure 1. Cancer statistics on a global scale. A) A pie chart shows the estimation of new cases for all cancers in both sexes and all ages in 2018. B) A pie chart shows the estimated number of deaths for all cancers in both sexes and all ages in 2018. C) A chart shows the breakdown of the types of cancers estimated in both sexes and all ages in 2018. D) A bar graph shows the breakdown of the incidence and deaths for each cancer across both sexes and all ages in Canada. Data were obtained from Bray et al. 2018 and Ferlay et al. 2019, and the illustrations were obtained from the Global Cancer Observatory (GCO; Ferlay et al. 2018).

While we discuss some of these hallmarks further in section 1.3, one particular hallmark they possess is the ability to proliferate in an uncontrolled manner, regardless of the presence of cell cycle entry cues. As such, some of the most successful chemotherapies that are still in use today block various stages of the cell cycle and reduce the proliferative capacity of cancer cells. While not selective per se, they tend to more strongly affect the rapidly dividing cancer cells compared to the quiescent or more slowly dividing healthy cells. The development of future therapies should continue to exploit these differences, but with improved drug design as discussed in section 1.4, they can be made to have improved selectivity over existing therapies.

1.2 The intricacies of cell division

1.2.1 Cell Cycle

Cell division is crucial for the development and homeostasis of tissues, and all metazoan cells rely on a highly controlled cell cycle to divide. The cycle is comprised of four phases; Gap 1 (G1) where cells grow and prepare to divide in response to external cues, Synthesis (S) where the genomic content is replicated to create sister chromatid pairs, Gap 2 (G2) where cells prepare for mitotic entry, and Mitotic (M) phase where cells build spindles that attach to and separate sister chromatids, and signal to the overlying cortex to form a contractile ring that physically separates the daughter cells during cytokinesis (**Figure 2A**). Each stage of the cell cycle is tightly controlled by distinct Cyclin-dependent kinase (Cdk)/Cyclin complexes (**Figure 2A, B**). The activity of these complexes is controlled by an increase in Cyclin levels and/or enzymatic regulation, followed by the removal of that particular Cyclin by its destruction. For example, cell cycle entry into G1 occurs due to an increase in the levels of Cyclin D, which forms a complex with Cdk4,6. This complex is soon replaced by Cyclin E/Cdk2, which commits cells to the cell cycle at the G1/S phase transition



B

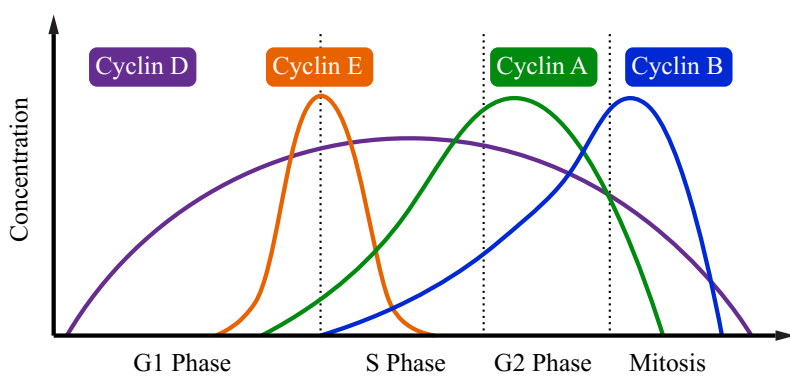


Figure 2. The cell cycle. A) The phases of the mammalian cell cycle are shown with the corresponding cyclins and CDKs required for each phase (left). Cartoon schematics show cells in the different stages of mitosis, from prometaphase to telophase. The microtubules are in blue, the chromosomes are in red, yellow and brown. Images show HeLa cells co-stained for tubulin to visualize microtubules (green) and DAPI to visualize chromatin (DNA; red) in metaphase (top), anaphase (middle) and telophase (bottom). B) A graphical representation shows the changes in cyclin levels as cells progress through the cell cycle.

(Poon 2016; Martínez-Alonso and Malumbres 2020). Due to their intrinsic role in cell cycle commitment, they are carefully controlled by several inhibitors including p16^{INK4}, p21^{CIP1}, and p27^{KIP1} (Poon 2016; Martínez-Alonso and Malumbres 2020). Cyclin D and E levels rise in response to Ras activation, which upregulates the transcription of early and late response genes (Poon 2016; Martínez-Alonso and Malumbres 2020). The Cyclin E/Cdk2 complex, and subsequently the Cyclin A/Cdk2 complex, regulate the replication machinery to generate copies of the genome, and to regulate centrosome biogenesis (Martínez-Alonso and Malumbres 2020). S phase complexes are replaced by the Cyclin A/Cdk1 complex that increases in G2 phase, and mediates entry into M phase, and is closely followed by the Cyclin B/Cdk1 complex (Poon 2016; Martínez-Alonso and Malumbres 2020). Their activities are tightly regulated by several enzymes. Cells exit from mitosis when the levels of Cdk1 activity drop due to Cyclin B degradation, and only re-enter the cell cycle when sufficient levels of active Cyclin D/Cdk4, 6 complexes form again (Poon 2016; Martínez-Alonso and Malumbres 2020). This tight regulation ensures an irreversible commitment, and that cells always progress from one stage to the next in a similar way. Any problems that arise will trigger checkpoints that arrest cells at various stages of the cycle.

1.2.2 Mitotic regulation

Mitosis consists of several phases, starting from prophase/prometaphase, transitioning into metaphase, then exiting into anaphase, and telophase followed by cytokinesis (Figure 2A). Mitotic entry is carefully controlled by several regulators of Cyclin A, B/Cdk1 activity, as well as enzymes that initiate DNA condensation, nuclear envelope breakdown and increase microtubule dynamics in preparation for mitotic spindle assembly. Prior to prometaphase, Cyclin B/Cdk1 is kept inactive

by inhibitory phosphorylation via Myt1 and Wee1 tyrosine kinases. At the G2/M transition, these inhibitory phosphates are removed by Cdc25 phosphatase, which generates a positive feedback loop, as Cyclin B/Cdk1 can phosphorylate and inhibit Myt1 and Wee1 (**Poon 2016**). This increase in Cdk1 activity promotes mitotic entry via the regulation of substrates required for chromosome condensation, nuclear envelope breakdown (NEBD), centrosome separation and microtubule nucleation.

The process of nuclear envelope breakdown (NEBD) is essential for microtubules to effectively access the chromatin for alignment at the equatorial plane in metazoans (**Ungricht and Kutay 2017**). NEBD is mediated in part by attachment of the nuclear pore complexes (NPCs) to dynein motors, which generate force via astral microtubules to move the associated complexes apart (**Figure 3B; Ungricht and Kutay 2017**). The force generated by the dynein motors also contributes to invagination of the nuclear envelope (NE), which is facilitated by degradation of the “linker of nucleocytoskeleton and cytoskeleton” (LINC) complexes that tethers the NE to the cytoskeleton (**Ungricht and Kutay 2017**). This also frees connections between the NE and chromatin so that the NE-ER membrane network is spatially distanced from the mitotic spindle (**Ungricht and Kutay 2017**). Aurora A kinase is also activated at the G2/M transition and promotes centrosome maturation via the phosphorylation and activation of polo-like kinase 1 (Plk1). As centrosomes build pericentriolar material and initiate microtubule growth in prometaphase, they disengage and begin to separate via the action of the Eg5 kinesin motor. This action also helps pull apart the disassembling nuclear envelope (**Figure 3 A, B, C**).

As cells progress through mitosis, the sister chromatids also go through several changes to prepare them for alignment and segregation. During prophase, the chromosomes condense via the compaction of DNA around histone octamers giving rise to the clearly defined units of chromatin

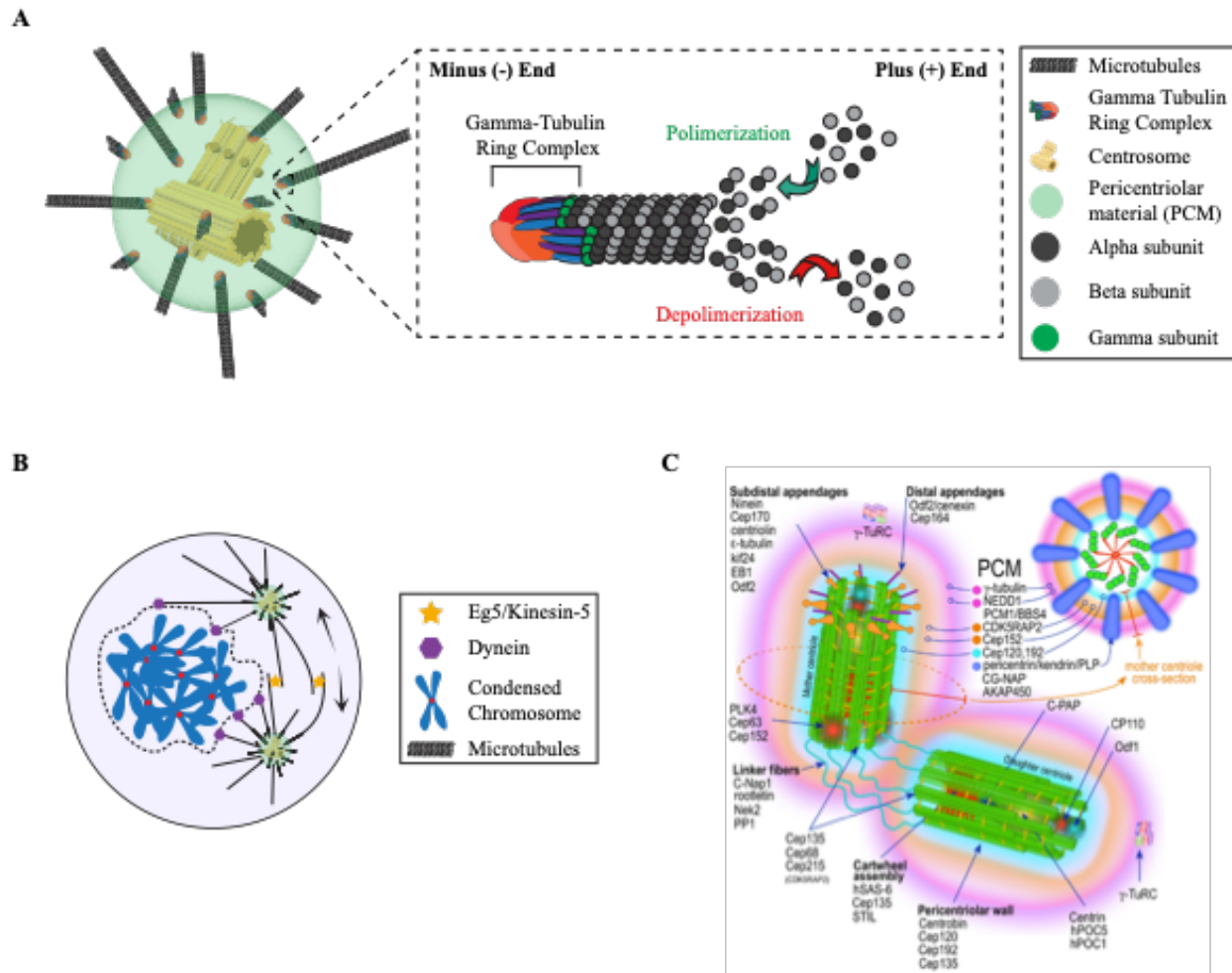


Figure 3. The microtubule organizing center (MTOC) in mammalian somatic cells. **A)** A cartoon model shows the centrosome surrounded by its pericentriolar material (PCM) from which microtubules emanate. The cartoon inset shows how the minus end is organized to allow for the microtubule polymer to grow and shrink. As indicated in the legend, the grey circles depict tubulin (dark grey, alpha and light grey, beta), the red, purple and blue components represent the ring gamma-tubulin complex, the yellow structures are the centrioles, the light green circle is the PCM. **B)** A cartoon picture shows a cell in prometaphase with maturing centrosomes (light green, with yellow centrioles), microtubules (dark grey), Eg5 (yellow stars) in relation to the condensing chromatin (blue with red centromeres), nuclear envelope (dotted line) and dynein (purple hexagons). The two centrosomes are pushed apart by Eg5 motor activity on microtubules. Also shown are the nuclear pore complex (NPC)-associated dynein motors and microtubules, which exert forces on the nuclear envelope (NE) to break it down. **C)** A cartoon schematic shows the proteins present in the centrioles and in the PCM with greater detail. It also shows a cross-section of the mother centriole to reveal the cart-wheel structure (Figure adapted from Pihan 2013).

(Mcintosh 2018). The process of compaction is guided by the posttranslational modifications of chromatin through phosphorylation and acetylation of proteins, such as histones. (Mcintosh 2018). This highly organized and condensed chromatin forms the sister chromatids which remain attached via cohesin at the arms and centromeres. As cells progress into metaphase, cohesin is lost from the arms, but remains at the centromeres. The bipolar mitotic spindle attaches to kinetochores and aligns sister chromatids along the equatorial plane (**Figure 2A**). When each sister chromatid forms stable attachments to the spindle, the spindle assembly checkpoint is satisfied, and cells exit mitosis into anaphase (**Figure 2A**). Mitotic exit or anaphase entry occurs following the ubiquitin-mediated degradation of Cyclin B to decrease Cdk1 activity. In addition, the degradation of securin releases active separase to cleave cohesin from the centromeres to release the sister chromatids for their segregation to each pole. There is also a corresponding increase in phosphatase activity – Cdc14 – which helps to regulate separase activation, and PP2A which removes Cdk1 phosphates from substrates (Hayward et al. 2019). During anaphase, the spindle undergoes changes to promote the separation of sister chromatids, and in telophase the chromatin de-condenses as the nuclear envelope begins to re-assemble (**Figure 2A**).

1.2.3 Mitotic spindle – centrosomes and microtubules

The successful segregation of sister chromatids requires the assembly of a robust, microtubule-derived bipolar spindle, which originates from the centrosomes in metazoan somatic cells (**Figure 2A**). The centrosomes are composed of a daughter centriole that lies perpendicular to a mother centriole (**Figure 3A, C**). Centrioles are cylindrical structures that contain 9-triplets of microtubule blades and two sets of subdistal and distal appendages (Nigg and Holland 2018). A cross-section of a centriole reveals a lumen that contains a scaffolding structure called the

“cartwheel” (**Figure 3A,C; Nigg and Holland 2018**). The centrioles duplicate to create a second centrosome in S phase via the activity of polo-like kinase 4 (Plk4), and by the end of G2 the cell will have two tethered centrosomes that mature and separate to build the bipolar spindle (**Conduit et al. 2015**).

To undergo centriole biogenesis the mother centriole plays an important role in organizing the initial structure of the procentriole. This process relies heavily on the activation of Plk4 via the STIL complex, which triggers the recruitment of hSAS-6 to template the formation of the cartwheel structure (**Conduit et al. 2015; Nigg and Holland 2018**). Currently there are two proposed models for how the site is chosen on the mother centriole for the *de novo* formation of the procentriole. The first model suggests that Plk4, hSAS-6 and the STIL complex are recruited to a ring of scaffolding proteins, CEP152 and CEP192, on the circumference of the mother centriole (**Nigg and Holland 2018**). They are recruited to a precise symmetry-breaking site on this ring, which marks the site of procentriole formation (**Nigg and Holland 2018**). However, it is not clear how this site is chosen. A potential explanation involves positive reinforcement where STIL further stabilizes Plk4 at one location, and Plk4 at other locations undergoes self-catalyzed degradation (**Nigg and Holland 2018**). The second model proposes that a mould of the cartwheel structure is made from the lumen of the mother centriole, which is then released and used to form the procentriole. However, it is not clear why this is only done once per cell cycle and experimental evidence is needed to support this model (**Nigg and Holland 2018**).

At the G2/M transition, the centrosomes mature and separate. The fibrous tether that initially connects the two centrosomes is removed via the Nek2 kinase phosphorylation of substrates that form the tether. The physical separation of the centrosomes from one another is regulated by the activity of the Eg5/Kinesin-5 motor protein, presumably via generating force on

newly formed microtubules nucleated around the maturing centrosomes (**Figure 3B; Conduit et al. 2015; Nigg and Holland 2018**). The centrosomes mature via the activity of Aurora A kinase and Plk1, which recruits hundreds of proteins to build a more robust pericentriolar material (PCM) compared to what is typically found in interphase cells (**Woodruff et al. 2014; Conduit et al. 2015; Fry et al. 2017**). The mature centrosomes nucleate microtubules to initiate mitotic spindle assembly.

PCM proteins have unique roles in defining the size of the centrosomes, templating microtubule growth, and controlling microtubule dynamics. For example, pericentrin (PCNT) and Cep152 function as molecular rulers to determine the diameter of the PCM (**Fry et al. 2017**). Their C-termini are anchored to the centriole, while their N-termini protrude towards the cytoplasm. These rod-like structures are recruited to the PCM via Plk1 phosphorylation early on in centrosome maturation (**Woodruff et al. 2014; Fry et al. 2017**). The scaffolding protein Cdk5Rap2/Cnn is found throughout the PCM and mediates centrosome expansion by anchoring the γ -tubulin ring complex (γ -TuRC) to the centrosome (**Figure 3C; Fong et al. 2008; Woodruff et al. 2014**). While the role of the γ -TuRC is not entirely clear, γ -tubulin can bind to α - β tubulin dimers and template polymer assembly.

It has remained unclear how the γ -TuRC controls the nucleation of microtubule polymers. A combination of *in vitro* studies of microtubule assembly on immobilized human γ -TuRCs, coupled with structural studies by cryo-EM and crosslinking mass spectrometry (CLMS) by Consolati et al. (2020) revealed novel features of the complex that shed light on how it could control polymer growth. It was determined that γ -TuRC has an asymmetric conformation with 14 stalks of GCP (γ -tubulin complex proteins) protomers that form the cone-shaped structure of the γ -TuRC, where the fourteenth stalk lies directly above the first one (**Consolati et al. 2020**). Each

of these 14 stalk protomers contains γ -tubulin (**Consolati et al. 2020**). The first four GCP2-GCP3 heterodimers are tightly bound to one another with the help of a single actin monomer located in the bottom lumen of the cone-shaped complex, and loosely interacting GCP4-GPC5, GPC4-GPC6 and GPC2-GPC3 heterodimers which form the upper part of the cone-shaped complex (**Consolati et al. 2020**). They estimate that approximately 7 tubulin dimers are needed to seed the microtubule, and shifting between the two conformations of the γ -TuRC permits continuous assembly (**Consolati et al. 2020**). The microtubule polymerase chTOG effectively binds to the γ -TuRC, where it accelerates and stabilizes the growth of nascent microtubules (**Consolati et al. 2020**). Given that this study shows the requirement of chTOG during microtubule assembly, it remains unclear as to how this large polymerase interacts with the γ -TuRC and whether or not other factors come into play to facilitate their interaction.

Microtubules are highly dynamic polymers that can withstand tension and forces. The core subunits are α - and β -tubulin heterodimers that require GTP and Mg^{2+} to assemble into protofilaments (Borisy and Taylor 1967a; 1967b; Goodson and Jonasson 2018). They have polarity, with α -tubulin at the slow-growing minus end, and β -tubulin at the fast-growing plus end (**Figure 4A; Goodson and Jonasson 2018**). As the protofilaments form, they align off-centre, forming contacts with neighbouring protofilaments that subsequently straighten up to form a hollow tube. In somatic mammalian cells, the tube is composed of 13 linear protofilaments with a diameter of 24 nm (**Olmsted and Borisy 1973; Goodson and Jonasson 2018**). It was hypothesized that this number is templated by the γ -TuRC at the centrosome, where the minus-ends of the microtubules are anchored in the cell (**Figure 4A; Olmsted and Borisy 1973; Goodson and Jonasson 2018**). However, several studies showed that this may not be the case, and it is not clear why this number of protofilaments is favored (**Borisy and Taylor 1967a, 1967b;**

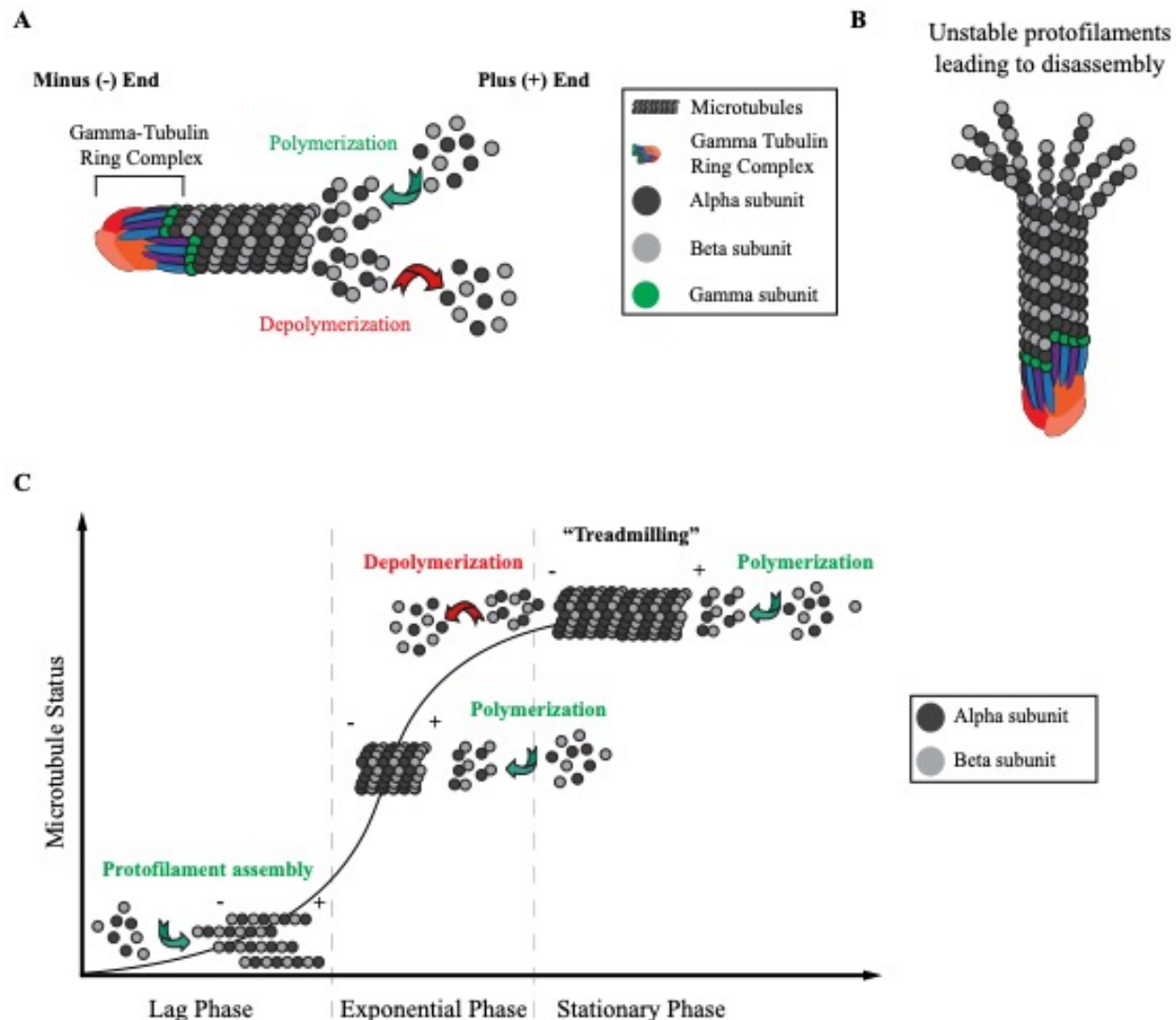


Figure 4. Microtubule dynamics. **A)** A cartoon schematic shows the γ -tubulin ring complex anchoring the minus-end of the microtubule polymer. With the minus-end anchored the polymerization and depolymerization occurs at the plus-end. The tubulin dimers are in grey, the gamma subunit is in green, the ring complex is in red, purple and blue. **B)** A cartoon schematic shows instability of the polymer. When the plus-end is destabilized, and the protofilaments peel apart from one another. **C)** A graph depicts the polymerization of microtubules *in vitro*. With no anchoring of the minus end, growth and/or disassembly can occur at both the minus and plus ends. The critical concentration of free tubulin dimers required to support growth is lower for the plus vs. minus end. At concentrations above this, polymer growth is supported, while at concentrations in between, growth is only favored at the plus end and treadmilling keeps polymers at a constant length. This plateau is reached as the concentration of free dimers decreases due to their assembly into the polymers.

Goodson and Jonasson 2018). When β -tubulin is GTP-bound, polymer growth is favored at both ends depending on the critical concentration of free tubulin (Olmsted and Borisy 1973; Mitchison and Kirschner 1987; Brouhard and Rice 2018). When hydrolysis occurs, this induces a curved conformation causing the protofilaments to peel apart and undergo catastrophe (**Brouhard and Rice 2018; Figure 4B**). *In vitro*, there are three phases of microtubule assembly. The first is the lag phase which constitutes the nucleation of dimers and assembly of protofilaments and is followed by the exponential phase where the microtubule polymers have assembled and favor growth. This growth reaches a plateau in the stationary phase where the critical concentration of free tubulin dimers is insufficient to support growth from the minus end, but growth can occur from the plus end causing a ‘treadmilling effect’ (**Figure 4C**). In cells, the minus-ends are typically anchored in the PCM of the centrosome, which provides added stability and so growth and depolymerization are favored at the plus-ends (**Figures 3A, 4A**).

One of the major functions of spindle microtubules is to “search and capture” sister chromatids, and promote their segregation to each pole by forming stable attachments at their kinetochores (**Rieder and Alexander 1990; Hayden et al. 1990; Heald and Khodjakov 2015**). Hayden et al. in 1990 observed microtubules interacting with the kinetochore and pulling the sister chromatids towards the spindle pole in a newt lung cell (**Rieder and Alexander 1990; Hayden et al. 1990**). Many proteins (i.e. TPX2, HSET, NSL, Augmin complex) control the *de novo* nucleation of microtubules at the plus-ends to favor kinetochore attachments and are regulated by a chromatin-associated Ran-GTP gradient (**Heald and Khodjakov 2015**). Ran-GTP is generated by the regulator of chromosome condensation 1 (RCC1), a RanGEF that associates with chromatin. RanGAP, which downregulates Ran, is found in the surrounding cytosol. Proteins that are regulated by this steep Ran-GTP gradient contain nuclear localization signals (NLS) that can bind

to importins. Importin-binding can impact the function of these proteins by affecting their ability to bind to other proteins or causing conformational changes. Ran-GTP releases importins from these NLS-proteins, which alters their function to carry out their respective roles in stabilizing, organizing, cross-linking and/or nucleating microtubules. This Ran-mediated control of microtubules occurs at the plus-ends of unattached microtubules near chromatin, which helps them to form the kinetochore fibers (K-fibers; **Heald and Khodjakov 2015**). These K-fibers are segments of new microtubules with their plus ends attached to the kinetochore, and growth occurs at this end until their free minus-ends reach the spindle pole for integration (**Khodjakov et al. 2003**). Altogether, microtubules and their dynamics involve a fine balance between structural organization of the heterodimers into microtubules, their associated proteins (microtubule associated proteins; MAPs) and the recruitment of various factors that allow the cell to undergo division.

In cells, microtubule growth is controlled by ch-TOG, a microtubule polymerase, whose location and/or activity is mediated by other proteins. ch-TOG is a microtubule polymerase that belongs to the highly conserved XMAP215 family, and is required for bipolar spindle formation in cells (**Barr and Bakal 2015**). These highly conserved proteins contain a pentameric tumor overexpressed gene (TOG) domain array and a C-terminal domain, although the number of TOG domains varies among organisms. The TOG domains are linked by 60-100 residues with no predicted secondary structure, but are basic in nature possibly to permit microtubule-binding (**Fox et al. 2014**). Each of the TOG domains has six Huntingtin, elongation factor 3, protein phosphatase 3A, target of rapamycin 1 (HEAT) repeats (HRs), which are capable of interacting with either α - and β -tubulin depending on their position at the C- or N-terminal of the domain (**Fox et al. 2014**). Studies on XMAP215/Minispindles (Msps) in *D. melanogaster* describe TOG1 and TOG2

domains as being architecturally similar to one another and have a bent conformation for binding to free tubulin, while TOG3 is structurally different from TOG1 and TOG2, but has a similar tubulin binding interface. TOG4 is quite different compared to the others due to a bend caused by 3 HRs at the C-terminus, and TOG5 has a distinct architecture altogether that may be required for interacting with the microtubule lattice to bridge protofilaments (**Byrnes and Slep 2017**). Conflicting models based on structural and biochemical information suggest that each TOG array interacts with an array of tubulin heterodimers, or that TOGs 1 to 4 wrap their domains around a single tubulin heterodimer for plus-end addition (**Byrnes and Slep 2017; Nithianantham et al. 2018**). Based on a study done by Hood et al. 2013, is described the C-terminal domain of ch-TOG as a novel TOG6 domain that is proposed to be the interacting region for TACC3, which is described in more detail below (**Hood et al. 2013**).

Ch-TOG localizes to centrosomes and kinetochores, reflecting its requirement at these locations. The most prominent localization is at the centrosome, where ch-TOG helps the cell to overcome the rate limiting step of nucleation from γ -TuRCs. For example, the *in vitro* microtubule nucleation from immobilized human γ -TuRCs was stimulated by a factor of 21-fold in the presence of ch-TOG (**Consolati et al. 2020**). This is in agreement with previous biochemical studies done by Roostalu et al. (2015) where adding 200 nM of purified ch-TOG increased the velocity of polymerization of microtubules by 17-fold compared to free tubulin alone. ch-TOG also localizes to the plus-ends of microtubules, where it promotes protofilament growth at the kinetochores, while stabilizing them (**Booth et al. 2011**). Biochemical studies done by Roostalu et al. have shown how other factors like TPX2, which is released from α/β importin in the vicinity of chromatin by RanGTP, can synergize with ch-TOG's polymerase activity by further stabilizing microtubules (**Roostalu et al. 2015**). It revealed that, although ch-TOG is not directly dependent on TPX2 for

nucleation, TPX2 shifted the balance from catastrophe by stabilizing the curved state of the protofilaments and permitting the growth of longer protofilaments (**Roostalu et al. 2015**). These longer protofilaments are better able to make more lateral contacts between each other and form the microtubule (**Roostalu et al. 2015**). Although this provides some insight on how a partner of ch-TOG controls microtubule assembly *in vitro*, we still do not completely understand how other suspected proteins participate inside the cell.

Enzymes such as ch-TOG that control microtubule growth or their instability are important for controlling spindle size, and their activities balance one another. The mitotic centromere-associated kinesin (MCAK/KIF2C) is a kinesin-13 family member that promotes microtubule depolymerization (**Wordeman and Mitchison 1995; Barr and Gergely 2008**). The depletion of ch-TOG via small interfering RNAs (siRNA) causes a decrease in microtubules and the formation of multipolar spindles in cultured human cells, and these phenotypes are suppressed by co-depletion of MCAK (**Barr and Gergely 2008**). MCAK function is best understood for its requirement at kinetochores where it is involved in error correction of improper K-fiber attachments and is mainly governed by Aurora B kinase (**Kline-Smith et al. 2004; Andrews et al. 2004**). However, MCAK also could have a role at the centrosomes. In a study using *Xenopus* oocyte extracts lacking chromatin and centrosomes, the localization of MCAK was negatively regulated by Aurora A kinase at the spindle poles (**Zhang et al. 2008**). Other studies have postulated that Aurora A regulates MCAK by recruiting the TACC3/ch-TOG complex to the centrosome, which can selectively protect and stabilize centrosome-associated microtubules from the depolymerase activity of MCAK (**Barr and Gergely 2007; Barr and Gergely 2008**). Another theory involves the KinI kinesin Kif2a, which is another member of the kinesin-13 family, which has been shown to depolymerize microtubules at the spindle poles (**Ganem and Compton 2004;**

Gaetz and Kapoor 2004; Ganem et al. 2005; Manning et al. 2007; Jang et al. 2009; Uehara et al. 2013). Studies done by Jang et al. 2009, showed that Plk1 promotes the activity of Kif2a, and enhances its localization to the spindle and spindle poles (**Jang et al. 2009**). They also found that Aurora A kinase colocalizes with Kif2a at the spindle poles and acts as an inhibitor of the depolymerase (**Jang et al. 2009**). Therefore, multiple depolymerases control microtubule length and stability at the plus and minus ends, while ch-TOG is required largely for their growth. It is important to clarify the functions of these enzymes at the spindle poles, as most of the research has focused on their role at the kinetochore.

In cells, ch-TOG function is (in part) mediated by forming a complex with transforming acidic coiled-coil protein 3 (TACC3) and Aurora A kinase. As described earlier, a major regulator for microtubule nucleation at the centrosome is Aurora A kinase, which promotes its own activity through autophosphorylation of its Thr288 residue in its activating T-loop (**Barr and Gergely 2007; Willems et al. 2018**). TPX2 is capable of binding to Aurora A kinase and maintains its activity by preventing its dephosphorylation by protein phosphatase 1 (PP1; **Barr and Gergely 2007**). Active Aurora A kinase is then capable of phosphorylating TACC3, which in turn recruits ch-TOG (also referred to as XMAP215) to the centrosome for microtubule nucleation (**Barr and Gergely 2007; Zhang et al. 2008; Fielding et al. 2011; Hood et al. 2013; Gutierrez-Caballero et al. 2015**). This is supported by studies done in *Drosophila* and *Xenopus* mitotic cells, where the TACC3/XMAP215 complex localizes to the centrosome via a pool of P-TACC3 regulated by Aurora A kinase, which is then unable to exchange with the soluble pool of unphosphorylated TACC3 localized more broadly to the spindle (**Barros et al. 2005; Kinoshita et al. 2005**). This interplay between active Aurora A kinase, TACC3 and chTOG has yet to be properly understood, as TACC3 knockdown does not cause a strong phenotype in cultured human cells, while ch-TOG

knockdown causes severe spindle defects (**Barr and Gergely 2008; Gutierrez-Caballero et al. 2015**). Although TACC3 may help with ch-TOG recruitment to the centrosome, the polymerase likely does not depend on TACC3 for its activity, and whether ch-TOG relies on other factors for its localization and function at the minus-end is not clear.

In summary, the interplay between Aurora A kinase, TACC3, ch-TOG, Kif2a, MCAK and TPX2 is still understudied and more work is needed to understand how they control mitotic spindle assembly in a dividing cell.

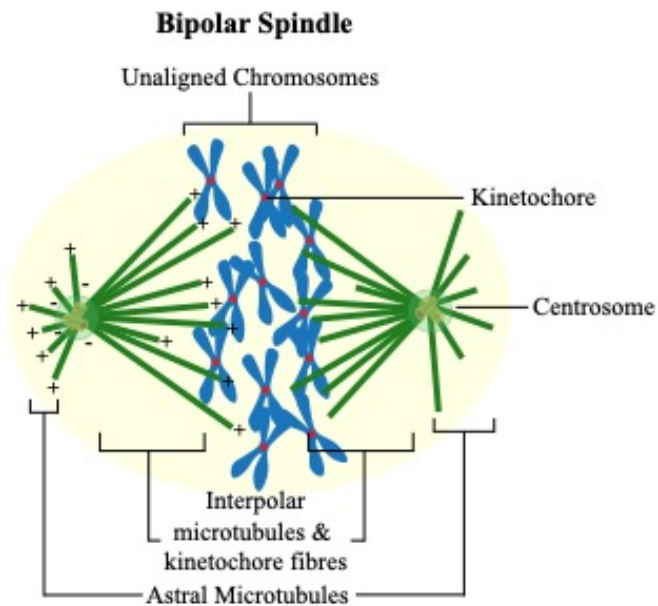
1.2.4 The Spindle Assembly Checkpoint (SAC)

The failure to form stable kinetochore attachments triggers the spindle assembly checkpoint (SAC), which arrests cells in mitosis to correct these attachments and avoid aneuploidy. Our understanding of the SAC began with studies in yeast done by the Hoyt and Murray labs, where they isolated mutant yeast strains that were able to progress through mitosis despite having spindle defects caused by benzimidazole treatment (**Hoyt 1991; Li and Murray 1991; Hayward et al. 2019**). They called these the budding uninhibited by benzimidazole (BUB) and mitotic arrest deficient (MAD) genes (**Hoyt 1991; Li and Murray 1991; Hayward et al. 2019**). Other studies showed that mammalian cells rely on similar proteins, suggesting that their function is conserved and necessary for proper cell division (**Li and Nicklas 1995; Rieder et al. 1995; Taylor et al. 1998**). Once kinetochores from each pair of sister chromatids form stable attachments to microtubules from each spindle pole (amphitelic), equal tension is generated, which causes a change in the localization and/or activity of BUB and MAD components to satisfy the spindle assembly checkpoint (SAC) and release inhibition of the Anaphase Promoting Complex (APC) for cell cycle exit (**Figure 5A, B; Lara-Gonzalez et al. 2012; Musacchio 2015; Hayward et al.**

2019). A key component of the SAC is monopolar spindle 1 (MPS1), which localizes to unattached kinetochores through Cdk1-Cyclin B1 activity (**Lara-Gonzalez et al. 2012; Hayward et al. 2019**). The kinetochore is a large protein complex assembled on the centromere, where two key subcomplexes are required for function, namely, Constitutive Centromere-Associated Network (CCAN) and the kinetochore scaffold 1 (KNL1)/Mis12/Ndc80 (KMN) network. The CCAN interacts directly with the centromere (inner kinetochore) and recruits the KMN network (outer kinetochore) during mitosis, together they form the bridge between microtubules and chromatin (**Hara and Fukagawa 2018; Monda and Cheeseman 2018**). With respect to faithful microtubule attachments, the Ndc80 complex, which is part of the KMN network is a key player in stabilizing the plus-end interaction with the kinetochore, while SAC proteins are recruited to ensure correct attachments in a bi-oriented fashion (**Lara-Gonzalez et al. 2012; Hara and Fukagawa 2018; Monda and Cheeseman 2018; Hayward et al. 2019**). This recruitment is mediated by MPS1 phosphorylation of the outer kinetochore protein KNL1, which offers a site for docking and recruitment of BUB1-BUB3 (**Lara-Gonzalez et al. 2012; Hayward et al. 2019**). Then the MAD1-MAD2 complex is recruited to the kinetochore, where MAD2 undergoes conformational changes to form Closed MAD2 (C-MDA2), and together with BUBR1, BUB3, form the Mitotic Checkpoint Complex (MCC; **Figure 5B; Lara-Gonzalez et al. 2012; Hayward et al. 2019**). Although binding of Cdc20 is required to activate the APC (APC/C^{Cdc20}), studies done by Izawa and Pines (2015) revealed that MCC binds to free or APC-bound Cdc20 in the presence of unattached kinetochores, preventing APC/C activity (**Izawa and Pines 2015**). The ability of MCC to associate freely with Cdc20 enables tight control over APC/C activation (**Izawa and Pines 2015; Hayward et al. 2019; Figure 5B**). Once all of the kinetochores are attached, MAD2 disappears from the kinetochore, the MCC no longer binds to Cdc20, and active APC/C^{Cdc20} is

able to mediate the degradation of securin and cyclin B for mitotic exit (**Musacchio 2015; Hayward et al. 2019; Figure 5B**). However, it is not clear how small amounts of kinetochore-associated MAD2 can over-ride the activation of the APC/C, for example via incorrect attachment at a single sister chromatid pair. Incorrect kinetochore attachments (merotelic, syntelic or monotelic) are corrected by Aurora B kinase, which leads to the release of microtubule plus ends from the kinetochores (**Musacchio 2015**). But merotelic attachments can also generate tension that could be incorrectly sensed by the cell to permit exit with lagging chromosomes, which could lead to aneuploidy. When the MCC persists, this causes persistent Cdk1 activity and stress, which triggers the apoptotic machinery, although how this occurs is not well understood.

A



B

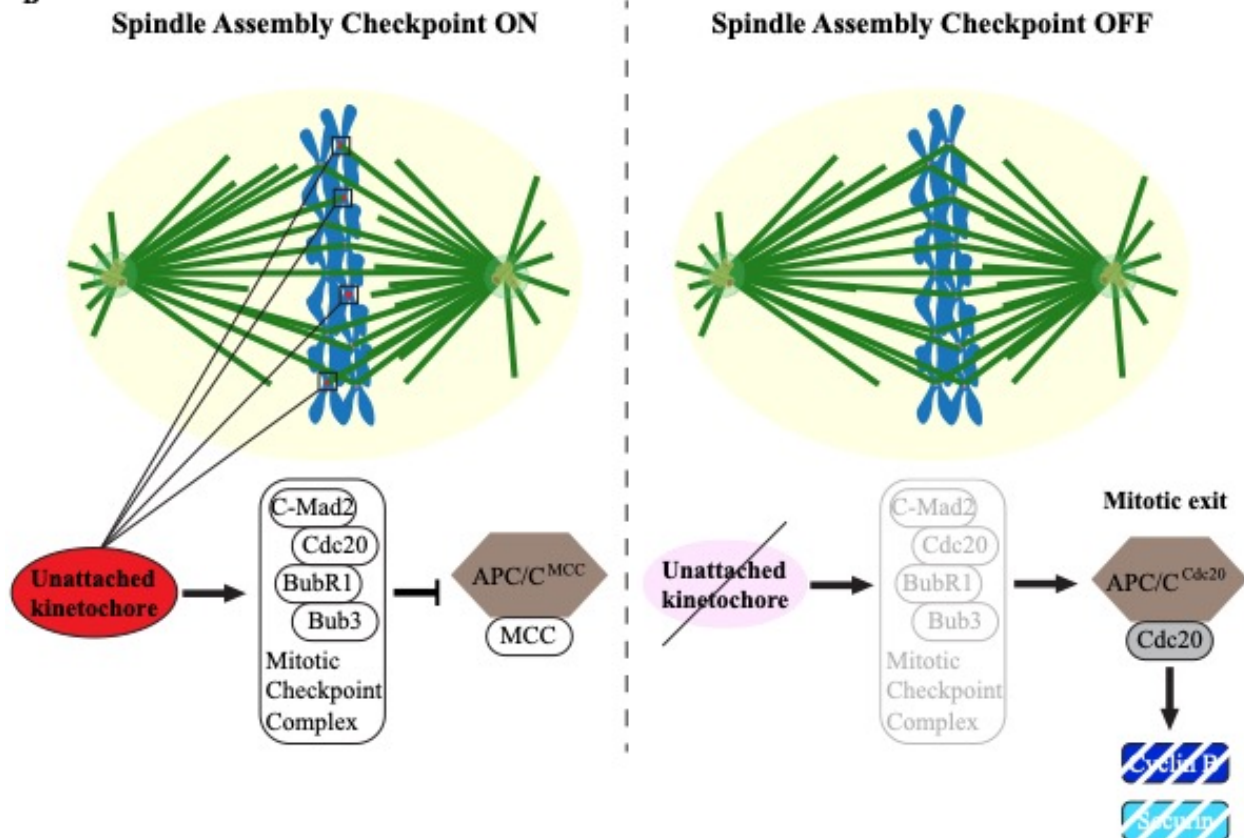


Figure 5. The spindle assembly checkpoint (SAC). **A**) A cartoon schematic shows the bipolar spindle that forms during mitosis. Microtubules emanate from each centrosome located at opposite poles and point toward the cortex (astral microtubules), or toward the equatorial plane (in this figure called interpolar microtubules and kinetochore fibres). The plus-ends of the microtubules form kinetochore attachments with sister chromatids, which aligns them at the equatorial plane. Microtubules are in green, chromosomes are in blue, and unattached kinetochores are in red. **B**) Cartoon schematics show when the SAC is on (left) and when it is satisfied and turned off (right). When uneven tension is sensed between sister chromatids, due to unattached or improperly formed kinetochores, the SAC is on. A complex of MAD and BUB proteins (mitotic checkpoint complex, MCC) localize to the unattached kinetochore (red), which templates their activation to inhibit the APC/C (brown hexagon). Once all kinetochores are properly attached (pink), the MCC complex no longer inhibits the APC. Activation of the APC/C by binding of the cofactor Cdc20 (grey) stimulates the degradation of Cyclin B (blue hatched) and securin (light blue hatched) to exit the cell cycle.

1.3 When a healthy cell loses its way

1.3.1 Hallmarks of cancer

Cancer arises when cells divide in an uncontrolled manner and undergo metastasis, when they leave their tissue of origin and invade other tissues. As mentioned earlier, cancers arise due to an accumulation of mutations that alters key cellular processes, and acquire several hallmarks that contribute to their progression (**Hanahan and Weinberg 2011**). In addition to uncontrolled cell proliferation, these also include other changes such as resisting cell death, enabling replicative immortality, evading growth suppressors, inducing angiogenesis, and activating invasion and metastasis (**Hanahan and Weinberg 2011**). These hallmarks also can be influenced non-autonomously through healthy cells and tissues in the local environment.

1.3.2 Loss of controlled cell proliferation

All cancer cells have lost cell cycle control, permitting their continued proliferation. In a normal context, growth factors such as EGF bind to their cognate tyrosine kinase receptors, such as EGFR, and their activation recruits adaptors that help activate Ras, which in turn activates a mitogen-activated protein (MAP) kinase signaling cascade that leads to the upregulation of transcription factors required for cell growth and division (**Shapiro 2002; Cohen-Mansfield et al. 2017; Hymowitz and Malek 2018**). Thus, the dysregulation of MAP kinase signaling via constitutively active Ras causes uncontrolled cell proliferation (**Shapiro 2002; Cohen-Mansfield et al. 2017; Hymowitz and Malek 2018**). Ras GTPase proteins act as binary molecular switches, as they cycle between active GTP-bound and inactive GDP-bound states via guanine exchange-factors (GEFs) and GTPase-activating proteins (GAPs), respectively. Importantly, active Ras localizes to the plasma membrane, where it recruits and stimulates the formation of Raf dimers to

activate MEK/ERK signaling. In humans, there are four distinct Ras isoforms: HRas, NRas, KRas4a and KRas4b, while Raf contains family members ARaf, BRaf and CRaf (**Shapiro 2002; Cohen-Mansfield et al. 2017; Hymowitz and Malek 2018**). Importantly, the KRas isoform harbours missense mutations that mimics the active GTP-bound state and constitutes ~85% of all *RAS* mutations (**Simanshu 2017; Hymowitz and Malek 2018; Liu et al. 2019**). In addition, ~70% of melanomas have an activating BRaf-V600E mutation, which is no longer dependent on Ras for its activity (**Hymowitz and Malek 2018**). These examples highlight the importance of this pathway in contributing to cancers, where activating mutations in Ras or Raf can cause cells to continuously proliferate in the absence of extracellular growth factors.

Relevant for this thesis, several types of breast cancers are categorized based on whether they have upregulated HER2, EGFR and/or progesterone receptor pathways (**Cheang et al. 2008; Wieduwilt and Moasser 2008**). HER2 and EGFR are ERBB family members, which respond to a variety of EGF-like ligands (**Cheang et al. 2008; Wieduwilt and Moasser 2008**). Similar to EGFR, HER2 dimerizes and autophosphorylates tyrosine residues to recruit adaptors or scaffolds that trigger signalling cascades to promote cell proliferation and survival (**Cheang et al. 2008; Weigelt et al. 2010; Fink and Chipuk 2013; Iqbal and Iqbal 2014**). When these pathways are upregulated, they cause uncontrolled proliferation. Although hyperproliferation should trigger cell cycle arrest or apoptosis via p53, many breast cancers also have lost p53 function, which permits the accumulation of mutations and genomic instability that contributes to their progression (**Mantovani et al. 2019**). While treatments involving hormone therapy or that selectively target HER2 or EGFR are successfully used to treat some breast cancers, they are ineffective against triple negative breast cancers (TNBCs; **Cheang et al. 2008; Aysola et al. 2014**). TNBCs

simultaneously lack or downregulate EGFR, HER2 and progesterone receptors (**Cheang et al. 2008; Aysola et al. 2014**).

Due to the challenges in categorizing TNBCs, classification criteria were developed based on gene expression profiling of tumor samples from patients at the Fudan University Shanghai Cancer Center (FUSCC) (**Liu et al. 2016; Yin et al. 2020**). They identified 4 subtypes of TNBCs, which were in agreement with those identified by earlier classification systems (**Liu et al. 2016; Yin et al. 2020**). Of particular interest is the BLIS (BL1 and M subtypes of the Lehmann/Pienpol system) subtype, which describes a population of TNBCs exhibiting highly proliferative properties (**Liu et al. 2016; Yin et al. 2020**). Associated with the BLIS subtype, are the overexpression of genes associated with proliferation, such as *CENPF*, *BUB1*, *PRC1* as well as genes involved in the suppression of the immune signalling pathway (**Liu et al. 2016; Yin et al. 2020**). The BLIS subtype was also found to be associated with the poorest recurrence-free survival (RFS; **Liu et al. 2016; Yin et al. 2020**). The subtyping of TNBCs revealed biomarkers that are useful for diagnosis, but also could be targeted to develop new therapies.

1.3.3 Genetic Changes that affect mitotic spindles

Many cancer cells also acquire genetic changes that affect mitotic spindle assembly or organization (**Cirillo et al. 2017; Ertynch et al. 2014**). For example, TACC3, ch-TOG/CKAP5 and Aurora A kinase are upregulated in colorectal cancers (**Ertynch et al. 2014; Harrison and Bleiler 2017**). Their overexpression allows for an increased rate of microtubule assembly, which contributes to chromosomal instability (CIN) (**Cirillo et al. 2017; Ertynch et al. 2014**). With altered microtubules dynamics, these cells have a greater chance of having erroneous kinetochore attachments, which may be challenging to correct, leading to an increase in CIN (**Harrison and**

Bleiler 2017). Interestingly, colorectal cancer has a slower growth rate compared to other cancers, which is thought to be caused by their extreme genomic instability (**Harrison and Bleiler 2017**). This reveals a clear pitfall in the design of cancers, where CIN is a necessity for their evolution and progression, but if CIN is too extreme it makes cells inviable. Thus, treating cancers that have altered microtubule dynamics with microtubule targeting drugs could be an effective way to push CIN beyond the point of no return.

Cancer cells also gain CIN by the acquisition of extra centrosomes. Theodore Boveri first documented the presence of supernumerary centrosomes in cancer cells in 1914 and coined the *Boveri's Hypothesis* which theorized their role in cancer progression. Boveri proposed that cells harboring multiple centrosomes lead to the formation of extra spindle poles which caused a gain or loss of chromosomes via their breakage by attaching to multiple poles (**Brinkley 2016; Hyman 2005; Scheer 2018**). This breakage-fusion cycle is propagated with each subsequent division. There are several ways in which cells can gain additional centrosomes. When cells fail cytokinesis, undergo mitotic slippage, or if Plk4 is not properly regulated, all can lead to the acquisition or formation of additional centrosomes. Some cancer cells have adapted to having additional centrosomes, by relying on mechanisms that cluster them to form pseudopoles that can build functional bipolar spindles. While the exact mechanisms are not clear, a dynein motor protein known as KIFC1/HSET enables focusing of the extra centrosomes to the poles. Elevated HSET expression levels in epithelial ovarian carcinoma has been linked with poor prognosis (**Mittal et al. 2016**). Another factor involved in the clustering mechanism is integrin-linked kinase (ILK), which is crucial for clustering multiple centrosomes in breast and prostate cancer cells (**Fielding et al. 2011**). In the same study, cells containing only two centrosomes were not affected by ILK inhibition and the authors proposed that ILK could be a promising target for anti-cancer therapies

(**Fielding et al. 2011; Kawamura et al. 2013**). This is based on the premise that the inhibition of ILK (or HSET) has little impact on mitosis of cells with normal centrosome numbers but disrupts clustering in cells with multiple centrosomes causing mitotic catastrophe. However, ILK is required in healthy cells for adhesion, cell shape and cell polarity, with crucial roles in tissue development and homeostasis (**Rudkouskaya et al. 2014; Sakai et al. 2003**). In addition, previous studies showed that ILK is highly expressed in the human brain where it may be required for development of the nervous system (**Mills et al. 2003; Xu et al. 2015; Hussain and Macklin 2017**). Therefore, despite their promise as potential targets for developing anti-cancer therapies, proteins like ILK may not be ideal to inhibit due to their pleiotropic functions in healthy cells and tissues. Our lack of knowledge of human cell physiology in the tissue-specific context is a challenge that applies to the development of any targeted therapy. Presumably many genes have been retained evolutionarily for their important roles in at least a subset of cells in complex organisms, and/or may have pleiotropic roles making it unlikely they would be viable targets for anti-cancer therapies. As indicated in the next section, this is likely why most targeted therapies have failed during clinical trials.

1.3.4 Chemotherapy – microtubule targeting agents

Various aspects of the cell cycle machinery are targeted by some of the most successful anti-cancer drugs, which include alkylating agents, anti-metabolites, anti-mitotics and other inhibitors capable of disrupting key proteins required for different stages of the cell cycle (**Livshits et al. 2014**). These drugs are not selective for cancer cells per se, but tend to have higher efficacy in cancer compared to healthy cells due to their rapid rates of proliferation (**Hanahan and Weinberg 2011; Dominguez-Brauer et al. 2015**). In particular, cancer cells are sensitive to

microtubule-targeting agents (MTAs), which disrupt microtubule dynamics. As described earlier, in addition to their rapid proliferation, many cancer cells have altered expression levels of microtubule associated proteins (MAPs), making their microtubules more sensitive to disruption with MTAs (**Cirillo et al. 2017; Kozielski 2015; Musacchio 2015**). MTAs include those that either stabilize (e.g. Taxol/paclitaxel) or destabilize (e.g. vinblastine) microtubules and are used in the clinic to treat a plethora of cancers as well as other diseases (Figure 6).

1.3.4.1 Taxol

Multiple cancers are treated with TaxolTM (paclitaxel), which stabilizes microtubules causing mitotic arrest or catastrophe and cell death (**Weaver 2014**). Taxol was discovered through collaboration with the National Cancer Institute (NCI) and the U.S. Department of Agriculture (USDA) from the years 1960-1981, where 115,000 extracts from 15,000 plant species were screened for anti-cancer activity (**Weaver 2014**). On the last day of his expedition in 1962, USDA botanist Arthur Barclay collected crude extracts from the bark, twigs, needles and fruit of the Pacific yew tree (*Taxus brevifolia*) and found that those from the bark had cytotoxic effects on tumors (**Weaver 2014; Yang and Horwitz 2017**). In 1967, researchers Mansukh Wani and Monroe Wall isolated and identified the active compound from the extract and named it Taxol. By 1994, 32 years after the first sample was obtained, the Food and Drug Administration (FDA) approved Taxol for the treatment of breast cancers, and in 1999 it was approved for the treatment of non-small cell lung cancers (NSCLC). Taxol is still used to treat particularly aggressive cancers such as TNBCs that have poor response to more targeted therapies (**Cheang et al. 2008; Aysola et al. 2014**).

Taxol belongs to the family of taxanes and binds to the N-terminal 31 amino acid of β -tubulin on the luminal side of the microtubule (Alqahtani et al. 2019). Biochemical assays revealed that in the presence of purified tubulin, Taxol can polymerize microtubules with enhanced kinetics compared to tubulin on its own (Horwitz 1992). Taxol is predicted to stabilize microtubules via promoting an increase in the longitudinal and lateral contact between dimers, which causes them to adopt a straight conformation (Xiao et al. 2006). The interaction of Taxol with the hydrophobic pocket in the β -tubulin subunit is reversible and follows a one to one stoichiometry (Xiao et al. 2006; Yang and Horwitz 2017; Figure 6A). As described earlier, successful mitosis requires the formation of a bipolar spindle with dynamic microtubules to align and segregate chromosomes to their respective poles (Musacchio 2015; Cirillo et al. 2017). When treated with Taxol, microtubule dynamics are lost as the spindle ‘freezes’ in metaphase with either unattached kinetochores or due to loss in inter-kinetochore tension, which triggers the SAC and causes cell cycle arrest and eventually apoptosis. However, in cells where the SAC is not functional, cells could slip through mitosis with unequally segregated chromosomes creating extreme aneuploidy, which becomes catastrophic (Funk et al. 2016; Lok et al. 2020). Like most drugs, there is a dose-dependent activity associated with Taxol, and it is not clear what intracellular concentration is reached *in vivo*, and what phenotypes this may cause given the poor solubility of paclitaxel *in vivo* (Weaver 2014). One hypothesis is that the concentration is quite low, and permits some dynamics, but sufficient loss of spindle organization to form multipolar spindles producing inviable daughter cells with high CIN (Weaver 2014; Zasadil et al. 2014; Funk, Zasadil, and Weaver 2016). Cultured cells treated with Taxol for longer periods of time have disorganized spindles and fragmentation of spindle poles. Despite its efficacy, Taxol has poor solubility requiring the use of a surfactant called polyoxyethylated castor oil as a solvent to reach

clinically relevant concentrations, which causes severe side-effects for the patient (**Dumontet and Jordan 2010**). To overcome this, an encapsulated version of TaxolTM, named AbraxaneTM, was developed for improved delivery. However, another limitation is that patients often develop Taxol-resistance, with few other alternatives.

1.3.4.2 Vinblastine

Another well-known class of MTAs called Vinca alkaloids (VA) are used to treat cancers. Vinca alkaloids were isolated from extracts of the Madagascar periwinkle plant by Canadian scientists Robert Noble and Charles Thomas Beer in the 1950s (**Cutts et al. 1960; Noble et al. 1958; Martino et al. 2018**). Vinblastine was identified and isolated from other phytochemical studies and was approved by the FDA in 1961 to treat various forms of cancer, making it one of the first plant-derived antimitotic drugs to enter the market (**Figure 6A; Cutts et al. 1960; Noble et al. 1958; Martino et al. 2018**). There are currently five vinca-alkaloids approved for use in treating various cancers (vinblastine, vincristine, vindesine, vinorelbine and vinflunine). Vinblastine binds at the interface of α/β -tubulin and introduces a molecular wedge causing the protofilaments to adopt a curved conformation that destabilizes their plus-ends (**Panda et al. 2002; Martino et al. 2018; Gigant et al. 2005; Jordan and Kamath 2007**). Studies done by Panda et al 2002, suggested that vinblastine disrupts the microtubule “cap”, which depends on the hydrolysis of GTP to GDP and the addition of P_i to β -tubulin therefore stabilizing the cap (**Panda et al. 2002**). At low concentrations of vinblastine, P_i is prematurely released and protein-protein interaction with adjacent tubulin dimers is favoured, and together they destabilize the microtubule “cap” and cause depolymerization (**Panda et al. 2002; Martino et al. 2018**). At high concentrations, vinblastine causes microtubules to depolymerize and the dimers have exposed

alkaloid sites that it binds to and leads to the formation of highly organized paracrystalline and spiral aggregates (**Martino et al. 2018**).

1.3.4.3 Colchicine

Another well-characterized MTA is colchicine, which is used clinically, although not to treat cancers (**Figure 6A**). Colchicine is an alkaloid extracted from plants belonging to the genus *Colchicum* (*autumn crocus*; **Leung et al. 2015**). Colchicine was discovered in 1967 by Gary Borisy and led to the biochemical purification of tubulin (Borisy and Taylor 1967b). Colchicine binds to a deep pocket in β -tubulin and prevents growth or causes catastrophe at the plus-end (**Fitzgerald 1976; Massarotti et al. 2012; Kumar et al. 2016; Wang et al. 2016**). Colchicine is used in the clinic to treat gout and Familial Mediterranean Fever (FMF), but failed as an anti-cancer therapy (**Jordan and Kamath 2007; Field et al. 2015; Leung et al. 2015**). It is not clear why colchicine failed, but could be due to efficacy and accessibility issues *in vivo* (**Jordan and Kamath 2007; Field et al. 2015; Leung et al. 2015**). The discovery and characterization of colchicine has led to a greater understanding of microtubule dynamics and scientists continue to synthesize derivatives with the hope of finding ones that have better toxicity profiles. Researchers speculate that a derivative with altered binding affinity for tubulin could have a greater chance of success by being more selective for mitotic vs. interphase cells and alter spindle organization vs. total loss of microtubules.

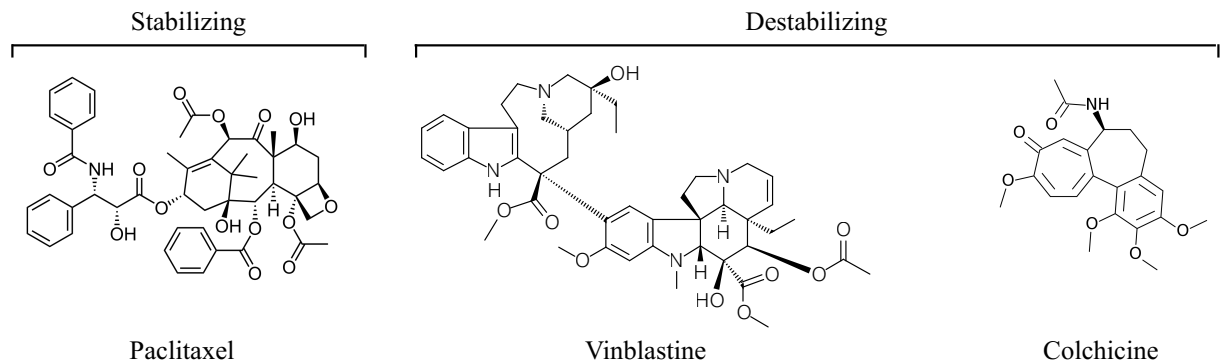


Figure 6. The chemical structures of well-known microtubule targeting agents (MTAs). The chemical structures of Taxol (also called paclitaxel) as an example of a stabilizing MTA, as well as vinblastine and colchicine as examples of destabilizing MTAs are shown.

1.3.5 Resistance to Chemotherapy

Although MTAs have been used as successful chemotherapies, patients can gain resistance to these drugs leaving them with few alternatives. Resistance is driven by the rapid evolution of cancers, which have genomic instability and can acquire rapid changes in their expression profiles. Furthermore, the majority of cancers are heterogenous, composed of multiple subsets of cell populations with different genetic changes (**Wein and Loi 2017**).

A well-studied mechanism for chemoresistance occurs through transporter-mediated drug efflux, where the ATP-binding cassette (ABC) transporters use ATP to pump out drugs from inside the cell. In the case of TNBCs, the multidrug-resistant protein-1 (MRP1), breast cancer resistance protein (BCRP) and multidrug-resistant protein-8 (MRP8) all play a significant role in shielding cells from various cytotoxic drugs (**Nedeljković and Damjanović 2019**). More specifically, MRP1 confers resistance in cells to anthracyclines, taxanes and methotrexate, while BCRP pumps out 5-Fluorouracil, methotrexate, doxorubicin and others (**Nedeljković and Damjanović 2019**). Thus, the overexpression of these transporters is common in TNBCs and plays an important role in overcoming chemotherapeutic agents (**Nedeljković and Damjanović 2019**).

Another mechanism of resistance relies on changes in the expression of β -tubulin isotypes. Currently there are 7 known isotypes of β -tubulin: β I, β II, β III, β IVa, β IVb, β V and β VI (**Kamath et al. 2005**). They mainly differ in their C-terminal region, which lies outside of the core tubulin structure and coordinates specific MAP interactions (**Kamath et al. 2005**). Studies done using various cell lines and tumors showed that the overexpression of β III-tubulin diminishes their response to Taxol (**Kavallaris et al. 1999; Gonçalves et al. 2001; Orr et al. 2003; Yusuf et al. 2003; Hari et al. 2003; Kamath et al. 2005**). Although it is not clear why this β III-tubulin isotype confers resistance, it restores microtubule dynamics in the presence of Taxol (**Orr et al. 2003**,

Kamath et al. 2005; Stengel et al. 2010). In TNBCs, the overexpression of βIII-tubulin correlates with increased aggressiveness of the cancer and poor prognosis (**Lebok et al. 2016**).

1.4 Drug Discovery

1.4.1 *The need to find new drugs*

For chemotherapies, a ‘cocktail’ approach is often used as a way of reducing side-effects and minimizing resistance. Breast cancer is one of the most prevalent cancers in women. Depending on the stage, origin (*e.g.* ductal or basal) and presence of certain biomarkers, it can be highly treatable or have poor prognosis (**Cheang et al. 2008; Aysola et al. 2014**). As indicated earlier, TNBCs do not express Estrogen Receptor, Progesterone Receptor or the HER2 Receptor, making them untreatable by hormone or targeted therapies. Currently they are treated with Taxol alone or in combination with other drugs depending on other biomarkers and the stage of progression (**Cheang et al. 2008; Aysola et al. 2014**). Even if they respond to chemotherapy, most TNBCs have a high chance of recurrence after 5 years (**Aysola et al. 2014; Kumar and Aggarwal 2016; Miller et al. 2016**). In addition, secondary tumors often arise in the brain and lungs, which are challenging to treat with chemotherapy (**Aysola et al. 2014; Kumar and Aggarwal 2016; Miller et al. 2016**). Since there are few drugs used to treat highly progressive TNBCs, and resistance is common, it is imperative to increase the repertoire of available drugs.

1.4.2 “Bottom-up” approach to drug discovery

A popular approach for drug discovery in the pharmaceutical industry is to identify a specific molecular target based on knowledge of its cellular function, and then screen large libraries of compounds to find one that binds the target with high affinity. This target-driven

approach requires the systematic testing of compounds from a large library of synthetic, semi-synthetic and/or natural products. Once a subset of molecules has been identified, they are moved along the pipeline to further assess their binding, and if possible, modifications will be made to improve selectivity and/or efficacy. These structure-activity-relationship studies (SAR) will identify lead compounds for *in vitro* studies of their absorption, distribution, metabolism and excretion (ADME) properties. These properties are used to predict how accessible a compound will be *in vivo*. An ideal lead compound is then tested in animal models for its pharmacokinetic (PK) and pharmacodynamic (PD) properties. Although this approach has brought many drugs into clinical trials, a large number of them fail, where the calculated overall probability-of-success for an indication to go from Phase 1 to Phase 3 clinical stage and be approved is 3.4% (**Wong et al. 2019**). The drugs fail due to lack of efficacy or poor bioavailability, or the target may not be ideal, causing severe side-effects. The bottom line is that there is high risk associated with placing so much emphasis on targeting a specific protein and hoping that *in vivo* testing will show favorable outcomes.

1.4.3 “Top down” approach to drug discovery

An alternative approach to drug discovery involves screening compounds for phenotypic effects in cells or tissues without a specific target in mind. This approach stems from the acknowledgment that we are still limited in our understanding of how the majority of genes function inside a normal healthy cell, let alone in a diseased cancer cell. Letting the biology of cancer guide the selection process for an active compound that has higher efficacy in cancer compared to non-cancer cells increases the overall chances of success because the molecule already shows favourable properties in a cell-based assay (**Pickett 2006; Cronk 2013; Schenone**

et al. 2017). However, using large libraries of compounds often leads to a problem that persists in both cases, where they cannot be easily modified to improve their efficacy and/or drug-like properties due to limited flexibility in the chemistry. An ideal solution is to combine these approaches by placing emphasis on the design of the molecules to ensure that they have favourable *in vivo* properties, are amenable to modifications and cause toxicity in cancer cells.

1.4.3.1 Summary of thesis objectives

Using such an approach, our collaborator Dr. Pat Forgione (Department of Chemistry and Biochemistry) strategically designed a family of compounds that share a common thieonoisoquinoline scaffold and are amenable to modifications with properties ideal for *in vivo* use (**Chen et al. 2014**). Their design included the ability to probe molecular space common to biological targets. We screened the first group of derivatives for their toxicity in cancer cells and found one, Compound 75 (C75), with IC₅₀ viability values in the nanomolar range for HeLa cells and with ~2-fold selectivity compared to non-cancer HFF-1 cells, while the other derivatives had low/minimal effects. Thus, the activity caused by C75 is unique to the functional groups and is not a general feature of the core scaffold. These data encouraged us to further investigate C75's mechanism of action, and to identify new derivatives with improved efficacy.

In this thesis, I developed methodologies for high-throughput screening of new derivatives (Chapter 3), explored the mechanism of action of C75 in cells (Chapter 4), and studied the *in vivo* potential of C75 (Chapter 5). Despite the promise of C75, we acknowledge that a better derivative may be needed before moving toward clinical studies. In Chapter 3 I designed a way to screen derivatives with high reproducibility. Using the Genome Foundry at Concordia University, which houses a robotic infrastructure, I established methodology for the high-throughput plating of cells,

the addition of different concentrations of compounds with high precision, high content imaging of cells, and organization of data. This methodology has permitted us to screen >40 derivatives, and accurately determine their IC₅₀ for viability in A549 cells. Preliminary analysis of the cellular phenotypes caused by C75 suggested that it caused mitotic arrest with defective spindles. In Chapter 4, I performed in depth cell biological studies to better understand the effects of C75 in cells. Studies performed *in vitro* showed that C75 can bind to the colchicine-binding site on tubulin, prevents microtubule polymerization, and destabilizes previously assembled polymers. Despite having properties similar to colchicine *in vitro*, I found that C75 causes different effects on microtubules in cells. When added to metaphase HeLa cells, C75 causes the rapid depolymerization of microtubules, followed by spindle pole fragmentation, and microtubule re-growth to form multipolar spindles. Whereas colchicine causes the depolymerization of microtubules without recovery. In support of their different mechanisms of action, they enhance each other's spindle phenotypes and toxicity. Finally, in Chapter 5, I found that C75 has a particularly high efficacy in TNBCs, suggesting that they could be an ideal cancer to target with our compounds. To explore this concept, I found that C75 causes severe spindle phenotypes in TNBCs, and generated paclitaxel-resistant MDA-MB-231 cell lines to determine if C75 retains activity in these cells. In addition, we found a new derivative, C140, with even higher efficacy that could be explored for *in vivo* use.

Chapter 2: Material and Methods

2.1 Cell culture

HeLa, HFF-1, patient derived fibroblasts, MDA-MB-231 and Hs578t cells were grown in DMEM (Wisent), A549 cells were grown in F12K medium (Wisent), HCT 116 cells were grown in McCoy's medium (Wisent), BT-549 cells were grown in RPMI-1640 supplemented with 0.023 U/mL insulin, H1299 cells were grown in RPMI-1640 (Wisent), and MCF10A cells were grown in DMEM/F12 (Wisent) supplemented with 100 ng/mL cholera toxin (Cedarlane Cat# 100B), 20 ng/mL EGF (Wisent Cat# 511-110EU), 0.5 mg/mL hydrocortisone (Sigma-Aldrich Cat#4001) and 10 ug/mL insulin (Wisent Cat#511-016-CM) in humidified incubators at 37°C with 5% CO₂. All media were supplemented with 10% fetal bovine serum (FBS; Thermo Scientific), 2 mM L-glutamine (Wisent), 100 U penicillin (Wisent), and 0.1 mg/mL streptomycin (Wisent). All cell lines were grown as per instructions from the American Type Culture Collection (ATCC).

2.2 Drug Treatments

Paclitaxel (TaxolTM; Bioshop), vinblastine (Bioshop), colchicine (Sigma-Aldrich), nocodazole (Sigma-Aldrich) and all thienoisoquinoline derivatives were made into a 10 mM stock solution with dimethyl sulfoxide (DMSO). Subsequent dilutions of the thienoisoquinoline derivatives were made in either pure DMSO or DMSO:H₂O (9:1). Final concentrations of DMSO were kept below 5% for *in vitro* assays and between 0.03 – 0.1% in viability assays. Cells were treated with paclitaxel and nocodazole as previously described (**van Oostende Triplet et al. 2014**) and cells were treated with vinblastine and colchicine as previously described (**Dhamodharan et al. 1995; Jordan et al. 1992**). Cells plated in antibiotic-free medium were transfected with ch-TOG siRNA (Dharmacon) using Oligofectamine (Life Technologies).

2.3 Viability assays

Assays were performed as per manufacturer's instruction (Cayman Chemicals) to determine the viability of cells after treatment with C75 and/or colchicine. The concentration of colchicine or C75 used in the combination experiments was the highest concentration that caused little to no toxicity based on dose-response curves. HFF-1, patient derived fibroblast, HeLa, A549, HCT 116, BT-549, and MDA-MB-231 cells were plated at a final dilution of 4,000 cells/well in 96-well dishes and left overnight to adhere. Drug dilutions were prepared and added to the cells using an acoustic liquid handler (LabCyte Echo 550). After 3 population doubling times, cells were assessed for viability using the WST-8 cell proliferation assay kit (Cayman Chemicals). Absorbance readings at 450 nm were collected using the Tecan 200 Pro plate reader. Values for each replicate were adjusted to the controls and plotted using GraphPad Prism 7 to generate graphs and IC₅₀ values. All assays were performed in triplicate for each treatment. For the combination assays, C75 or colchicine were repeated alongside the combination treatments to ensure accurate comparison.

2.4 Microtubule assays

Microtubule polymerization assays were performed as per manufacturer's instructions using 1.5 mg/mL purified tubulin (Cytoskeleton, Inc) that was taken from a 10 mg/mL flash frozen stock, thawed on ice and diluted in G-PEM buffer (80 mM PIPES pH 6.9, 2 mM MgCl₂, 0.5 mM EGTA and 1 mM GTP with 20% glycerol) with 10% DMSO (control) or 250 nM C75. Assays were performed in a preheated 50 µL sub micro Z15 black Q/Spectrosil cuvette in a Varian Cary 1 spectrophotometer. Reagents were added to the cuvette and blanked immediately before recording absorbance at 340 nm in 0.1 second intervals for 45 minutes. We determined the effect

of C75 on polymerized microtubules by sedimentation. Lyophilized microtubules (Cytoskeleton, Inc) were reconstituted to 5 mg/mL in PM buffer (15 mM PIPES pH 7.0, 1 mM MgCl₂, and 2 mM paclitaxel) and aliquots were snap frozen in liquid nitrogen and stored at -80°C. Aliquots were thawed on ice in a circulating water bath, then diluted to 2 mg/mL in PM buffer at room temperature. Microtubules (1 μM) were incubated with 5 μM of C75, paclitaxel, or colchicine in a general tubulin buffer (80 mM PIPES pH 6.9, 2 mM MgCl₂, 0.5 mM EGTA) for 15 minutes. Then the samples were centrifuged at 16,000 x g for 1 hour. The supernatant and pellets were resuspended in sample buffer without SDS or DTT and analyzed by native PAGE on an 8% polyacrylamide gel. Colchicine-competition assays were performed with 2 μM purified tubulin (Cytoskeleton, 160 Inc) taken from a 10 mg/mL stock prepared in tubulin buffer as above, and the binding assays were performed with 1 μM colchicine or 1 μM colchicine with 500 nM C75 in 161 25 mM PIPES buffer, pH 6.8 in a 600 μL Q fluorometer cell, Z=20 (Varian) using a fluorescence spectrophotometer Cary Eclipse (Varian) at 25 °C for 3 hours. Reaction mixtures were excited at 350 nm and the emission was measured from 380 to 500 nm (**Bhattacharyya and Wolff 1974**). Emission values were collected at 30-minute intervals and normalized to the spectra recorded at time zero. All values were exported as excel files and graphs were generated in Prism V8.1.0 GraphPad.

2.5 Flow cytometry

Flow cytometry experiments were setup as per the open-source protocol from UC San Diego. Flow cytometry was used to measure changes in the proportion of cells in different stages of the cell cycle after C75-treatment. HeLa, HCT 116 and A549 cells were grown to 80% confluence and treated with a range of C75 concentrations for 8 hours. Cells were harvested in

Falcon tubes, then fixed with 70% cold ethanol and washed with cold phosphate buffered saline (PBS; Wisent). Cells were permeabilized and stained for 15 minutes at 37 °C with a solution containing 500 µg/mL propidium iodide (PI; Sigma) in PBS with 0.1% (v/v) Triton X-100 and DNase-free RNase A (Sigma). Cells were protected from light and measured for PI intensity using the BD LSRFortessa flow cytometer with excitation at 561 nm and detection at 600 nm (LP) using the D-BP filter. Each treatment was done in triplicate with 20,000 cells analyzed per sample. Data were exported and plotted using GraphPad Prism 7 to make bar graphs.

2.6 Immunofluorescence staining

Immunofluorescence staining was performed as per Yüce et al. 2005 to monitor mitotic spindle phenotypes. Cultured cells were plated on coverslips at a confluence of 40-50% and left overnight to adhere. Cells were fixed using freshly prepared ice-cold 10% w/v cold trichloroacetic acid (TCA) for 14 minutes at 4°C. Cells were washed with PBST (0.3% Triton X-100) and kept at 4°C prior to staining. After blocking in 5% normal donkey serum, fixed cells were immunostained for microtubules using 1:400 mouse anti- α -tubulin antibodies (DM1A; Sigma) or centrosomes using 1:400 mouse anti- γ -tubulin antibodies (Santa Cruz Biotechnology), and centromeres using 1:500 human anti-centromere antibodies (ACA; Sigma) for 2 hours at room temperature. After washing, anti-mouse Alexa 488 and anti-human Alexa 647 (Invitrogen) secondary antibodies were used at a 1:500 dilutions for 2 hours at room temperature. After washing, a 1:1000 dilution of 1 mg/mL 4',6-Diamidino-2'-phenylindole dihydrochloride (DAPI; Sigma) was added for 5 minutes. Cells were then washed with PBST, followed by a wash with 0.1 M Tris pH 9, then a drop of mounting medium (0.5% propyl gallate in 50% glycerol) was added to the coverslip, which was mounted onto a slide and sealed.

2.7 Microscopy

Fixed slides were imaged using the Nikon-TIE inverted epifluorescence microscope with Lambda XL LED light sources, using the 60x/1.4 oil objective, a Piezo Z stage (ASI), a Photometrics Evolve 512 EMCCD camera and Elements acquisition software (Nikon). Exposures were determined by control cells, and the same settings were used in the treatment conditions. Images were acquired as 1 μm Z-stacks and exported as TIFFs, which were opened as maximum intensity Z-stack projections in Image J (NIH). Merged colour images were converted into 8-bit images and imported into Illustrator (Adobe) to make figures. Live imaging was performed using techniques as previously described (van Oostende Triplet et al. 2014)

For live imaging, HeLa cells were plated to 50-60% confluence on 25 mm round coverslips (No. 1.5; Neuvitro). Cells were treated with 75 nM Hoescht 33342 and 200 nM SiR-tubulin (Cytoskeleton Inc.) for 90 minutes prior to imaging. Depending on the experiment, HeLa cells were transfected with a plasmid that expresses RNAi-resistant ch-TOG:GFP plus a hairpin RNA (sh ch-TOG) to knockdown endogenous protein and minimize overexpression (Addgene ID# 69113). HeLa cells stably expressing GFP:tubulin were generated previously (**van Oostende Triplet et al., 2014**). Coverslips were transferred to a 35 mm Chamlide magnetic chamber (Quorum) and kept at 37 °C with 5% CO₂ using an INU-TiZ-F1 chamber (MadCityLabs). Images were acquired using the 60x/1.4 oil objective on the Nikon Livescan sweptfield confocal microscope with an Andor iXon X3 EMCCD camera and Elements acquisition software (Nikon). The 405 nm, 480 nm and 640 nm lasers were used to image Hoescht 33342, GFP and sir-Tubulin, respectively, with a quad filter and exposures set to controls. Z-stacks of 1 μm were collected using a NI-DAQ piezo Z stage (National Instruments). Images were used to make figures as described above.

For cold-treated HeLa cells imaged in the presence or absence of C75 or colchicine, they were plated onto coverslips and transferred to a 35 mm chamlide magnetic chamber (Quorum), which was kept at in an ice-cold water bath for 30 minutes to cause spindle collapse. After 30 minutes the chamber with cells was transferred to 37 °C with 5% CO₂ using an INU-TiZ-F1 chamber (MadCityLabs) and the drug was added after acquisition of the first timepoint. Images were acquired using the 60x/1.4 oil objective on the Nikon Livescan sweptfield confocal microscope with an Andor iXon X3 EMCCD camera and Elements acquisition software (Nikon). The 405 nm and 480 nm lasers were used to image Hoescht 33342, GFP:tubulin respectively, with a quad filter and exposures set to controls. Z-stacks of 1 μm were collected using a NI-DAQ piezo Z stage (National Instruments). Images were used to make figures as described above.

2.8 Analysis

For the analysis of phenotypes in the Figures 16, 18, 19 and 22, either whole fields of view (Figure 16A) or z-stack projections of individual cells were used (**Figures 16B, C, D, 18A, B, C, 19B, 22A, B**). To calculate the proportion of mitotic cells based on cell rounding (Figure 16A) we counted the following number of HeLa cells on average: 0 nM n=568, 100 nM n=847, 200 nM n=266, 300 nM n=105, 400 nM n=96, 500 nM n=75), A549 cells: 0 nM n=461, 100 nM n=519, 200 nM n=181, 300 nM n=154, 400 nM n=150, 500 nM n=253), and HCT 116 cells: 0 nM n=813, 100 nM n=742, 200 nM n=297, 300 nM n=296, 400 nM n=314, 500 nM n=301 (N=4 experimental replicates). To calculate the proportion of cells with different mitotic spindle phenotypes (**Figure 16B and C**), the following number of HFF-1 cells were counted on average after treatment with DMSO n=28, 300 nM C87 n=24 and 300 nM C75 n=13, HeLa cells after treatment with

DMSO n=45, 300 nM C87 n=36 and 300 nM C75 n=109, A549 cells with DMSO n=29, 300 nM C87 n=32 and 300 nM C75 n=63, and HCT 116 cells with DMSO n=41, 300 nM C87 n=32 and 300 nM C75 n=66 (N=3 experimental replicates). Fewer HFF-1 cells were analyzed compared to the other cell lines due to low proportion of mitotic cells in the population. To determine the number of centrin-2-positive foci in HeLa cells (**Figure 16D**), an average of 25 cells were counted for the control (DMSO-treated) and 30 cells after treatment with 300 nM C75 (N=3 experimental replicates). To calculate changes in the proportion of mitotic spindle phenotypes in HeLa cells after treatment with C75 and/or colchicine (**Figures 18A and B**), we counted the following average numbers of cells: DMSO n=51, 20 nM colchicine n=62, 50 nM colchicine n=72, 100 nM colchicine n=78, 100 nM C75 n=42, 200 nM C75 n=46, 300 nM C75 n=59, 400 nM C75 n=69, 500 nM C75 n=65, 100 nM C75 + 20 nM colchicine n=70, 200 nM C75 + 20 nM colchicine n=89, 300 nM C75 + 20 nM colchicine n=94, 400 nM C75 + 20 nM colchicine n=98 and 500 nM C75 + 20 nM colchicine n=83 (N=3 experimental replicates). To calculate changes in the proportion of mitotic spindle phenotypes in HCT 116 cells after treatment with C75 and/or colchicine as above (**Figure 18C**), we counted the following average number of cells: DMSO n=44, 20 nM colchicine n=39, 50 nM colchicine n=54, 100 nM colchicine n=51, 100 nM C75 n=42, 200 nM C75 n=40, 300 nM C75 n=82, 400 nM C75 n=56, 500 nM C75 n=65, 100 nM C75 + 20 nM colchicine n=43, 200 nM C75 + 20 nM colchicine n=52, 300 nM C75 + 20 nM colchicine n=69, 400 nM C75 + 20 nM colchicine n=76 and 500 nM C75 + 20 nM colchicine n=81 (N=3 experimental replicates). To count the proportion of cells with multipolar or bipolar spindles in HeLa cells after release from C75 or colchicine (**Figure 19B**), we counted the following number of average cells: DMSO n=61, 500 nM C75 n=50 and 500 nM colchicine n=64 (N=3 experimental replicates). To determine the proportion of cells with mitotic spindle phenotypes and compare these to ch-TOG RNAi treatment

(Figure 22A and B), we counted the following number of average cells: DMSO n=81, 200 nM C75 n=242, 300 nM C75 n=143, ch-TOG RNAi n=534 (N=3 experimental replicates). To determine synergy for the viability of cells treated with C75 and colchicine in combination, CompuSyn software was used (**Figure 17A, B**). We used the non-constant ratio method of analysis since the concentration used for the combination studies was selected based on the highest concentration without lethality. The analysis indicated what combination of drug concentrations yielded an antagonistic, synergistic and additive effect based on the well-documented combination index (CI) described by the Chou-Talalay method (**Chou 2010**). To determine the effect of C75 on spindle poles, HeLa cells stably expressing GFP:Tubulin and or ch-TOG:GFP; sh ch-TOG were used to measure changes in spindle volume and maximum intensity after upshift from cold treatment to recover depolymerized microtubules in the presence of C75 or colchicine. To do this, we used the spot analyzer function in Imaris 9.5.1 (Bitplane), with parameters set to measure local contrast between the spindle pole and surrounding cytosol, which defined the pole boundaries. Values were exported and organized in csv format using a macro in Python 3.0 to extract the volume and maximum intensity of each pole. The csv files were then imported into GraphPad Prism 7 to build graphical representations, including heat maps, bar graphs and distribution plots. Statistical analyses were also done in GraphPad Prism 7, to determine the significance between slope distributions using the Welch's two-tailed t test with a 99% confidence interval ($p<0.0001$). Peaks corresponding to changes in spindle pole volume were determined for each pole using the built-in function "findpeaks" in MatLab R2017b. The parameters were set to identify any peaks that corresponded to a change in volume with an amplitude $\geq 20\%$. Identified peaks were then tabulated in Excel (Microsoft) and imported to GraphPad Prism 7 for graphical representation.

2.9 Metabolism profile of C75

A metabolism assay was performed as per a protocol obtained from Dr. Dajana Vuckovic laboratory (Concordia University) to determine the metabolites that are produced when C75 is in the presence of liver enzymes. For the Phase 1 metabolism profile, 5 µL of mice liver microsomes (MLM; S9 fraction; ThermoFisher) were incubated with 5 µM C75, 12 µL of a 20 mM NADPH solution (Sigma Aldrich) and 182 µL of PBS buffer. A similar setup was used for negative controls. The solutions were incubated for 0 and 60 minutes, and aliquots were taken and stopped via heat inactivation. For the Phase 2 metabolism profile, the same setup was used as in Phase 1, with the addition of 1 µL of 5 mg/mL of alamethicin solution (Sigma-Aldrich), 10 µL of a 100 mM solution of UDPGA (Sigma-Aldrich) and 10 µL of a 100 mM solution of MgCl₂. A similar design was used for negative controls. The solutions were incubated for 0 and 60 minutes where aliquots were taken and stopped via heat inactivation. The Phase 1 and 2 samples were then analyzed using LC-MS and the data was imported into Compound Discoverer 3.0 for analysis using its pre-programmed protocol for the detection and measurements of the metabolites.

2.10 Developing Taxol-resistant cell lines

Several MDA-MB-231 cell lines with resistance to different concentrations of paclitaxel were generated using similar methodologies previously described (**Zhang et al. 2010**). Cells were plated in 100 mm dishes with the appropriate cell culture media until they reached 80% confluency. The cells were then treated with 20 nM paclitaxel for 48 hours, after which the media was replaced with drug-free media. The cells were left to recover for another 48 hours. They were then trypsinized and re-plated in new dishes with fresh media and left for 48-72 hours. Subsequent treatments were done in a similar fashion using increasing concentrations of paclitaxel (60 nM and

100 nM). Depending on the number of remaining cells after selection, they were given more time to recover and replenish the cell population. MDA-MB-231 cells resistant to 20 nM, 60 nM and 100 nM paclitaxel were then frozen for storage.

2.11 Illustrations and cartoon schematics

The cartoons and illustrations in this thesis were made using Adobe Illustrator 2015-2020. All of the cartoon schematics are original and/or modified extensively from the original and cited appropriately.

Chapter 3: Discovering a novel anti-cancer compound

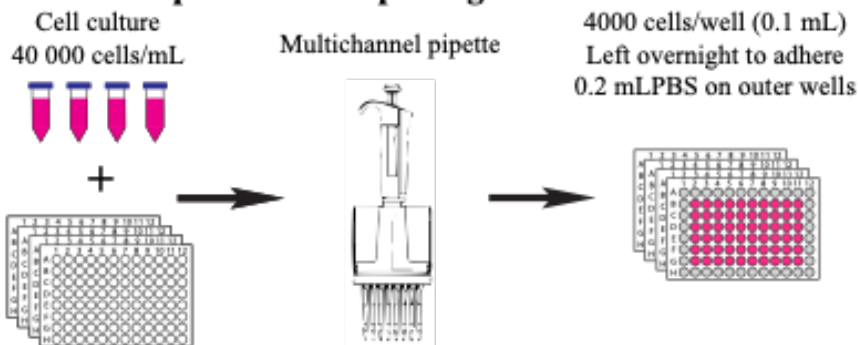
3.1 Developing a High-Throughput Screening (HTS) pipeline

As outlined earlier, we collaborated with Dr. Pat Forgione (Department of Chemistry and Biochemistry at Concordia) to develop a new family of anti-cancer compounds. These initial derivatives, which share a common thienoisoquinoline scaffold, were screened by our group for cancer cell toxicity (**Chen et al. 2014**). Based on promising results from this first screen and the identification of a derivative with high efficacy, they generated new derivatives. To efficiently screen these new compounds, we had to develop methodology that would enable high reproducibility using multiple cell lines with a range of concentrations, and multiple replicates.

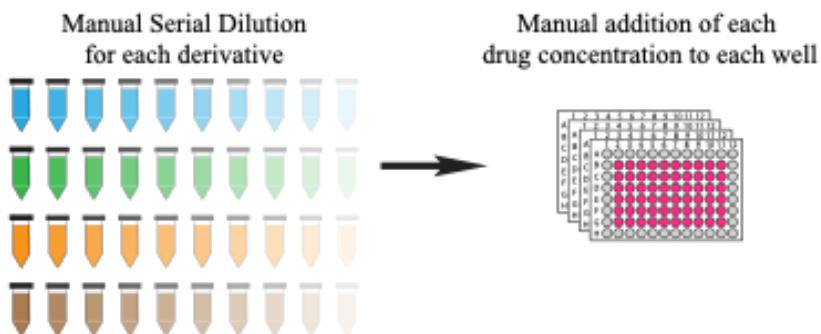
Concordia University recently built a Genome Foundry with an infrastructure that has the capacity to conduct molecular research in a high-throughput fashion. These instruments are task-specific, which enables users to effectively learn and implement them in their routine experiments. Using these instruments from the Foundry and from the Center of Microscopy and Cellular Imaging (CMCI), I developed a method for screening new derivatives to determine their effect on cell viability with high efficiency and reproducibility, while decreasing the overall cost typically associated with screening libraries of compounds in various cancer cell lines. The goal of this methodology was to replace steps typically carried out manually (Figure 7) with the equivalent automation, to reduce the need to use higher volumes and to improve the speed and precision at which components are added. These machines and software were used to set up viability assays via diluting libraries of compounds, performing imaging, data processing, as well as organizing and performing a comparative analysis of the data (Figure 8).

The following steps were automated and/or developed as described to perform viability assays; 1) liquid handling to plate cells in 96-well plates, 2) liquid handling to add varying

Day 1 - Cell Preparation and plating



Day 2 - Drug addition



Day 5 - Viability measurement

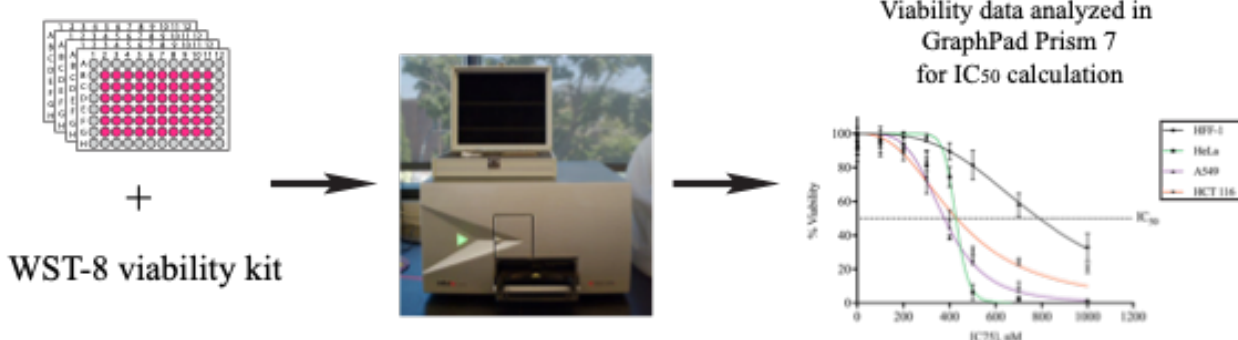
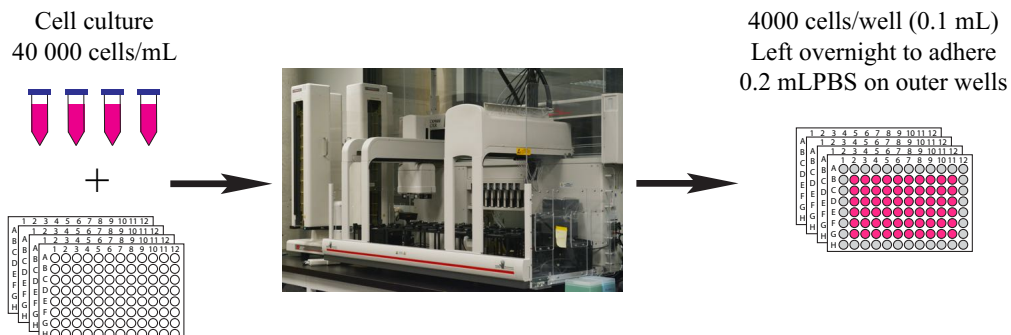
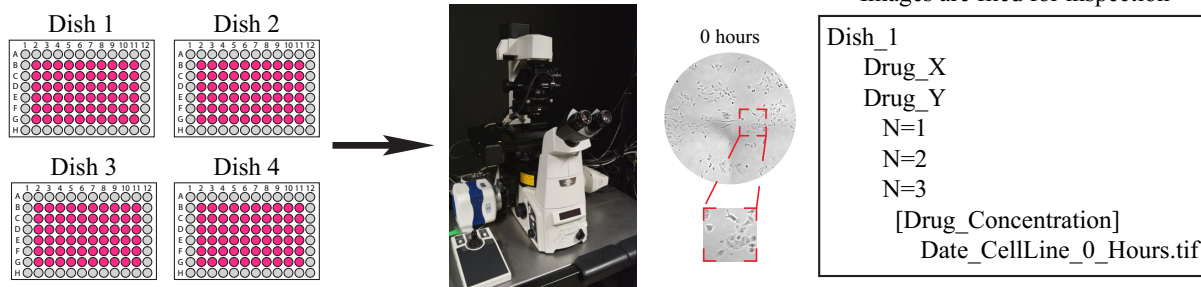


Figure 7. Low-throughput workflow to determine cell viability. Schematics show the workflow of the different steps required to conduct a viability assay manually. On Day 1, the cells are plated using a multichannel pipettor to a final concentration of 4,000 cells/well. On Day 2, manual pipetting is used to add the different concentrations of compounds to each well. A serial dilution of each compound is prepared in microfuge tubes, to cover the entire range needed for the logarithmic determination of IC₅₀ values. On Day 5, viability is measured by adding WST-8 and measuring colorimetric changes in the media via the TECAN plate reader. These values are exported in Excel spreadsheets and used to generate graphs in GraphPad Prism. Amanda Michel took the picture of the TECAN plate reader.

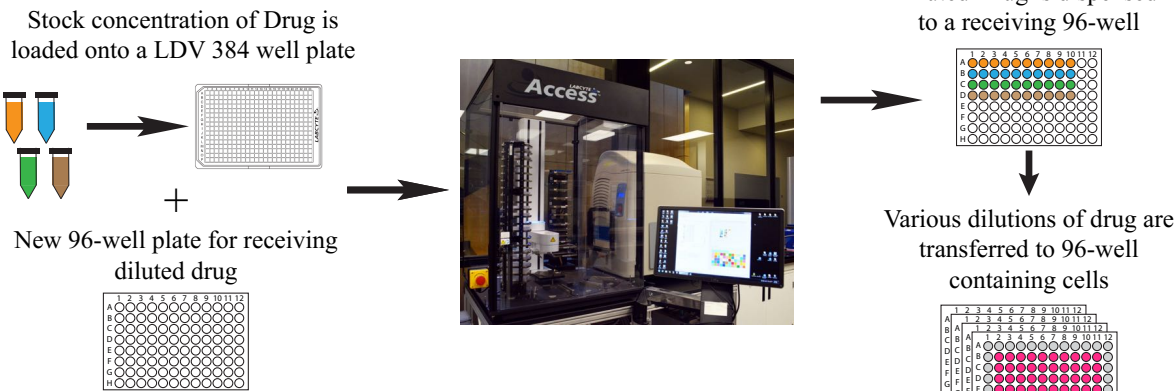
Day 1 - Cell Preparation and plating



Day 2 - Part 1: Imaging at 0 hours



Day 2 - Part 2: Drug addition



Day 3, 4, 5 - Imaging at 24, 48 and 72 hours

Day 5 - Viability measurement

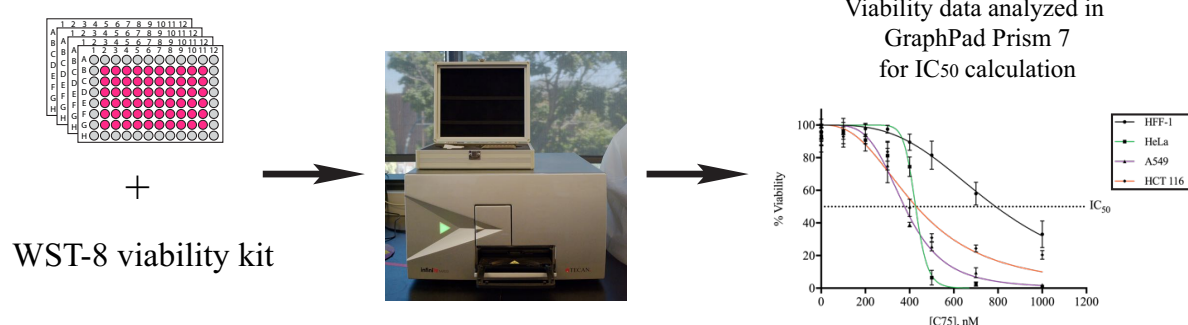


Figure 8. High-throughput workflow to determine cell viability. Schematics show the workflow to determine IC₅₀ values using automated instrumentation in the Genome Foundry and CMCI. On Day 1, cells are plated to a final concentration of 4,000 cells/well using the BioMek liquid handler. On Day 2, compounds of varying concentrations are added to each well using the ECHO liquid handler. On Days 3, 4 and 5, high content imaging is performed using the Nikon TiE Eclipse inverted microscope. Images are organized using a GUI interface (not shown here). On Day 5, metabolic assays are performed by measuring colorimetric changes after WST-8 addition using the TECAN plate reader. Amanda Michel took the pictures of the instruments.

concentrations of each compound in triplicate, 3) high content imaging the cells in each well, 4) spectroscopy using a plate reader, and 5) the organization of data and analysis.

The BioMek liquid handler is used to dispense media containing cells into the wells of a 96-well plate. The cells used for plating are counted and diluted to achieve a final number of 4,000 cells/well. The instrument accurately dispenses 100 µL of cell culture to the inner wells, and PBS to the outer wells. This is done with an adjustable rate of expulsion to minimize microcurrents, which is a major issue with manual dispensing. Due to the time needed for cells to adhere to the bottom of the well, microcurrents can cause cells to settle in clumps and at the edges of the well, which hinders their growth and impacts results from drug treatment. After dispensing cells, the BioMek liquid handler stores the plates for their retrieval, which takes 30 minutes for four 96-well plates. The time saved using this instrument is exponential compared to manual dispensing.

Manually pipetting the compounds to each well introduces additional variability. To circumvent this, the ECHO liquid handler uses multiple controlled bursts of sound against their specially designed 384-well low dead volume (LDV) plates to launch 2.5 nL microdroplets into the receiving 96-well plate. The instrument initially determines the volume and composition of the solvent that the compound is diluted in (*e.g.* 90-100% DMSO) which allows it to adjust the force required from the sound wave to dispense the microdroplet. Little-to-no manual dilutions are required using this method, which can dispense small volumes from a stock solution and maintain final DMSO concentrations in a range of 0.03-0.1%. This is crucial because DMSO can impact cell health and higher concentrations can skew results. While levels below 5% are generally considered acceptable, we try to keep these levels as minimal as possible as different cell lines could have different sensitivities. In addition to adding precise, small volumes, the ECHO liquid handler greatly reduces the time spent diluting compounds by at least a factor of 12. For example,

making 6 dilutions for 10 derivatives to keep the volume of DMSO below 5% typically requires the use of 60 microfuge tubes, a large number of pipette tips, loss of precious stock, and 1.5 to 2 hours of constant pipetting where the errors associated with pipetting are compounded. The ECHO liquid handler only uses 2 different concentrations (*i.e.* 10 mM and 1 mM/derivative), requires 12 µL of the stock solution, and dispenses all of the compounds at the required concentration in under 10 minutes while maintaining a final concentration of DMSO (0.03-0.1%) for each derivative.

To monitor the impact of each compound on cell viability, we use two assays. One assay involves measuring changes in metabolic activity using WST-8, which is described below and is more quantitative. The other assay relies on using microscopy to confirm that there is a change in the number of cells in the treated wells and aligns with the metabolic assay as a qualitative read-out for viability. To do this we use a fully automated Nikon Eclipse TiE Inverted microscope to image the cells in each well. This allows us to identify any issues regarding cell confluence, cell distribution, contamination, and consistency between wells when monitoring the effect of the drugs. Although the acquired data is qualitative, since the cells are treated over 3 population doublings, it gives us more confidence in the metabolic assays and permits us to terminate the experiment if any issues are found that can reduce the use of reagents and time. The wells of each plate are imaged with a 4x objective that captures four quadrants of the well to cover approximately 80-90% of the well's surface and stitches them together to create a single image of the well. Before the plate is imaged, the user places the 96-well plate onto the microscope stage and the centre of the first well is determined using automated focusing to allow the system to build a virtual map of all the wells and register the XY co-ordinates for the center of each well. With the wells in focus the system images the plate without requiring additional user input, and the user returns the plate

to an incubator once imaging is complete. The plates are imaged once every 24 hours and the images for each well are organized and stored into an appropriate file system for easy retrieval.

A graphical user interface (GUI) was developed with Christian Sanchez (a BIOL 490 student) to enable the user to easily monitor the images collected by microscopy. The GUI accesses the library of organized pictures acquired by the TiE based on the user's selection of treatment and cell line and displays the full course of the experiment. Although this information is qualitative, it shows the user how the treatment affects the population of cells, when mitotic arrest (or other phenotypes) occurs, and factors that could affect interpretation of the experiment. The technical schematic of the GUI's back-end is illustrated in Figure 9, where it shows the final output once the user calls upon an experiment.

As mentioned above, the cells in each well are also assayed for changes in metabolic activity. After three population doubling times, the wells of each plate are treated with the colorimetric reagent, WST-8, which measures the metabolic activity of cells and is used to determine the proportion of cells that are viable compared to cells in the control wells. The WST-8 tetrazolium salts are reduced by NAD(P)H to form an orange formazan salt that solubilizes in the media, which is a direct measurement of dehydrogenase enzyme activity in the cell (**Chamchoy et al. 2019**). The amount of orange formazan salt is proportional to the viability of the cells, where the control wells have the highest amounts and are used to normalize the plate to 100% viability. After 2-4 hours of incubation, the wells are measured by spectrophotometry at 450 nm using the TECAN plate reader. Multiple readings are obtained per well and averaged to ensure accuracy. The spectrophotometry data was compiled into Microsoft Excel spreadsheets where a macro is used to organize the raw data into a usable format and transferred to GraphPad and/or CompuSyn for more in-depth analysis. Graph Pad Prism is extremely powerful for data processing

A

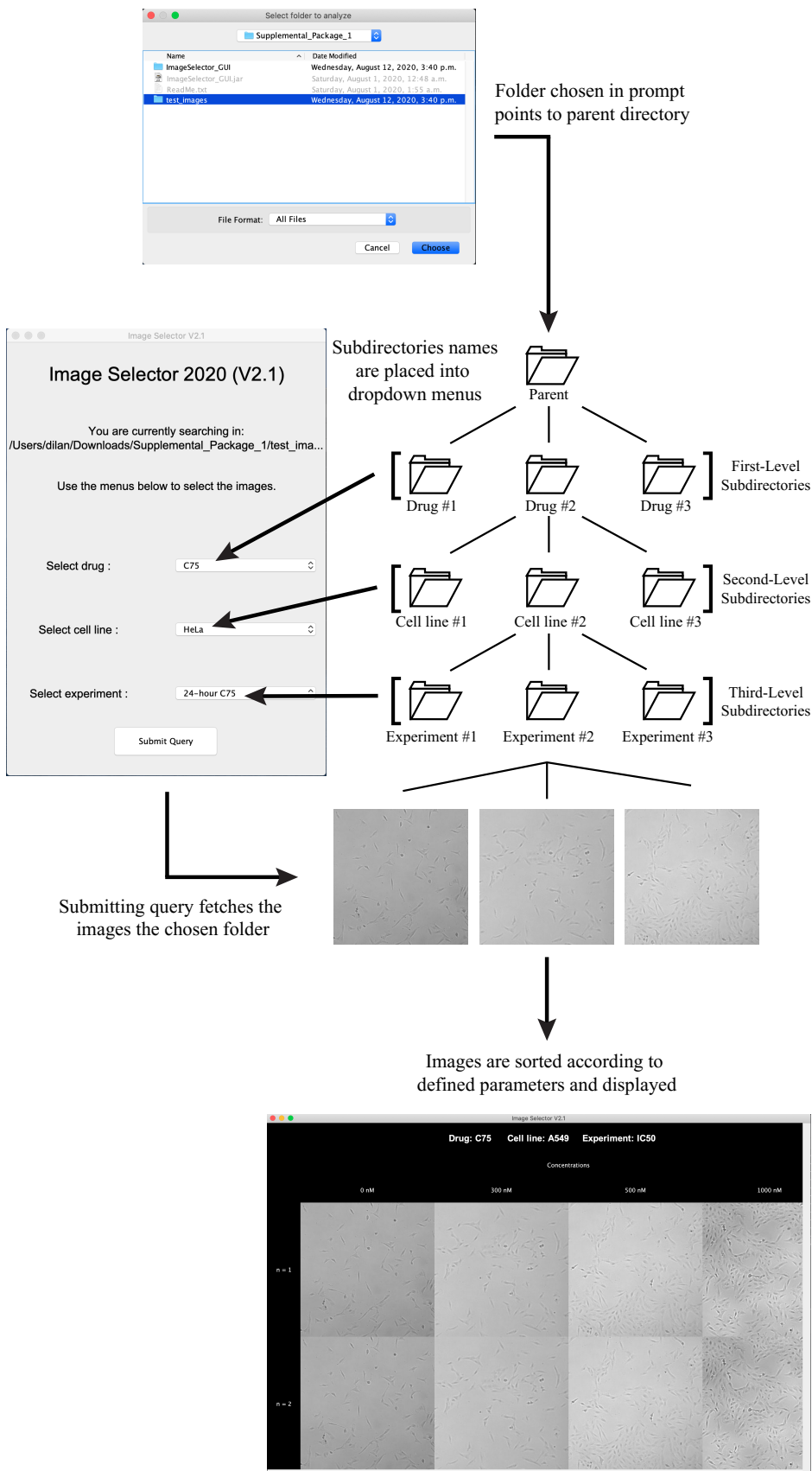


Figure 9. An overview of the GUI design to organize images. A) Flow chart of how to use the GUI for fetching and displaying images of any viability experiments. The GUI accesses a database of all the images acquired throughout the viability assay and displays it for the user to assess progression of the experiment. Once the program is launched it requires input to which directory the image database is located in and the prompts the user to input parameters such as, drug, cell line and experiment. Once the query is submitted it displays the whole experiment in a single window for viewing and inspection by the user. Credits for the flow chart and development of the GUI goes to Christian Sanchez-Espinoza.

and has statistical analysis functions that are based on the experimental design. In addition, CompuSyn offers the user the ability to simulate and calculate how two drugs interact with one another, to define when they are synergistic, antagonistic or additive using a unified theory of biochemical and biophysical equations that include the Scatchard equation, Henderson-Hasselbalch's equations, Michaelis-Menten's equation and Hill equation. It is by far the most intricate conceptualization of combinatorial drug treatments, which considers the most important factors for such an experiment.

3.2 Determining derivatives that affect the viability of cancer cells

Some of the data is included in the following patents:

- Forgione, P. (40%), Piekny A. (40%), *Jauny D., *Larocque, K., Chen F. and L. Jiang. Thienoisoquinolines and their derivatives for targeting tubulin, ch-TOG, Aurora A Kinase or TPX2. PCT Patent Application 62681093 – P54735PC00 filed June 12, 2018
- Forgione, P. (40%), Piekny A. (40%), Jauny D., Chen F. and L. Jiang. Thienoisoquinolines and their derivatives for the treatment of cancer. PCT U.S. Patent Application 14863-P51477PC00 filed June 12, 2017

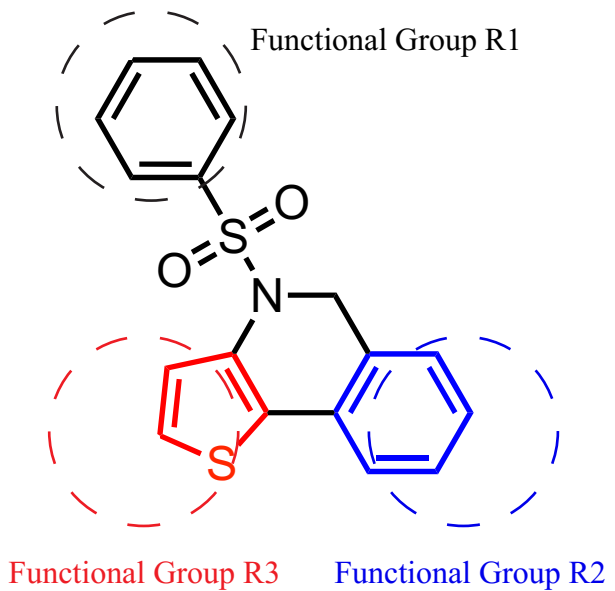
Using the methodology described in 3.1, I screened multiple thienoisoquinoline derivatives. Most of the derivatives (44 out of 54) were screened to determine their IC₅₀ for viability in A549 cells, while I also screened C87 in HeLa (cervical carcinoma), HCT 116 (colorectal carcinoma) and HFF-1 (fibroblast) cells, C75 in HeLa, HCT 116, HFF-1, PDF (fibroblast), BT-549 (ductal carcinoma), MCF10A (fibrocystic disease of the breast), and MDA-MB-231 (adenocarcinoma) cells, and C140 in MDA-MB-231 and BT-549 cells. Given their ease of culturing without clumping and response to active derivatives, A549 was chosen as the main cell line for screening the family of compounds. As described earlier, the design of the scaffold permits modifications at three different functional groups (**Figure 10A**). Identifying the impact of distinct chemical

moieties at each site is crucial to guide SAR studies to optimize their design and identify a lead compound with high efficacy and selectivity.

The screened derivatives displayed a range of activity which could be attributed to specific modifications at one of three functional groups (R1, R2, and R3). For example, some had high activity had $IC_{50} < 500$ nM, while others had more moderate activity between 500-1,000 nM, and others had little/no activity with $IC_{50} > 1000$ nM. The gain or loss of activity after modification of one of the R groups helped to identify those that are crucial. For example, C87, 153 and 155, which lack one or more of the functional groups compared to C75 had IC_{50} values of 7,000, 5,242 and >10,000 nM, respectively, compared to 369 nM for C75 (**Figure 10B**).

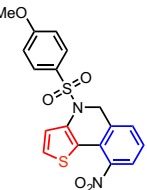
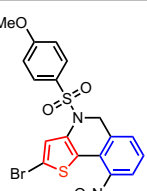
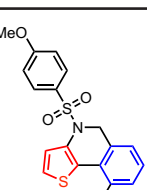
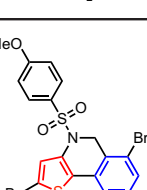
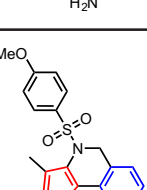
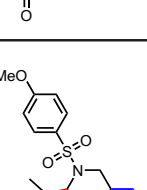
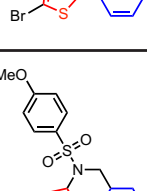
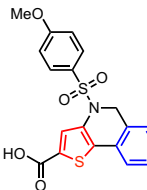
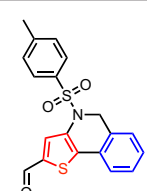
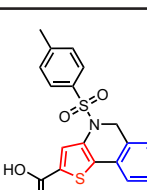
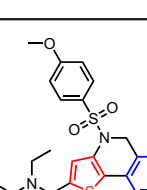
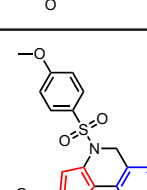
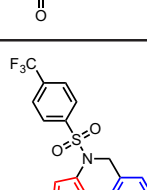
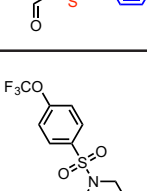
We identified several active compounds with IC_{50} values under 500 nM. These were C75, C138, C140, C145, C158, C160, C173, C174, C207, 208 and C401 with IC_{50} values of 369, 416, 260, 295, 70, 195, 172, 223, 433, 434, and 383 nM, respectively (**Figure 10B**). C75 was identified early in the screen and guided the strategic design of subsequent derivatives such as C128*, C138, C140, C145, C207 and C208 to explore the R3 functional group. These more active derivatives (*except C128, which was 549 nM) favor electronegative groups such as halogens (Br: 2.8, I: 2.5, Cl: 3.0) and oxygen (O: 3.5). This property could signal that the pocket where the R3 group binds on the target is positively charged and facilitates ionic interactions. Another feature that is favored in the active derivatives is the presence of an O-methyl group (O-Me; C75, C127, C128, C138, C140, C207, and C208) or O- (C145, C158, C160, C174, and C401) at the R1 position. When this was removed or replaced with just a methyl group, the activity of the compound depended more strongly on the R3 position. Interestingly, C154, which has Bromine at the R3 position has little activity, but C142 with oxygen at the R3 position retains high activity with a methyl group at R1

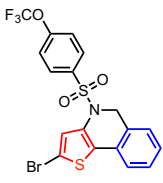
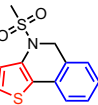
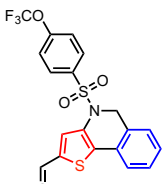
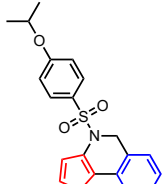
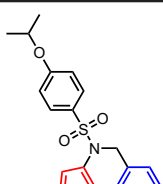
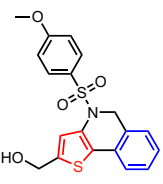
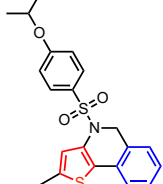
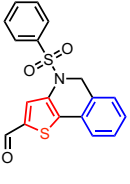
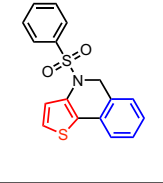
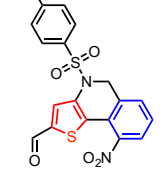
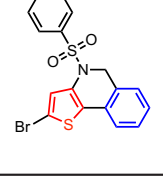
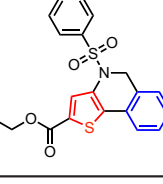
A



B

	C39 MW: 341.443 CLogP: 5.057	A549: 4420 nM		C87 MW: 333.438 CLogP: 4.279	A549: 7000 nM HeLa: >10,000 nM HCT116: >10,000 nM HFF-1: >10,000 nM
	C39-1 MW: 421.347 CLogP: 5.057	A549: 2289 nM		C90 MW: 357.442 CLogP: 4.727	A549: 780 nM
	C71 MW: 417.541 CLogP: 7.155	A549: >10,000 nM		C91 MW: 341.443 CLogP: 5.057	A549: 3380 nM
	C72 MW: 447.567 CLogP: 7.102	A549: >10,000 nM		C108 MW: 395.414 CLogP: 5.441	A549: >10,000 nM
	C74 MW: 420.339 CLogP: 6.024	A549: 2086 nM		C109 MW: 383.524 CLogP: 6.384	A549: >10,000 nM
	C75 MW: 436.338 CLogP: 5.694	A549: 369 nM HeLa: 427 nM HCT116: 431 nM HFF-1: 789 nM BT-549: 185 nM MCF 10A: 363 nM MDAMB231: 263 nM PDF: 1160 nM		C127 MW: 371.469 CLogP: 5.226	A549: 635 nM
	C80 MW: 467.601 CLogP: 8.329	A549: >10,000 nM		C128 MW: 405.911 CLogP: 6.031	A549: 549 nM

	C130 MW: 402.439 CLogP: 4.501	A549: >10,000 nM
	C131 MW: 481.335 CLogP: 5.447	A549: >10,000 nM
	C132 MW: 372.457 CLogP: 3.540	A549: 2275 nM
	C133 MW: 530.249 CLogP: 5.614	A549: 6621 nM
	C138 MW: 399.479 CLogP: 4.967	A549: 416.4 nM
	C139 MW: 450.365 CLogP: 6.193	A549: 2819 nM
	C140 MW: 385.452 CLogP: 4.469	A549: 260 nM MDAMB231: 127 nM
	C141 MW: 401.451 CLogP: 4.670	A549: >10,000 nM
	C142 MW: 369.453 CLogP: 4.799	A549: 456.2 nM
	C143 MW: 385.452 CLogP: 5.000	A549: 4261 nM
	C144 MW: 456.575 CLogP: 4.559	A549: >10,000 nM
	C145 MW: 415.478 CLogP: 4.951	A549: 295 nM
	C146 MW: 423.424 CLogP: 5.182	
	C147 MW: 411.413 CLogP: 5.836	A549: >10,000 nM

	C148 MW: 490.309 CLogP: 6.803		C155 MW: 265.345 CLogP: 2.779	A549: >10,000 nM
	C149 MW: 439.423 CLogP: 5.577		C156 MW: 344.241 CLogP: 3.746	A549: >10,000 nM
	C150 MW: 385.496 CLogP: 5.565		C157 MW: 293.355 CLogP: 2.521	A549: >10,000 nM
	C151 MW: 464.392 CLogP: 6.532		C158 MW: 387.468 CLogP: 3.680	A549: 70 nM
	C152 MW: 413.506 CLogP: 5.306		C159 MW: 355.426	A549: 1064 nM
	C153 MW: 327.416 CLogP: 4.558		C160 MW: 430.490 CLogP: 4.227	A549: 195 nM
	C154 MW: 406.312 CLogP: 5.525		C161 MW: 429.505 CLogP: 5.479	A549: 1000 nM

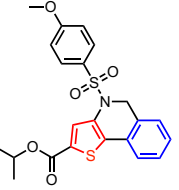
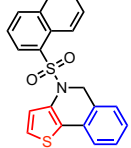
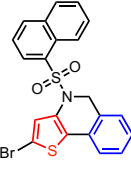
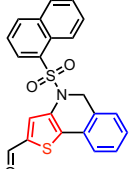
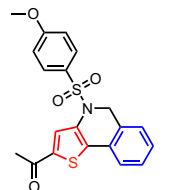
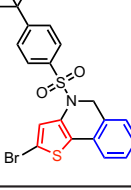
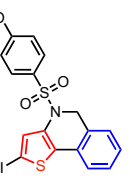
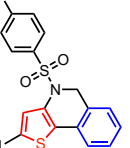
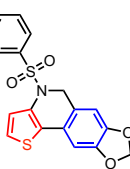
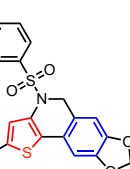
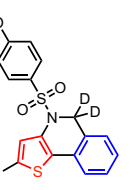
	C162 MW: 443.532 CLogP: 5.788	A549: 5758nM	
	C170 MW: 385.496 CLogP: 5.565		
	C171 MW: 464.392 CLogP: 6.532		
	C172 MW: 413.506 CLogP: 5.306		
	C173 MW: 399.470 CLogP: 4.470	A549: 172 nM	
	C174 MW: 382.450 CLogP: 4.501	A549: 223 nM	
	C201 MW: 462.420 CLogP: 7.351		
	C207 MW: 483.338 CLogP: 5.954		A549: 433 nM
	C208 MW: 391.884 CLogP: 5.544		A549: 434 nM
	C300 MW: 401.451 CLogP: 4.709		A549: >10,000 nM
	C301 MW: 480.347 CLogP: 5.666		A549: 3932 nM
	C401 MW: 438.25 CLogP: 5.694		A549: 383 nM

Figure 10. Structures show the thienoisoquinoline derivatives synthesized for this study. A)

A schematic shows the core scaffold and the functional groups amenable to modifications (R1, R2 and R3). **B)** Tables show the synthesized derivatives with their corresponding IC₅₀ values in A549, and/or other cell lines, CLogP values and molecular weights (MW). Peter Liu provided schematics of the derivatives.

(Figure 10B). This suggests that the R1 moiety also can impact how the compound binds to the target and needs to be considered in the design of the lead compound.

While some of these active derivatives were only recently identified, C75 had been discovered as an active derivative early on. Thus, our efforts focused on further characterizing C75 at the molecular and cellular level. These studies included comparing its efficacy in different cell lines to determine if it is selective for some cell types compared to others. I found that the IC₅₀ value for C75 in human foreskin fibroblasts (HFF-1) and human derived fibroblasts (HDF) is 789 and 1160 nM, respectively (**Figure 10B**). Thus, C75 is ~2-4-fold more selective for A549 cells compared to fibroblasts. I also determined the IC₅₀ for C75 in other cell lines including HeLa (427 nM), HCT 116 (431 nM), BT-549 (185 nM), MCF10A (363 nM), and MDA-MB-231 (263 nM) cells (**Figure 10B**). All are derived from cancers except for MCF10A, which are derived from fibrocystic disease. These cells are not considered to be cancerous but have aneuploidy and are not considered ‘normal’. The increased efficacy of C75 toward TNBCs is encouraging and will be explored further in Chapter 5. However, we are continuing to synthesize and evaluate new derivatives. A lead compound should have high efficacy and selectivity, and properties ideal for *in vivo* use that include solubility (CLogP).

3.3 Characterizing the anti-cancer properties of C75

Some of the data is included in the following patents:

- Forgione, P. (40%), Piekny A. (40%), *Jauny D., *Larocque, K., Chen F. and L. Jiang. Thienoisoquinolines and their derivatives for targeting tubulin, ch-TOG, Aurora A Kinase or TPX2. PCT Patent Application 62681093 – P54735PC00 filed June 12, 2018
- Forgione, P. (40%), Piekny A. (40%), Jauny D., Chen F. and L. Jiang. Thienoisoquinolines and their derivatives for the treatment of cancer. PCT U.S. Patent Application 14863-P51477PC00 filed June 12, 2017

We identified several active thienoisoquinoline derivatives with IC₅₀ values <500 nM in A549 cells. As described above, C75 was identified early in our screen and given its efficacy and selectivity for some cells compared to others, we further characterized its effect in cells. These studies formed the foundation for more rigorous experiments to determine its mechanism of action, which are described in Chapter 4.

One of our first observations was that C75 causes cells to arrest in mitosis. HeLa and HFF-1 cells were treated with increasing concentrations of C75 for 8 hours. While we saw an increase in the proportion of HeLa cells in mitosis treated with 200 nM of C75, we only saw an increase in mitotic HFF-1 cells with 500 nM of C75 (**Figure 11A, B**). When these cells were fixed and stained for tubulin, HeLa cells treated with 300 nM of C75 showed dramatic changes in the morphology of the mitotic spindle, while HFF-1 cells looked similar to control (**Figure 11C**). However, both cell types had a strong reduction in microtubules, and fragmentation of spindle poles when treated with 500 nM of C75 (**Figure 11C**).

Next, we determined if C75 causes similar phenotypes in other cell types (**Figure 12A**). We treated HeLa, HFF-1, H1299 (non-small cell lung cancer), MCF10A (fibrocystic disease), MCF7 (breast cancer – ER+), BT-549 (TNBC), A549 (lung carcinoma) and HCT116 (colorectal carcinoma) cells with 300 nM C75, or an inactive derivative (C87) for 8 hours. Depending on the cell line, we observed spindle phenotypes that could be categorized as disorganized spindles (e.g. monopolar, or bipolar with unequal microtubule distribution) with microtubules, or fragmentated spindle poles with few microtubules (**Figure 12A**). Interestingly, H1299, MCF10A and MCF7 cells had robust microtubules, while BT-549, A549, and HCT116 cells showed more dramatic loss of microtubules. The latter are cell lines obtained from more aggressive cancers and could reflect genetic changes that make their microtubules more susceptible to treatment with C75.

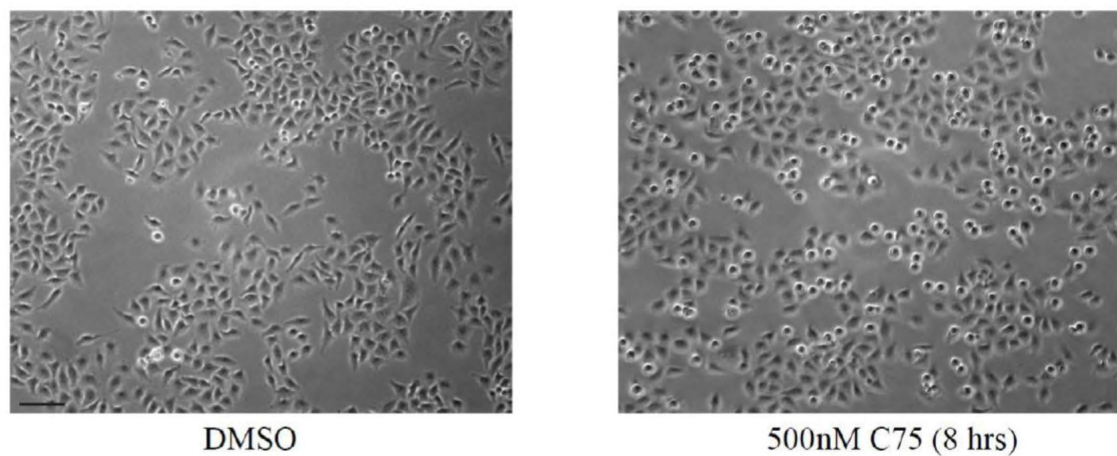
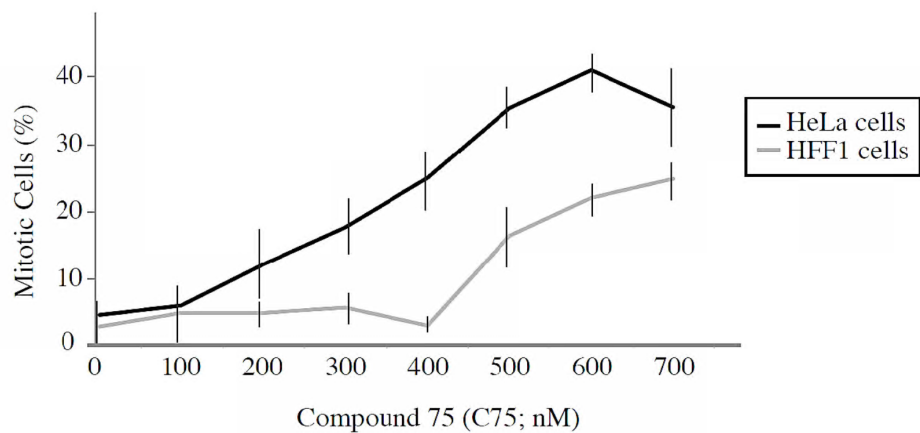
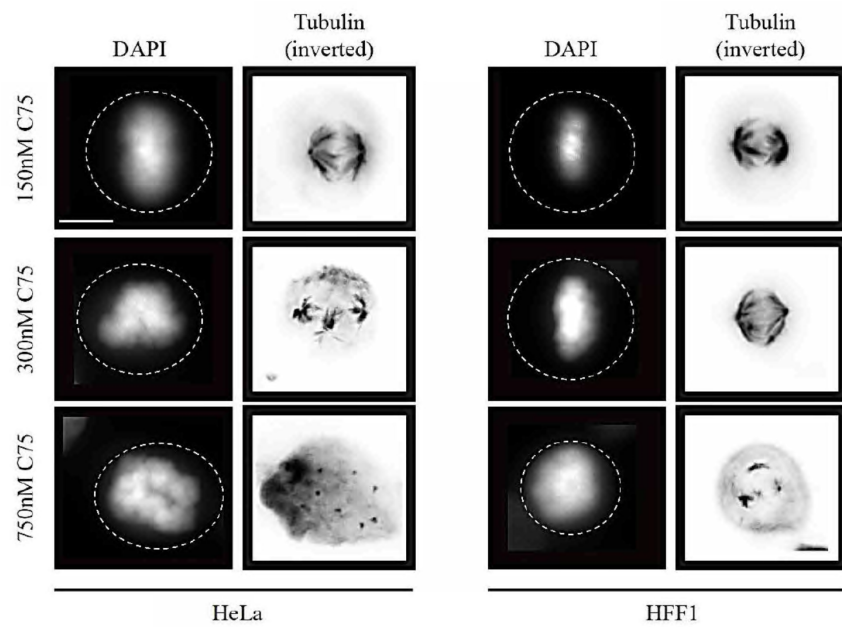
A**B****C**

Figure 11. C75 causes HeLa cells to arrest in mitosis with disorganized spindles. A)

Brightfield images show HeLa cells treated with DMSO or 500 nM C75 for 8 hours. The images show a change in the number of cells in mitosis after each treatment. **B)** A line graph shows changes in the percentage of mitotic HeLa and HFF-1 cells after treatment with increasing concentrations of C75 for 8 hours. The bars show standard deviation. **C)** Images show cells stained for DNA (DAPI) and tubulin in mitotic HeLa and HFF-1 cells after treatment with 150, 300 and 750 nM C75 for 8 hours. The scale bar is 10 μ m.

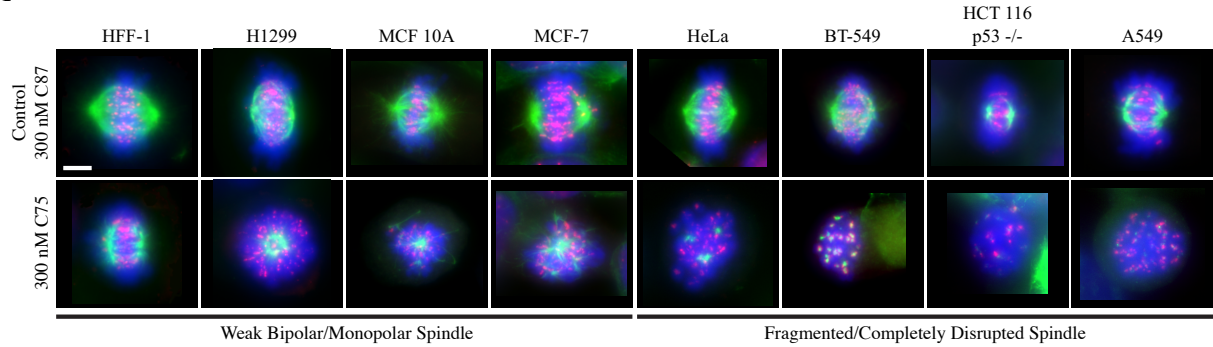
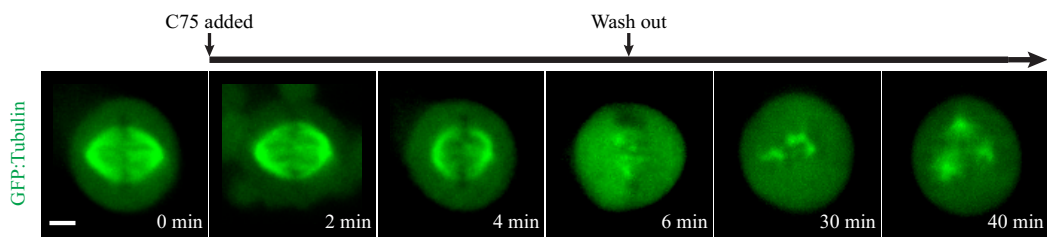
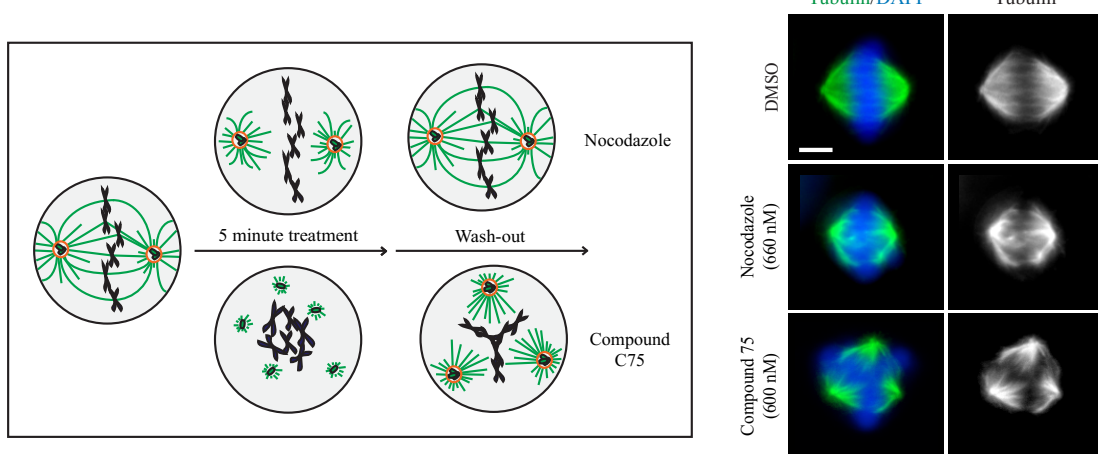
A**B****C**

Figure 12. C75 causes mitotic spindle phenotypes in a broad range of cell types and causes spindle pole fragmentation. A) Images show fixed cells with bipolar, monopolar or fragmented mitotic spindles in cancer (H1299, MCF 7; mammary gland adenocarcinoma, HeLa, BT-549; breast ductal carcinoma, HCT116 p53^{-/-}, and A549) and non-cancer (HFF-1; foreskin fibroblast and MCF 10A; mammary gland fibrocystic disease) cell lines after treatment with 300 nM of C75 for one population doubling time. Tubulin is in green, ACA (stains kinetochores) in red, and DAPI (stains chromatin) is in blue. The scale bar is 10 μm . B) Images show a HeLa cell stably expressing GFP:tubulin treated with 900 nM of C75 for 6 minutes (arrows indicate addition and washout). Times are indicated in minutes, and the scale bar is 10 μm . C) Images show fixed HeLa cells after treatment with 660 nM of nocodazole or 600 nM of C75 for 5 minutes, which was then washed out for 40 minutes. Cells were stained for tubulin (green in left panels; white on right panels) and DNA (DAPI; blue in left panels). While nocodazole-treated cells reformed bipolar spindles, C75-treated cells had multipolar spindles. The cartoon schematic on the left illustrates the experimental design and the phenotypes that were observed during and after treatment with each drug. Microtubules are in green, chromatin is in black, and the orange circles are centrosomes. The scale bar is 10 μm .

We next determined the phenotypes caused by treating cells with C75 for a short period of time. We imaged metaphase HeLa cells expressing GFP:tubulin treated with 900 nM of C75 for 5 minutes, which was then removed (**Figure 12B**). In the presence of C75, the microtubules regressed substantially, which coincided with fragmentation of the spindle poles into small foci. When C75 was washed out, the spindle poles formed a multipolar spindle (**Figure 12B**). We have more recent data showing that microtubule recovery occurs even in the presence of C75 (see Chapter 4). Since the loss of microtubules was reminiscent of drugs that prevent microtubule polymerization, such as nocodazole, we performed a similar experiment where we compared the phenotypes caused by C75 and nocodazole. For this experiment, we treated HeLa cells with either drug for 5 minutes, then removed the drug and fixed the cells after 40 minutes. While nocodazole-treated cells formed bipolar spindles after drug removal, C75-treated cells formed multipolar spindles (**Figure 12C**). Therefore, despite causing microtubule depolymerization, C75 has different effects on the spindle compared to drugs known to prevent microtubule polymerization. This prompted us to determine the mechanism of action of C75 in more detail in Chapter 4.

Chapter 4: A novel compound that disrupts mitotic spindle poles in human cells

This chapter describes the results from: Jaunky, D. B., Husser, M., Larocque, K., Liu, P., Thampipillai, S., Forgione, P., & Piekny, A. (2020). A novel compound that disrupts mitotic spindle poles in human cells. *BioRxiv*.

4.1 Preamble

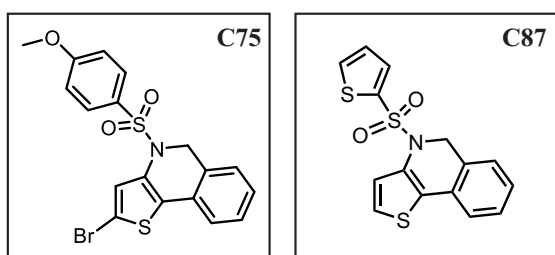
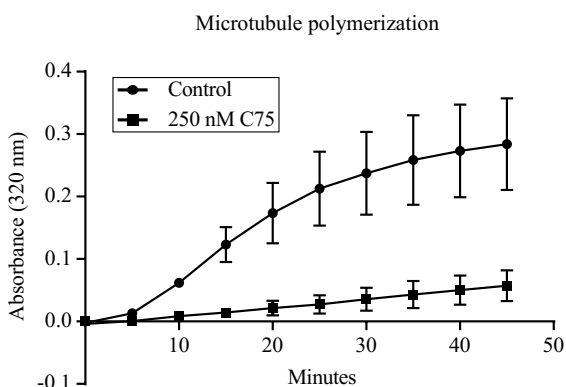
In this chapter we characterize the mechanism of action of C75 in cells. As outlined in the introduction and in Chapter 3, we synthesized a family of compounds that share a common scaffold and have several functional groups amenable to modifications. One of the active derivatives, C75, reduces cell viability and in the nanomolar range causes mitotic arrest with spindle phenotypes in several cancer cell lines. Here we show that C75 prevents microtubule polymerization, destabilizes microtubules, and can bind to the colchicine-pocket on tubulin *in vitro*. Despite these similarities between C75 and colchicine, C75 causes different spindle phenotypes in cells. While colchicine causes a decrease in microtubules and spindle pole collapse without re-growth, similar concentrations of C75 cause the rapid loss of microtubules and spindle pole fragmentation followed by microtubule re-growth to form multipolar spindles. In addition, C75 and colchicine synergize for reduced viability and spindle phenotypes. Importantly, the phenotypes caused by C75 are similar to those caused by the depletion of ch-TOG, a microtubule polymerase, and tubulin and ch-TOG are displaced and oscillate in C75-treated cells. This suggests that C75 causes microtubule depolymerization in cells either directly or indirectly via inhibiting ch-TOG. This unique effect of C75 on microtubules warrants further exploration of its anti-cancer potential.

4.2 Compound 75 causes cells to arrest in G2/M phase

We recently synthesized a new family of thienoisoquinoline compounds and identified several active derivatives that can bind to tubulin *in vitro* and cause reduced cell viability (Liu et al. 2020 – *manuscript submitted*). The structure of Compound 75 (C75) is shown in **Figure 13A**, along with an inactive derivative C87. C75 prevents microtubule polymerization *in vitro* at concentrations equal to or above 250 nM (**Figure 13B**) and disrupts previously assembled microtubule polymers (**Figure 14A**). These characteristics of C75 are similar to colchicine, which prevents polymerization *in vitro* at ranges of 1-5 μM, and depolymerizes microtubules (**Figure 14A; Fitzgerald 1976**). Indeed, C75 decreases colchicine binding (**Hastie 1991; Fitzgerald 1976**), suggesting that it could compete with colchicine for binding to this site (**Figure 14B**). However, it is possible that C75 binds to a different site on the dimer, which indirectly affects colchicine-binding. Despite their similar effects on microtubule polymers *in vitro*, the ability of a lower concentration of C75 to block polymerization supports that it interacts with the polymer through a different site, and/or has different accessibility.

Next, we determined if C75 causes mitotic arrest similar to other tubulin-targeting compounds. While the inactive derivative, C87, had little effect on the viability of HFF-1 (human foreskin fibroblast), HeLa (cervical adenocarcinoma), A549 (lung carcinoma), or HCT 116 (colorectal carcinoma) cells, C75 caused reduced viability that varied depending on the cell line (**Figure 13C**). While the IC₅₀ for the viability of HeLa, A549 and HCT 116 cells treated with C75 was 427, 377 and 431 nM, respectively, it was 789 nM for HFF-1 cells (**Figure 13C**). This suggests that cancer cells have ~2-fold higher sensitivity to C75 compared to fibroblasts. To determine if the reduced viability is caused by cell cycle arrest, we performed flow cytometry on HeLa, A549 and HCT 116 cells after treatment with increasing concentrations of C75 for 8 hours. For all three

lines, there was an increase in the proportion of cells in G2/M, and a decrease in G0/G1 (**Figures 13D and 15**). An ANOVA test followed by a post hoc Tukey's multiple comparison test revealed that there was a significant change in the proportion of HeLa and A549 cells in G2/M and G0/G1 after treatment with 400 or 500 nM of C75 (**Figure 13D**). HCT 116 cells responded at lower concentrations, with significant changes observed after treatment with 200 nM, 300, 400 and 500 nM of C75 (**Figure 13D**). While there was no change in the proportion of HeLa or A549 cells in S phase, there was a decrease in HCT 116 cells in S phase after treatment with 500 nM of C75 (**Figure 13D**). To further demonstrate that cells had mitotic phenotypes, cells were fixed and stained for DNA, microtubules and centromeres after treatment with 300 or 500 nM C75 and compared to control cells. Indeed, while metaphase HeLa, A549 and HCT 116 cells had bipolar spindles and aligned chromosomes, the spindles in treated cells had reduced microtubule intensity, misaligned chromosomes and fragmented spindle poles (**Figure 13E**). Next, we counted the number of rounded, mitotic HeLa, A549 and HCT 116 cells after treatment with varying concentrations of C75 for 24 hours (**Figure 16A**). For all cell lines, we saw a dramatic increase in the proportion of mitotic cells at 300 nM (55.7% HeLa, 76.4% A549 and 71.7% HCT 116, respectively).

A**B****C**

Cell Lines	Viability IC ₅₀ , nM	
	C75	C87
HFF-1	789	> 1000
HeLa	427	> 1000
A549	377	> 1000
HCT 116	431	> 1000

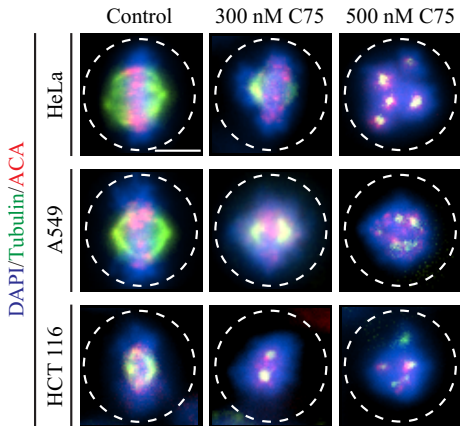
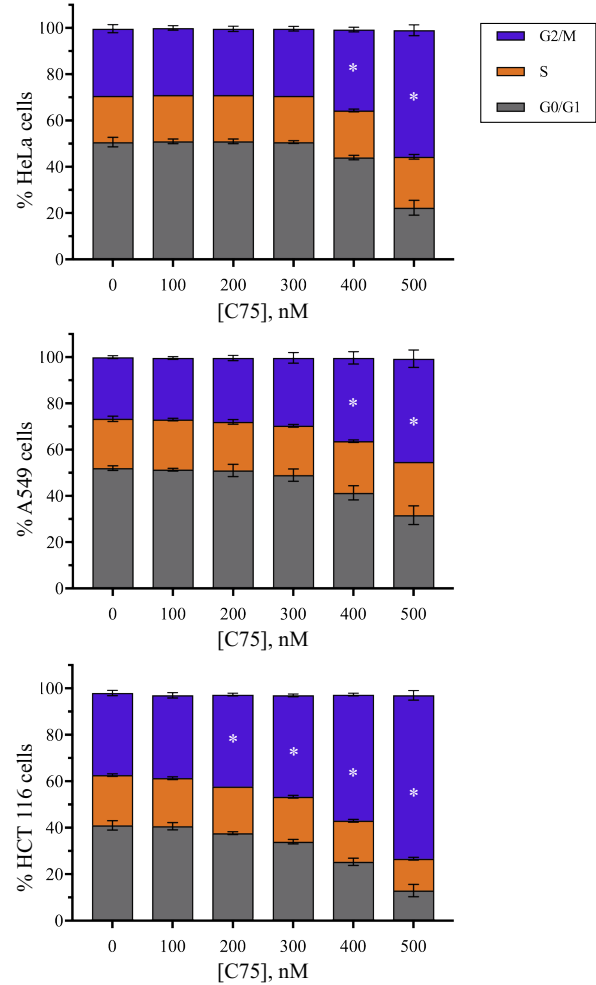
E**D**

Figure 13. C75 is a thienoisoquinoline compound that causes G2/M arrest in cultured human cells. **A)** The structures of C75 and C87, a derivative with minimal activity, are shown. **B)** A graph shows the polymerization of microtubules in vitro, measured by changes in absorbance at 320 nm (X-axis) over time (minutes; Y-axis). Tubulin was polymerized in the presence of 250 nM C75 or DMSO (control). **C)** A table shows the IC₅₀ for the viability of HFF-1, HeLa, A549 and HCT 116 over three population doubling times after treatment with C75 or C87 (N=3). **D)** Bar graphs show the distribution of cells in G0/G1, S and G2/M phases of the cell cycle measured by flow cytometry, for HeLa, A549 and HCT116 cells treated with increasing concentrations of C75 for 8 hours (n = 20,000 cells per treatment; N=3 experimental replicates). Asterisks indicate statistical significance using two-way ANOVA test and post-hoc Tukey's multiple comparison test with a 95% CI, multiplicity adjusted p < 0.0004. **E)** Images show fixed HeLa, A549 and HCT116 cells immunostained for DNA (DAPI; blue), tubulin (green), and centromeres (ACA; red) after treatment with 300 or 500 nM of C75 for 8 hours. The scale bar is 10 μm.

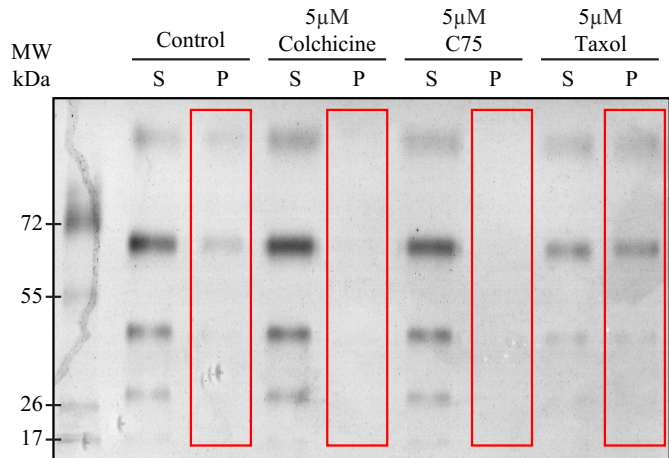
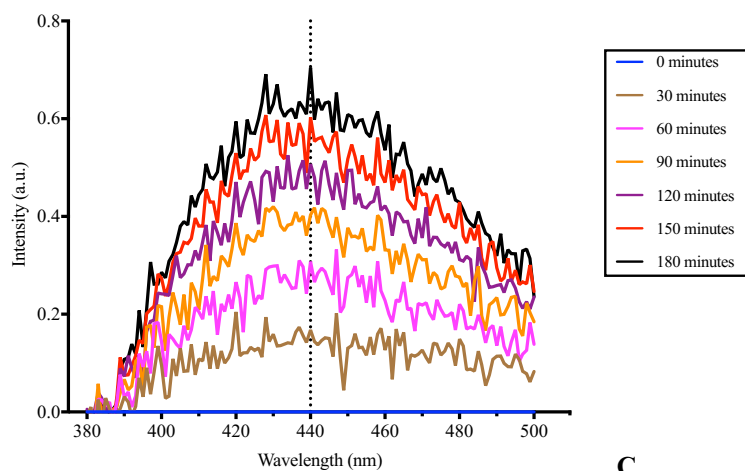
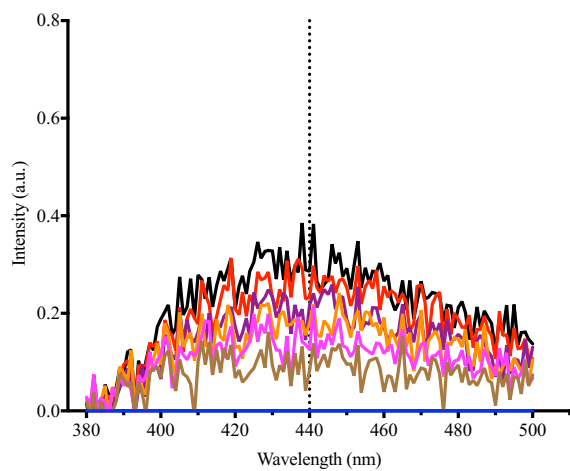
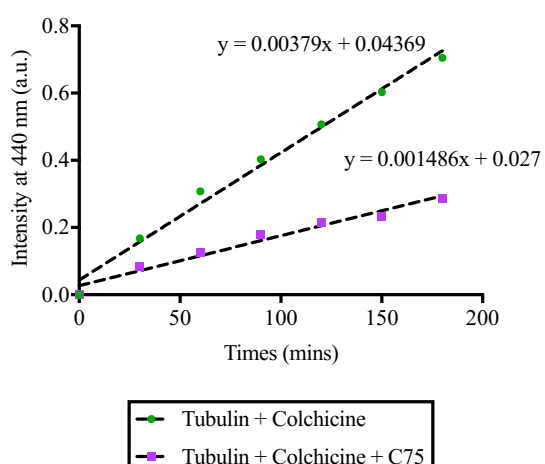
A**B****Colchicine with Tubulin****Colchicine + C75 with Tubulin****C**

Figure 14. C75 depolymerizes microtubules and competes with colchicine for tubulin-binding in vitro. **A)** A non-denaturing PAGE is shown after staining with Coomassie. The lanes show the marker (far left) and microtubules in the supernatant (S) or pellet (P) after treatment with DMSO (control), 5 μ M colchicine, 5 μ M C75 or 5 μ M paclitaxel. The red boxes highlight the pellet fractions. **B)** Line graphs from fluorescence spectroscopy show changes in the intensity (a.u., Y-axis) over the different wavelengths (nm, X-axis) for tubulin with 1 μ M colchicine (top) or 1 μ M colchicine and 500 nM C75 (bottom) over time (different colored lines as indicated in the legend). **C)** Line graphs show the changes in intensity at 440 nm for tubulin with colchicine (green) or colchicine and C75 (purple) over time (minutes, X-axis) as in B). The slopes for the best-fit lines are indicated.

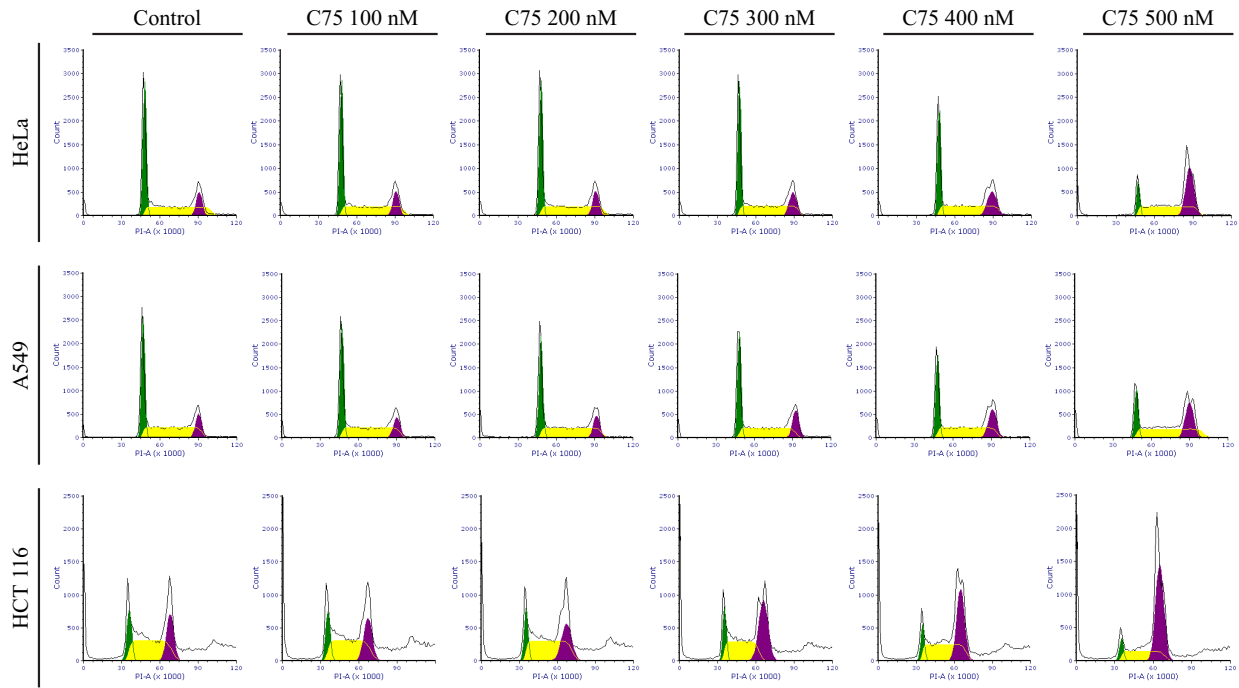


Figure 15. C75 causes cultured human cells to arrest in G2/M. Graphs show the proportion of HeLa, A549 and HCT 116 cells in the different phases of the cell cycle (G1 in green; S in yellow; G2/M in purple) 8 hours after treatment with varying concentrations of C75, as determined by flow cytometry. Cell counts are on the Y-axis and propidium iodide (PI) intensity (levels) is on the X-axis.

4.3 C75 causes spindle pole phenotypes

As described above, C75 causes spindle phenotypes that increase in severity with concentration. These phenotypes range from reduced microtubules and misaligned chromosomes to fragmented spindle poles. To further quantify the spindle phenotypes caused by C75, HFF-1, HeLa, A549 and HCT 116 cells were treated with 300 nM C75 for 4 hours and stained for DNA, γ -tubulin and centromeres (**Figure 16B**). Cells were treated at a lower vs. higher concentration of C75 and for a shorter period of time (4 hours vs. 8 or 24 hours) to capture a broader range of phenotypes. While HFF-1 cells had no obvious change in their spindle morphology, HeLa, A549 and HCT 116 cells showed spindle phenotypes that we classified as monopolar (centrosomes failed to separate), bipolar misaligned (misaligned sister chromatids) and multipolar spindles (fragmented or de-clustered centrosomes; **Figures 16B, C**). As determined by multiple t tests, there was a significant increase in HeLa cells with bipolar misaligned (41.1 vs. 7.1% control) and multipolar spindles (30.6 vs. 7.6% control), while there was a significant increase in A549 cells with monopolar (5 vs. 0% control) and multipolar spindles (77.6 vs. 3% control; **Figure 16C**). There was a significant increase in HCT 116 cells with monopolar (34.5 vs. 9.5% control), bipolar misaligned (21.5 vs. 4.4% control) and multipolar spindles (12.5 vs. 6.9% control; **Figure 16C**). To determine if multipolar spindles arose due to γ -tubulin displacement, or due to disruption of more core centrosome components, we repeated this experiment with HeLa cells and stained for DNA, tubulin and centrin-2 (**Figure 16D**). Indeed, a significantly greater proportion of C75-treated cells had more than 1 or 2 centrin-2 foci compared to control cells (59 vs. 10%). Therefore, C75 is capable of displacing centrosome components. The different proportions of spindle phenotypes caused by C75 in the different cell lines likely reflects underlying differences in their 360 genetic backgrounds and overall sensitivity to spindle disruption.

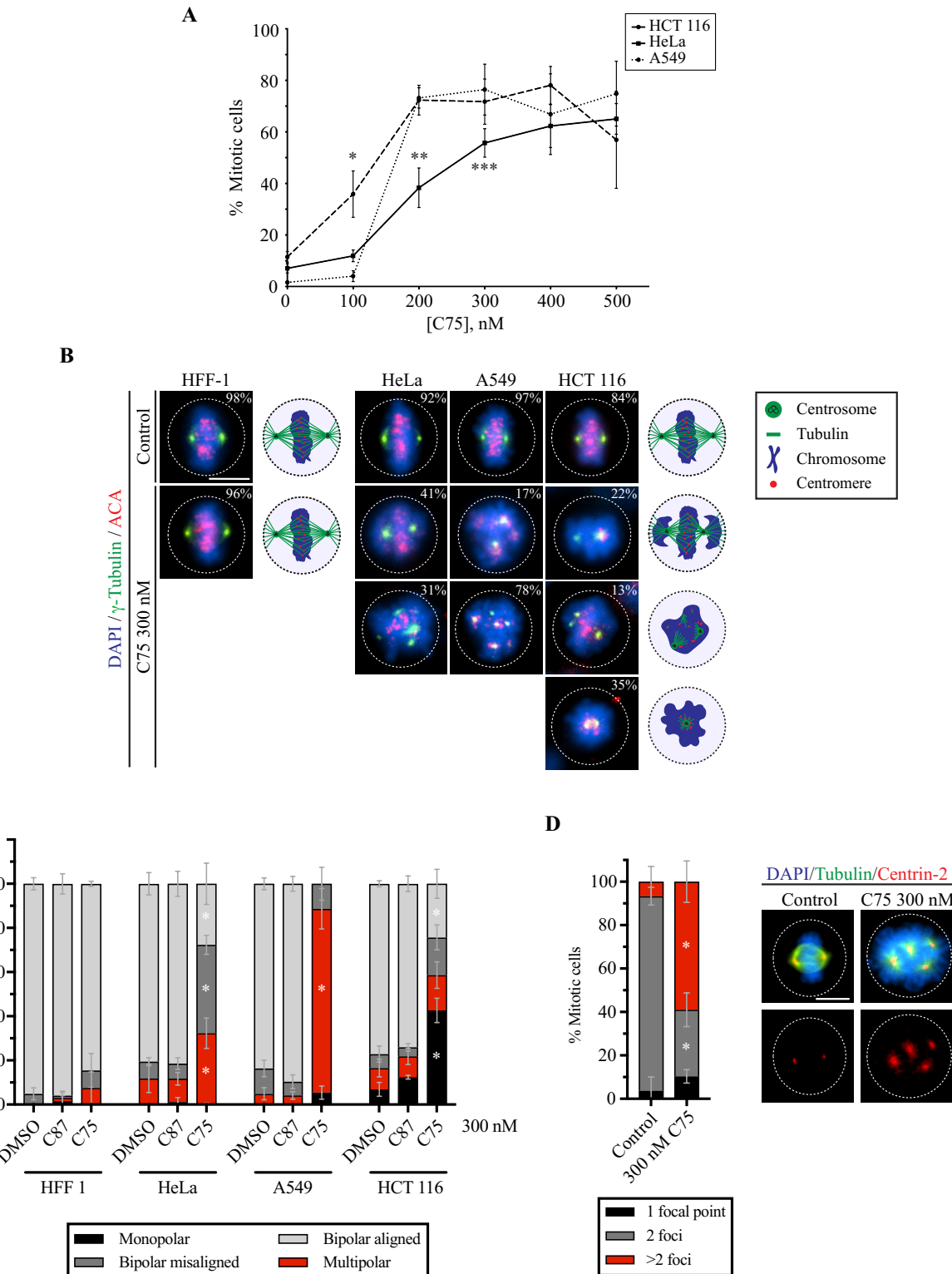


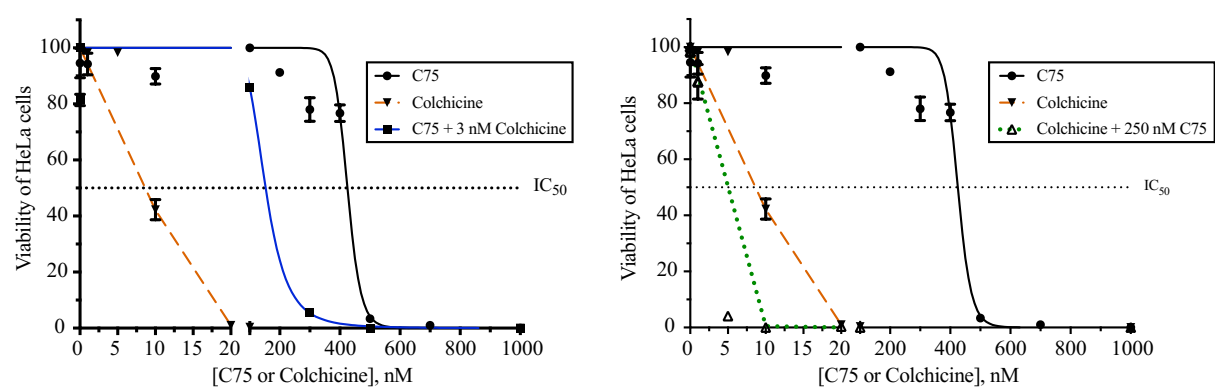
Figure 16. C75 causes cells to arrest in mitosis with multipolar spindles. **A)** A line graph shows the proportion of mitotic HeLa, A549 and HCT 116 cells after treatment with increasing concentrations of C75 for 24 hours. Asterisks indicate statistical significance using two-way ANOVA test and post-hoc Tukey's multiple comparison test with a 99% CI; a single asterisk means that HCT 116 is significantly different than HeLa and A549 (multiplicity adjusted $p = 0.0007$ and $p < 0.0001$, respectively), two indicates that HeLa is significantly different than A549 and HCT 116 (multiplicity adjusted $p < 0.0001$ for both), and three indicates that HeLa is significantly different than A549 (multiplicity adjusted $p = 0.0035$). **B)** Images show fixed HFF-1, HeLa, A549 and HCT116 cells stained for DNA (DAPI; blue), γ -tubulin (green), and centromeres (ACA; red) after treatment with 300 nM of C75 for 4 hours. Cartoon schematics (green circles, centrosomes; blue, chromatin; green lines, microtubules; red, centromeres) show bipolar spindles with aligned chromosomes (top), bipolar spindles with misaligned chromosomes (second from top), multipolar spindles (third from top), or monopolar spindles (bottom). The proportion of each phenotype is indicated at the top right corner of each image. **C)** A bar graph shows the proportion of each phenotype (bipolar aligned in light grey; bipolar misaligned in dark grey; multipolar in red; monopolar in black) for HFF-1, HeLa, A549 and HCT 116 cells treated as in B. Bars show standard deviation and asterisks indicate two-way ANOVA test and a post-hoc Tukey's multiple comparison test with a 99% CI, and multiplicity adjusted $p < 0.001$ for each phenotype vs. DMSO and C87. **D)** A bar graph shows the proportion of HeLa cells with 1 (black), 2 (dark grey) or more (red) centrin-2 foci after treatment with DMSO or 300 nM C75. Cells were fixed and stained for DNA (DAPI; blue), tubulin (green), and centrin-2 (red). Asterisks indicate statistical significance using a multiple t test with a 95% CI with a multiplicity adjusted $p = 0.0009$ and $p = 0.0031$, respectively. The scale bar for all images is 10 μm .

4.4 Combining C75 and colchicine enhance spindle phenotypes

Our data show that C75 has characteristics similar to colchicine and can bind to the colchicine-pocket on tubulin. However, C75 is more effective at preventing polymerization *in vitro* and it could bind to alternate sites on tubulin. In addition, the two compounds could have different accessibility, or other targets in cells. If C75 binds to a different site or target vs. colchicine, it could cause synergistic vs. additive effects when combined. We found that the IC₅₀ for viability of C75 and colchicine in HeLa cells was 425 nM and 9.5 nM, respectively (**Figure 17A**). Adding 3 nM of colchicine, a sub-optimal dose that caused little change in viability, to varying concentrations of C75 lowered the IC₅₀ for C75 to 153 nM (**Figure 17A**). Similarly, adding 250 nM of C75, which had a minimal impact on viability, to a range of colchicine concentrations lowered the IC₅₀ for colchicine to 1.9 nM (**Figure 17A**). To ascertain whether the combinatorial treatments were synergistic, additive or antagonistic, we analyzed the data using software for drug combination studies called CompuSyn (**Chou 2010**). Using the non-constant ratio method, we determined the Combination Index (CI) as a measure of drug interaction for each drug combination and found that C75 and colchicine synergized at concentrations where they typically had low lethality (**Figure 17B**). In particular, synergy was observed with 3 nM of colchicine and 300 nM of C75, and when 250 nM C75 was combined with 5 nM colchicine, with CI values of 0.20 and 0.25, respectively (**Figure 17B**).

Next, we determined the spindle phenotypes caused by combining the two compounds. HeLa cells were treated for 4 hours with 20 or 50 nM colchicine, or 100, 200 or 300 nM of C75 with or without 20 nM colchicine. Cells were fixed and stained for DNA, γ -tubulin and centromeres, and the proportion of cells with bipolar, bipolar misaligned or multipolar spindles was counted for each treatment (**Figure 18A, B**). While control (DMSO) and cells treated with 20

nM colchicine, or 100 nM or 200 nM C75 had similar proportions of bipolar misaligned or multipolar spindles, higher concentrations of colchicine (50 nM) or C75 (300 nM) caused an increase in the proportion of cells with these phenotypes; **Figure 18A, B**). When 20 nM of colchicine was added to C75 (100, 200 and 300 nM) the proportion of cells with bipolar misaligned and/or multipolar spindles increased (**Figure 18A, B**). In particular, combining 20 nM colchicine with 300 nM C75 caused the multipolar phenotype to increase beyond the sum of each drug on their own at those concentrations. A similar enhancement of phenotypes was observed in HCT 116 cells, when 20 nM colchicine was added with 300 or 400 nM of C75 (**Figure 18C**). Therefore, we propose that C75 and colchicine enhance each other's effect in cells, suggesting that they have different binding sites or accessibility for tubulin, or bind to a different target in cells.

A**B**

[Colchicine], nM	% Lethality
0	0%
1	2%
5	2%
10	58%
20	99%
30	99%
40	99%
50	100%
100	100%
1000	100%

[C75], nM	% Lethality
0	0%
1	6%
10	10%
100	0%
200	9%
300	22%
400	23%
500	97%
700	99%
1000	100%

[Colchicine], nM	[C75], nM	% Lethality	Combination Index (CI)	
0	0	0%	>1000	Antagonistic
3	0	19%	7.4	Antagonistic
3	100	14%	237	Antagonistic
3	300	95%	0.2	Synergistic
3	500	100%	0	-
3	1000	100%	0	-
3	10000	99%	0	-

[C75], nM	[Colchicine], nM	% Lethality	Combination Index (CI)	
0	0	0%	>1000	Antagonistic
250	0	2%	>1000	Antagonistic
250	1	12%	897	Antagonistic
250	5	96%	0.25	Synergistic
250	10	100%	0	-
250	20	100%	0.12	Synergistic
250	30	99%	0.33	Synergistic
250	40	99%	0.43	Synergistic
250	50	100%	0	-
250	100	100%	0	-
250	1000	100%	0	-

Figure 17. Combining C75 with colchicine enhances lethality and shows a synergistic interaction. **A)** Line graphs show the IC₅₀ for the viability (dotted black lines) of HeLa cells treated with varying concentrations of C75, colchicine, or both after three population doubling times as indicated. The graph on the left shows changes in viability (Y-axis) with increasing C75 concentrations (X-axis; black line), colchicine (dotted orange line), and C75 with 3 nM colchicine (blue line). The graph on the right shows the changes in viability with colchicine and 250 nM C75 (green dotted line). The bars indicate SEM, for N=3 experimental replicates. **B)** Tables illustrate the percent lethality of HeLa cells treated with colchicine (top left), C75 (top right), or both in combination (bottom two) for different concentrations as indicated. Also included are values for the Combination Index (CI) calculated using CompuSyn software, and whether the values indicate synergistic, antagonistic or additive interactions. Red boxes highlight the lowest concentrations that show synergism between C75 and colchicine.

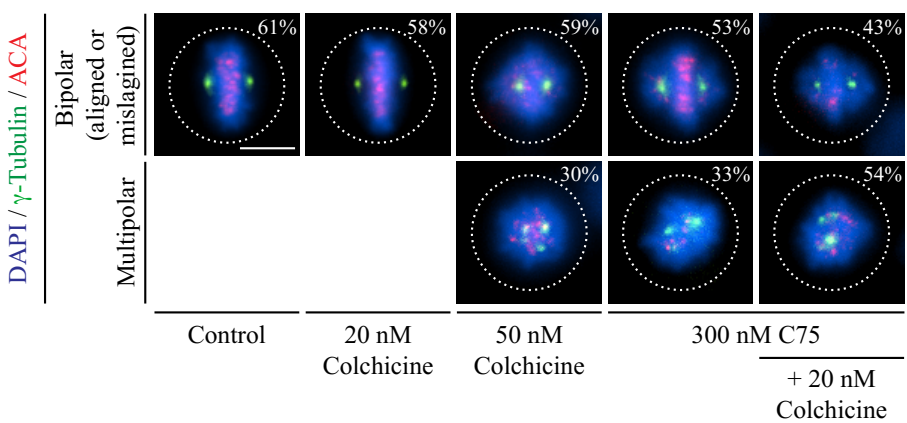
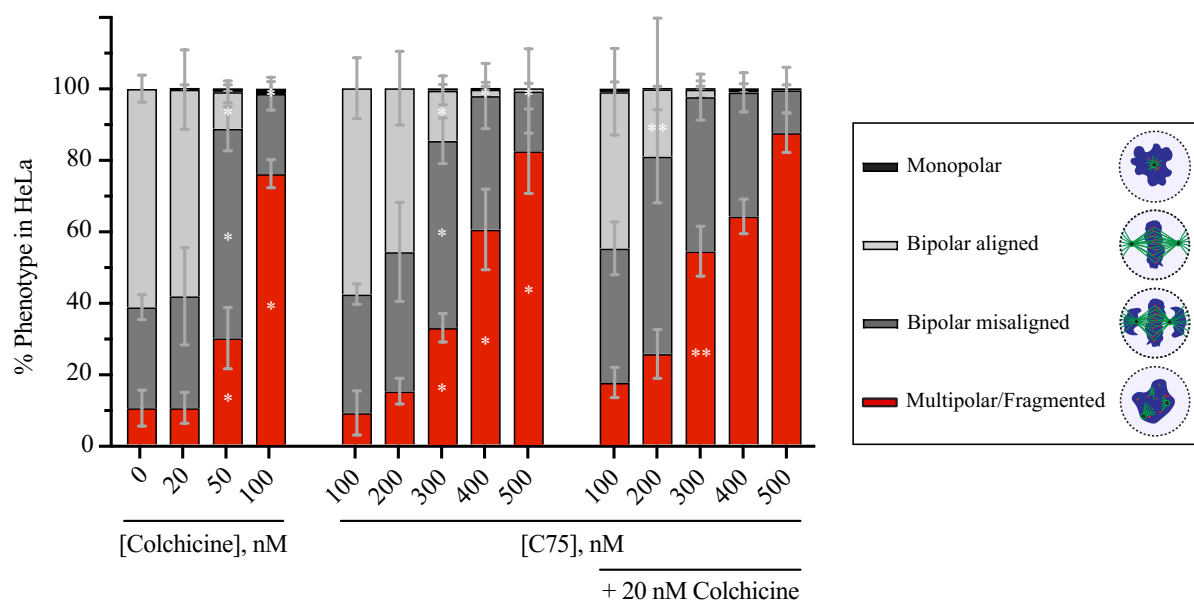
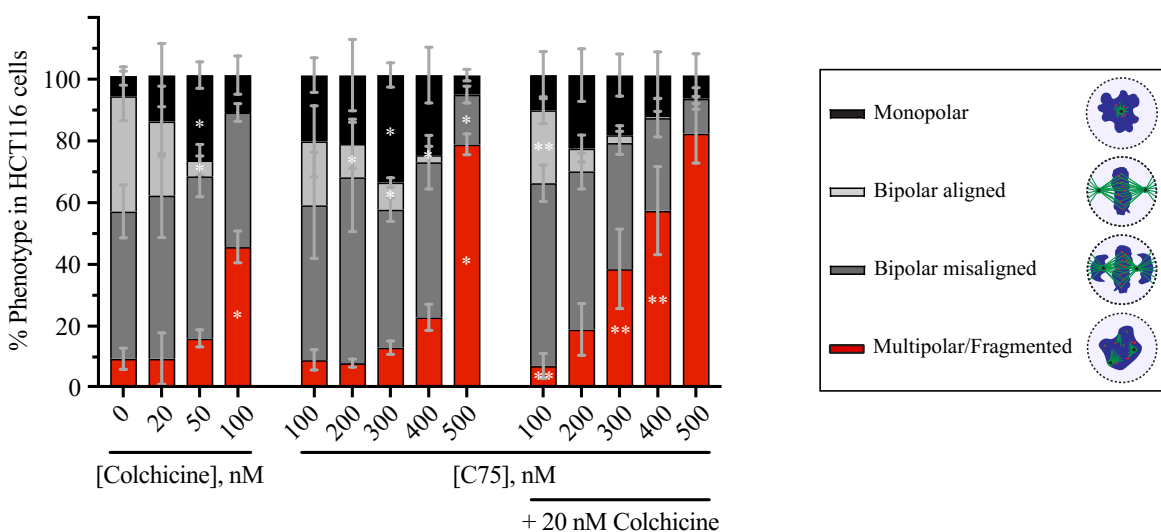
A**B****C**

Figure 18. Combining C75 with colchicine enhances spindle phenotypes in HeLa and HCT

116 cells. **A)** Images show fixed HeLa cells stained for DNA (DAPI; blue), γ -tubulin (green) and ACA (centromeres; red) after treatment for 5 hours with colchicine, C75 or both. On the images are the proportion of cells with bipolar spindles, and aligned chromosomes (control, DMSO or 20 nM colchicine), or misaligned chromosomes and multipolar spindles (50 nM colchicine, 300 nM C75 or both). The scale bar is 10 μ m. **B)** Bar graphs show the proportion of HeLa cells from A) with bipolar aligned (light grey), bipolar misaligned (dark grey), multipolar (red) or monopolar (black) spindles. Bars show standard deviation. Statistical analysis was done using two-way ANOVA test and a post-hoc Tukey's multiple comparison test with a 90% CI, and multiplicity adjusted $p = < 0.0831$; a single asterisk indicates significance to the control (DMSO) and two indicates significance to C75. **C)** A bar graph shows the proportion of HCT 116 cells with bipolar aligned (light grey), bipolar misaligned (dark grey), multipolar (red) or monopolar (black) spindles after 5 hours of treatment with varying concentrations of colchicine, C75, or both as indicated. Bars show standard deviation. A single asterisk indicates significance to the control (DMSO) and two asterisks indicates significance to the single treatment with C75. Statistical analysis was done using two-way ANOVA test and a post-hoc Tukey's multiple comparison test with a 90% CI, and multiplicity adjusted $p = < 0.0687$. The cartoon schematics to the right show examples of the different spindle phenotypes (green circles are centrosomes, green lines are microtubules, blue is chromosomes, red is centromeres).

4.5 C75 and colchicine have different effects on microtubule polymers in cells

Our data show that C75 causes mitotic spindle phenotypes, which include the formation of multipolar spindles. Although C75 acts similarly to colchicine *in vitro*, the enhancement seen with both drugs in cells suggests that there are differences in their mechanism of action. We characterized spindle phenotypes immediately after adding C75 or colchicine and compared their phenotypes. Live imaging of metaphase HeLa cells were treated with 300 nM C75 or colchicine and imaged using live dyes (Hoechst 33342 to visualize chromatin, and SiR-tubulin to visualize tubulin) to monitor spindle phenotypes. The majority of control cells (DMSO-treated) exited mitosis, with bipolar spindles that matured to segregate sister chromatids and form a midbody (14/15), with the exception of one cell that started as a tripolar cell but eventually formed a pseudo bipolar spindle and divided successfully (**Figure 19A**). All cells treated with 300 nM colchicine remained bipolar, but while some cells arrested with collapsed spindles (5/20), the majority of cells exited mitosis similar to control (15/20; **Figure 19A**). Cells treated with 300 nM C75 either arrested in mitosis with bipolar spindles (12/20), or became multipolar (7/20), and a monopolar spindle formed in one cell (1/20; **Figure 19A**). In cells treated with either colchicine or C75, the microtubules decreased or were lost altogether, but in C75-treated cells, microtubules re-polymerized with an uneven distribution between the two poles (**Figure 19A**).

Next, we compared how cells recovered from short treatments of C75 or colchicine. HeLa cells were treated with 500 nM of C75 or colchicine for 5 minutes, then the drugs were washed out, and cells were left to recover in drug-free media for 40 minutes prior to fixing and staining for DNA and tubulin (**Figure 19B**). While the majority of cells recovered with bipolar spindles after colchicine treatment (79.2% bipolar vs. 17.7% multipolar), a significantly larger proportion of cells treated with C75 had multipolar spindles determined by the multiple t test (45.7% bipolar

vs. 49.7% multipolar; **Figure 19B**). The data show C75 causing different spindle phenotypes compared to colchicine in cells, although both compounds can prevent microtubule polymerization and cause depolymerization *in vitro*.

To further compare the effect of C75 and colchicine on microtubules in cells, we induced microtubule depolymerization by cold treatment, then monitored its re-growth in the presence of the compounds. To do this we used HeLa cells stably expressing GFP-tagged tubulin, and cold-treated the cells for 30 minutes in an ice bath. The cells were then upshifted to 37°C at which time 300 nM C75 or colchicine was added, then the cells were imaged during recovery as represented by the cartoon (**Figure 20A**). All of the control cells re-formed robust bipolar spindles and were in telophase ~40 minutes after temperature upshift, indicating the recovery of microtubules and reformation of a functional mitotic spindle. In the presence of colchicine, microtubules steadily decreased in intensity, with no detectable GFP signal by 98 minutes (24/24 cells; **Figure 20A**). In C75-treated cells, microtubules similarly decreased, but after 20 minutes, they re-polymerized to form spindles and a GFP signal was detected in all cells by 98 minutes (15/15 cells; **Figure 20A**). Although the cells re-formed spindles, sister chromatids were not aligned, and the cells failed to exit mitosis (**Figure 20A**). To further characterize these phenotypes, we quantified changes in spindle pole volume and maximum intensity of the spindle pole over time (**Figure 20A-D; 21A, B**). As expected, colchicine-treatment caused a decrease in both volume and maximum intensity of the spindle poles over time (**Figure 20A-D; 21A, B**). Some fluctuation in volume was observed, however, there was a net, linear decrease in volume and signal intensity over time as indicated by the best-line fits with negative slopes (**Figure 20A-D; 21A, B**).

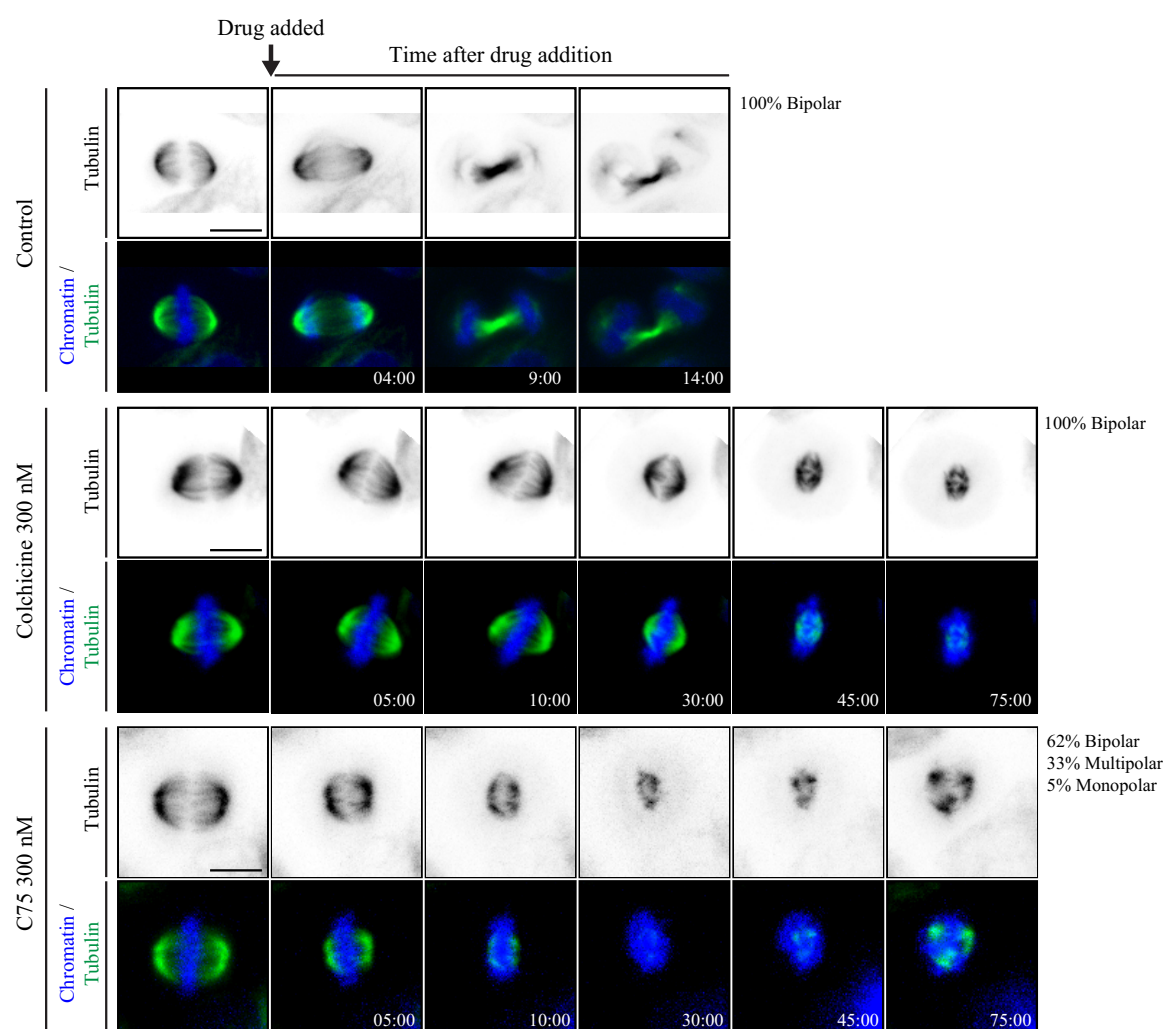
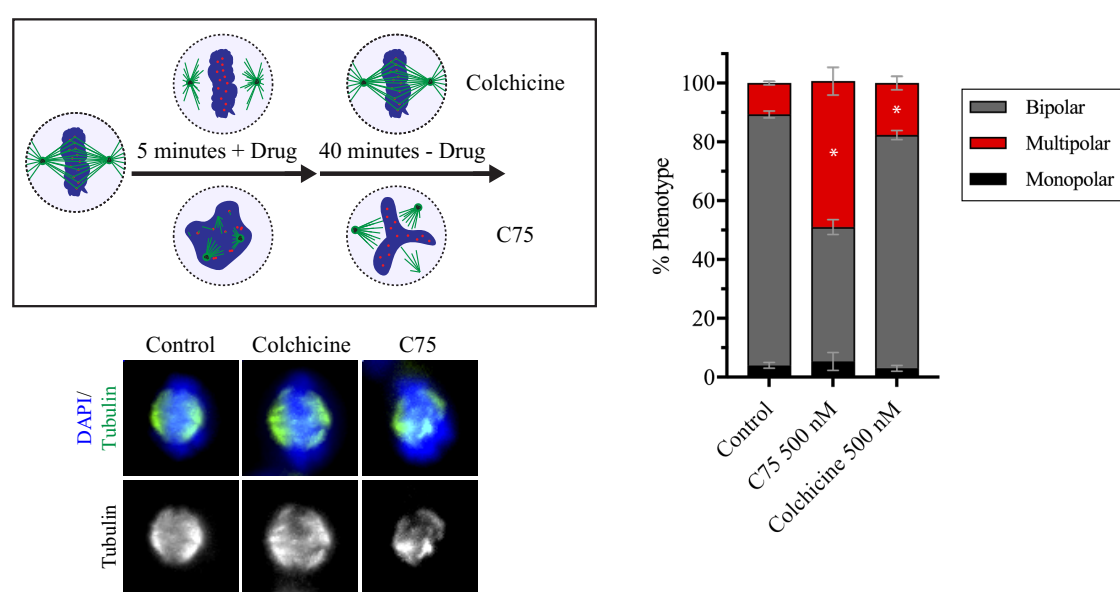
A**B**

Figure 19. C75 and colchicine cause different spindle phenotypes. **A)** Timelapse images show live HeLa cells co-stained for DNA (Hoechst 33342; blue) and microtubules (SiR-tubulin; green). Times are indicated in minutes. An arrow points to the time of addition of 300 nM of C75 (n=21), 300 nM of colchicine (n=18) or DMSO (control; n=17). The proportion of cells with bipolar, multipolar or monopolar spindles are indicated. **B)** A cartoon schematic shows how HeLa cells were treated with drug (DMSO, 500 nM C75 or colchicine) for 5 minutes, then fixed 40 minutes after the drugs were washed out. Underneath, images show fixed HeLa cells co-stained for DNA (DAPI; blue) and tubulin (green or white) after treatment with C75 or colchicine. To the right, a bar graph shows the proportion of cells with monopolar (black), bipolar (dark grey) or multipolar (red) spindles. Bars show standard deviation and asterisks indicate $p<0.05$ by multiple t tests vs. control. The scale bar for all cells is 10 μm .

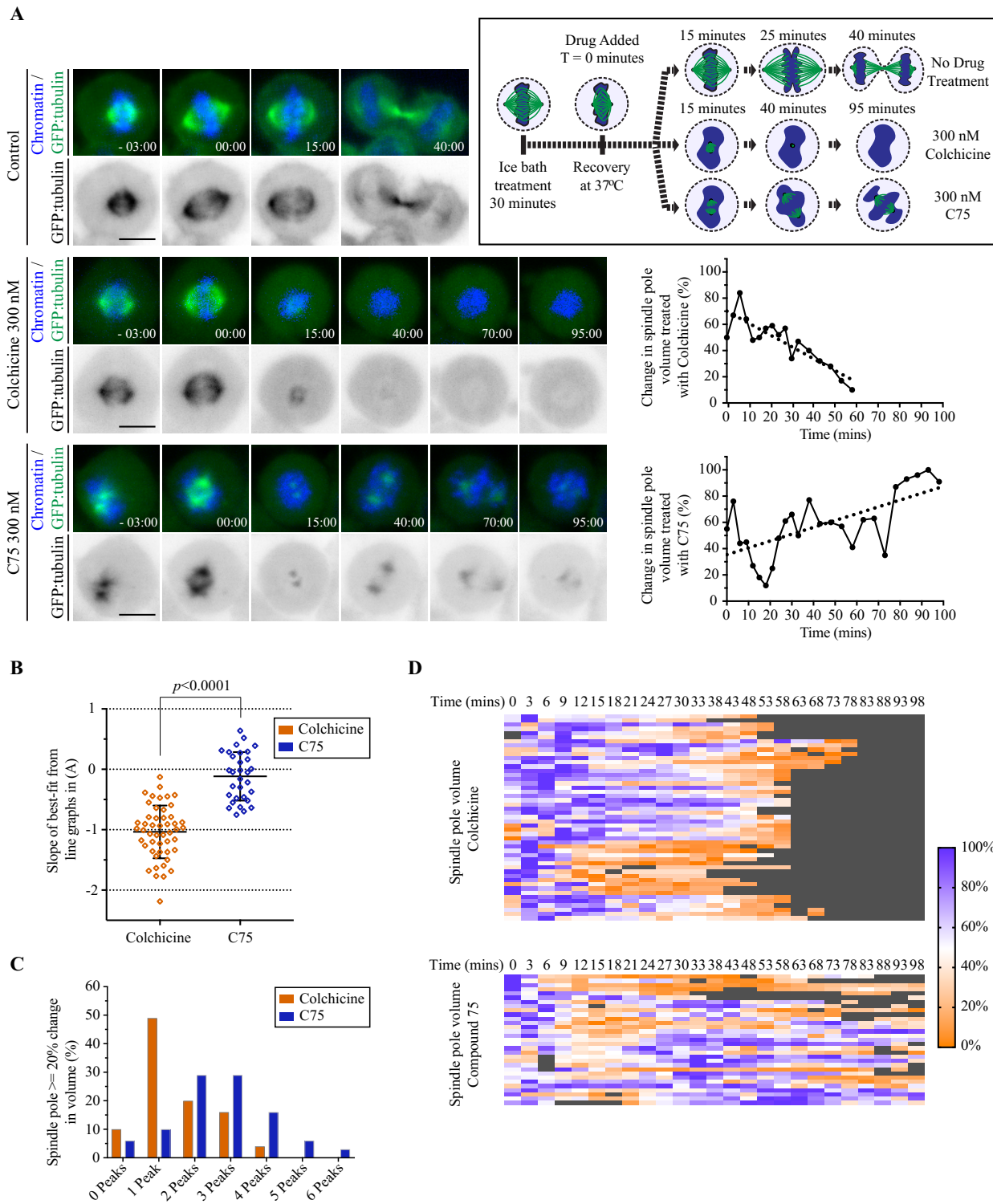


Figure 20. Microtubules and spindle poles recover in the presence of C75. **A)** A cartoon schematic (box at upper right) shows the experimental design. HeLa cells were cold-treated for 30 minutes in an ice bath to collapse microtubules, then upshifted to 37°C and imaged for microtubule regrowth in the presence or absence of 300 nM C75 or colchicine. Timelapse images show live HeLa cells stably expressing GFP:tubulin (green) and co-stained for DNA by Hoechst (blue), with the times indicated in minutes. DMSO (control, n=6), colchicine (n=24) or C75 (n=15) was added at 0 minutes. To the right, line graphs show changes in spindle pole volume (%; Y-axis) over time (X-axis) after addition of colchicine or C75 (dotted line indicates best-fit). **B)** A scatter plot shows the distribution of slope values obtained from best-fit line graphs (Y-axis) for the changes in each spindle pole volume over time after treatment with C75 or colchicine as in A). Significance was determined using the two-tailed Welch's t test, $p<0.0001$. **C)** A bar graph shows the number of peaks (X-axis) with an amplitude equal to or greater than 20% of the maximum volume of the spindle pole after treatment with C75 or colchicine (Y-axis). **D)** Heat maps show the change in volume (%) of individual spindle poles over time (at the top in minutes) in cells treated with colchicine or C75 as in A). Purple indicates larger volumes while orange indicates smaller volumes. Each line indicates a different spindle pole.

Heatmaps show the proportional changes in spindle volume or intensity for each spindle pole, and highlight how each pole decreased over time, albeit some sooner than others (**Figure 20D; 21B**). Unlike colchicine, C75-treatment caused an initial decrease in spindle pole volume and maximum intensity, followed by subsequent recovery and oscillation (**Figure 20A-D; 21A, B**). This is clearly evident in the heatmaps for each spindle pole, where signal intensity and pole volume continued to recover and fluctuate over time (**Figure 20D; 21B**). To better understand this oscillatory pattern in spindle pole volume, we quantified the number of peaks where there was a >20% change in volume. While the majority of spindle poles in colchicine-treated cells had only 1 or 2 peaks (31% cells had >2), the majority of poles in C75-treated cells had >2 peaks (54%). Thus, C75 causes distinct phenotypes compared to colchicine, where microtubule growth can recover in the presence of the compound, but this growth is not even between the spindle poles and leads to the formation of disorganized mitotic spindles.

Depleting ch-TOG, a microtubule polymerase, caused phenotypes similar to C75 (**Figure 22A; Barr and Bakal 2015**). HeLa cells treated with ch-TOG siRNAs had an increase in the proportion of bipolar spindles with misaligned chromosomes (51 vs. 17% for control) and multipolar or fragmented spindles (42 vs. 8% for control; **Figure 22A, B**). As described earlier, we saw an increase in both phenotypes in cells treated with a mild increase in C75, from 200 to 300 nM C75 for 4 hours (64 and 22% bipolar misaligned; 24 and 76% multipolar, respectively; **Figure 22A, B**). However, a similar mild increase in colchicine did not significantly change the proportion of spindle phenotypes (**Figure 22A, B**). Since ch-TOG balances the activity of MCAK, a microtubule depolymerase to control microtubule length (**Holmfeldt et al. 2004; Barr and Gergely 2008; Barr and Bakal 2015**), we propose that C75 similarly causes excess microtubule depolymerization.

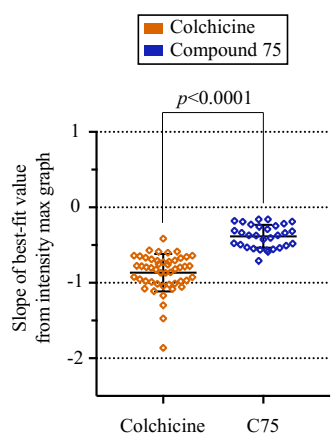
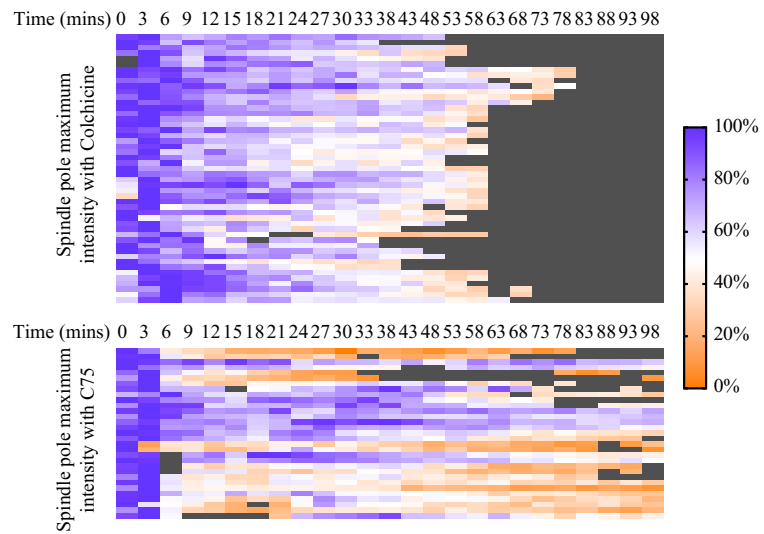
A**B**

Figure 21. Spindle poles recover in the presence of C75. **A)** A scatter plot shows the distribution of best-fit slope values obtained from plotting changes in the maximum intensity of tubulin at spindle poles over time after treatment with 300 nM colchicine or C75. Statistics were done using two-tailed Welch's t test with a $p<0.0001$. **B)** Heat maps show the change in maximum intensity of tubulin at each spindle pole (%) over time (in minutes) after treatment with 300 nM colchicine (top) or C75 (bottom). Purple indicates large values, while orange indicates small values.

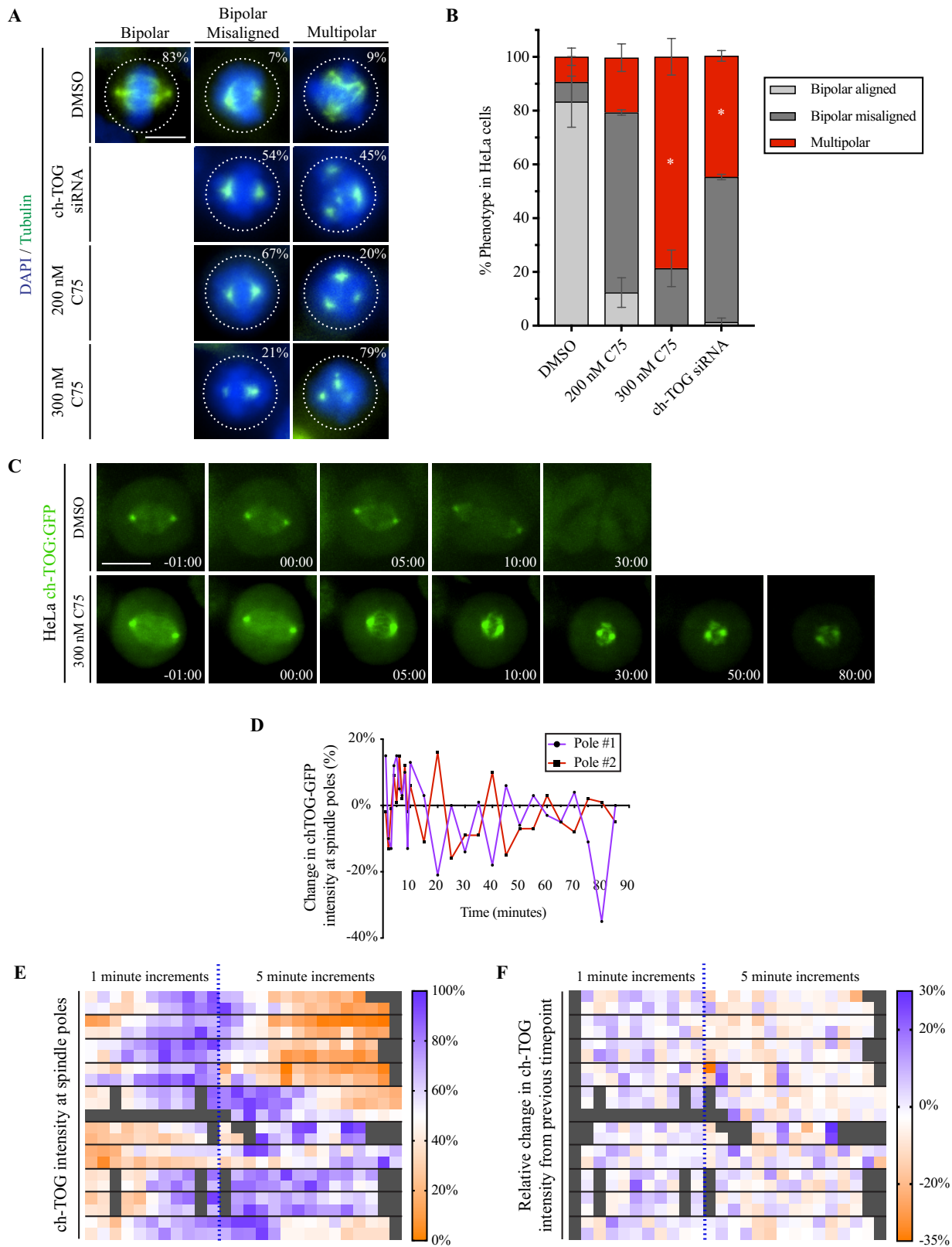


Figure 22. ch-TOG knockdown phenocopies C75, and ch-TOG oscillates in C75-treated cells.

A) Images show fixed HeLa cells stained for DNA (DAPI, blue) and microtubules (tubulin, green) after treatment with ch-TOG siRNAs, C75 or colchicine as indicated for 4 hours. The proportion of cells with bipolar spindles and aligned chromosomes, bipolar spindles with misaligned chromosomes, or multipolar spindles is indicated on the images. The scale bar is 10 μ m. **B)** A bar graph shows the proportion of cells (%) with bipolar spindles (black), bipolar spindles with misaligned chromosomes (dark grey) or multipolar spindles (red) as in A. Bars show standard deviation. Asterisks show $p<0.0001$ with respect to control (DMSO) using two-way ANOVA with a 99% confidence interval. **C)** Timelapse images show live HeLa cells expressing ch-TOG:GFP (green) in the presence ($n=10$) or absence of C75 ($n=13$). Times are indicated in minutes. The scale bar for all cells is 10 μ m. **D)** A line graph shows the change in ch-TOG:GFP signal intensity (%), Y-axis) over time (minutes, X-axis) for each pole in an individual cell after C75 treatment as in C). **E)** A heat map show the change in intensity of ch-TOG:GFP (%) at the spindle poles. Times are indicated above, with timepoints from 1-11 in increments of 1 minute, and the remainder in increments of 5 minutes (separated by the blue dotted line). **F)** A heat map shows the relative change in intensity between two adjacent timepoints (%) after C75-treatment. Times are indicated above, with the same scale as in E). For both heat maps, purple indicates larger values, while orange indicates smaller values. The poles from the same cell are plotted together and separated by cells via lines.

Next, we determined how C75 affects ch-TOG localization. Metaphase HeLa cells co-expressing sh ch-TOG for endogenous knockdown and sh-resistant ch-TOG:GFP were imaged immediately after treatment with 300 nM C75. In control cells, ch-TOG localized to the spindle poles and spindle microtubules, where the ch-TOG:GFP signal gradually decreased as cells progressed through mitotic exit (*e.g.* 30 minutes; **Figure 22C**). In cells treated with 300 nM C75, ch-TOG increased in intensity at the spindle poles, which moved closer together after ~5 minutes, and remained visible for more than 50 minutes (**Figure 22C**). We also noticed that new ch-TOG appeared at a third pole in one of the cells, albeit with lower intensity compared to one/both of the other poles (*e.g.* Fig. 6E). Measurements of the relative changes in maximum intensity of ch-TOG at the spindle poles revealed that there was a change in the intensity at one pole relative to the other in a single C75-treated cell, and the changes appeared to oscillate over time (**Figure 22D**). We then measured the maximum intensity for multiple C75-treated cells and plotted these values as heatmaps of their maximum values (%), where purple shows values closest to the maximum, and orange shows the lowest (**Figure 22E**). While there was a trend for ch-TOG levels to recover to maximum levels within the first 10 minutes of imaging, we observed reciprocal changes in intensity between the poles as in Figure 22D. To show this more clearly, we made a heat map of the relative changes in intensity from one timepoint to the next, where the colour reflects the percentage increase (purple) or decrease (orange; **Figure 22E**). Indeed, for most time points, there were inverse changes in the intensity of ch-TOG at the spindle poles within each cell, which started almost immediately after the addition of C75. This suggests that although ch-TOG accumulates at spindle poles, some pools of ch-TOG can be displaced and oscillate between the poles, supporting their instability.

Chapter 5: Characterizing the *in vivo* potential of C75

5.1 Identifying TNBCs as a target cancer for C75

Our drug discovery pipeline revealed a compound, C75, that causes mitotic arrest with high efficacy for different cancer cells (Chapter 3). We found that C75 targets tubulin and characterized its mechanism of action in cells in Chapter 4, where I found that C75 has a different effect on microtubules and spindle poles compared to other microtubule-targeting drugs. While we are constantly developing new derivatives to identify new leads with higher efficacy and/or selectivity compared to C75, it is also important to explore the potential application of our compounds.

We found that C75 caused more severe mitotic spindle phenotypes in cells derived from progressive cancers. In particular, it had a strong effect on the TNBC cell line, BT549, which prompted us to explore the effect of C75 on other TNBC cell types. MDA-MB-231 and Hs 578t cells have different genetic backgrounds but lack and/or have low expression of estrogen receptors (ER), progesterone receptors (PR) and human epidermal growth factor receptor-2 (HER2) categorizing them as TNBCs. We found that the IC₅₀ for MDA-MB-231, BT-549 and Hs578t cells was 263, 186 and 258 nM, respectively (**Figure 23A, B**). This is ~1.5-2-fold lower compared to MCF10A cells, (363 nM) which are derived from fibrocystic diseased tissue of the mammary gland (**Figure 23A, B**). Although MCF10A cells are not derived from a cancer, they have higher aneuploidy and a higher proportion of multipolar spindles compared to other cell lines, which could increase their sensitivity to C75 (**Figure 23A**). This efficacy is in stark contrast to the IC₅₀ for C75 in HFF-1 cells and a patient-derived fibroblast line, which had an IC₅₀ of 819 nM and 1160 nM, respectively (**Figure 23A, B**). Although preliminary and despite the relatively low selectivity compared to MCF10A, TNBCs could be an ideal group of cancers to consider targeting with C75.

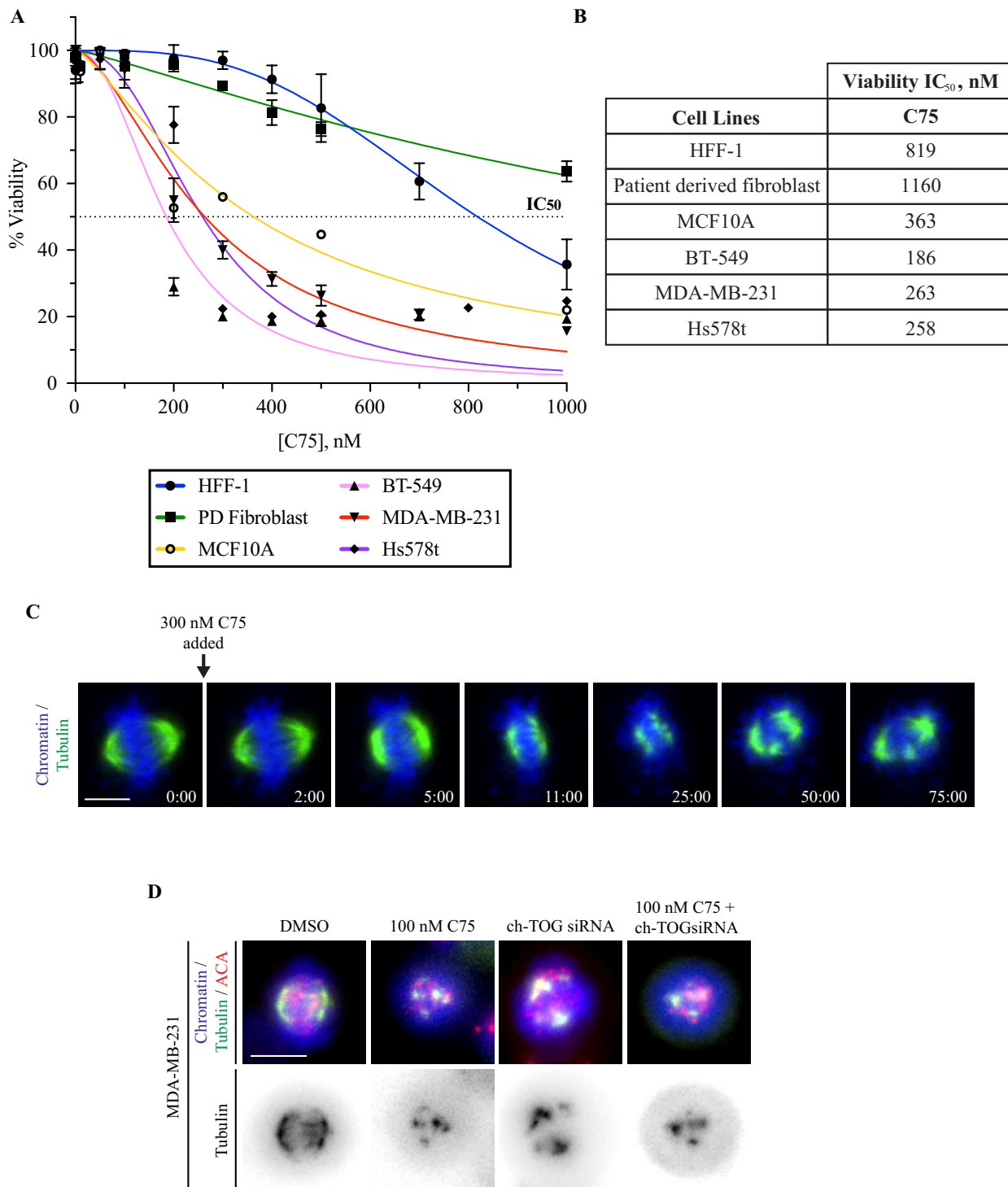


Figure 23. C75 has high efficacy for TNBCs and causes multipolar spindles to form in MDA-MB-231 cells. **A)** A line graph shows the IC₅₀ values for various cell lines treated with increasing concentrations of C75. **B)** HFF-1, patient derived fibroblast (PDF) and MCF10A are all non-cancerous cell lines but MCF10A is derived from fibrocystic diseased tissue, while BT-549 and MDA-MB-231 are both TNBC cell types. Cells from each line were treated for 3 population doubling times (PDT). **C)** Images show a mitotic MDA-MB-231 cell co-stained for microtubules with SiR-tubulin (green) and chromatin with Hoechst 33342 (blue) after treatment with 300 nM C75. Times in minutes are indicated. The scale bar is 10 μm. **D)** Images show fixed MDA-MB-231 cells co-stained with DAPI to visualize chromatin (blue), microtubules (tubulin; green) and centromeres (ACA; red) after ch-TOG RNAi, or treatment with 100 nM C75. The scale bar is 10 μm.

We then determined the phenotypes caused by C75 in MDA-MB-231 cells. To do this, we imaged metaphase MDA-MB-231 cells stained with SiR-tubulin to visualize microtubules and Hoechst 33342 to visualize chromatin, after treatment with 300 nM of C75 (**Figure 23C**). It is important to note that SiR-tubulin is a fluorophore attached to docetaxel, which theoretically could confer a change in microtubule dynamics. While we previously compared SiR-tubulin imaging data with GFP:Tubulin in HeLa cells to ensure that we had the same outcome when assessing spindle phenotypes caused by C75, this has not yet been done in MDA-MB-231 cells. Similar to what we had observed for HeLa cells (Chapter 4), we saw a reduction in microtubules, followed by the fragmentation of spindle poles and the re-growth of microtubules to form disorganized/multipolar spindles. Although the data is preliminary, given our extensive analysis of spindle phenotypes caused by C75 in HeLa cells, we propose that it has a similar mechanism of action in MDA-MB-231 cells. This experiment will be repeated to obtain a higher number of biological replicates, which will be analyzed similarly to HeLa cells for spindle pole dynamics.

As described in Chapter 4, we found that C75 causes spindle phenotypes similar to the depletion of ch-TOG. As a reminder, ch-TOG is a microtubule polymerase required for microtubule polymerization during metaphase and balances the activity of MCAK, a microtubule depolymerase (**Gergely et al. 2003; Zhang et al. 2008; Brouhard et al. 2008; Barr and Gergely 2008; Barr and Bakal 2015; Gutierrez-Caballero et al. 2015**

Ch-TOG RNAi causes a decrease in microtubules in cells and spindle pole fragmentation, presumably due to the unchecked activity of MCAK (**Gergely et al. 2003; Brouhard et al. 2008; Barr and Gergely 2008; Barr and Bakal 2015**). While it is not clear why the loss of ch-TOG causes spindle poles to fragment, ch-TOG is loaded onto the spindle poles and the loss of microtubules there could lead to instability of the centrosome and/or PCM (**Gergely et al. 2003; Brouhard et al. 2008; Barr and Gergely 2008;**

Barr and Bakal 2015). We compared the spindle phenotypes caused by ch-TOG RNAi and C75 treatment in MDA-MB-231 cells to determine if they are similar to what we had observed in HeLa cells (**Figure 23D**). The treatment of MDA-MB-231 cells with 100 nM of C75 for 4 hours caused a small proportion of cells to have multipolar/fragmented spindles (**Figure 23D**). As with HeLa cells, ch-TOG RNAi caused multipolar/fragmented spindles, which did not change when both were combined. While the data is preliminary, and we have not yet determined what happens to the proportion of multipolar cells when combined, it appears as though C75 phenocopies ch-TOG depletion in MDA-MB-231 cells.

We also characterized the mitotic spindle phenotypes caused by treating Hs578t cells with C75. Hs578t cells were treated for 8 hours with increasing concentrations of C75. We observed four categories of phenotypes, similar to what we had observed for the other cancer cell types (monopolar spindles, bipolar spindles with aligned chromosomes, bipolar spindles with misaligned chromosomes and multipolar spindles; *e.g.* **Figure 20**). Quantification of these phenotypes revealed that there is an increase in cells with bipolar misaligned and/or multipolar spindles with increasing concentrations of C75 (**Figure 24A, B**). In control cells, 78.4% had bipolar spindles with aligned chromosomes, 5.4% had bipolar misaligned spindles, 2.7% had multipolar spindles, and 13.5% had monopolar spindles (**Figure 24A, B**). As cells transition from prometaphase to metaphase, the centrosomes separate and having a proportion of cells with centrosomes that have not yet separated is considered a normal part of cell cycle progression. Treatment with 50 nM C75 had little effect on the proportion of phenotypes, while 100 nM C75 caused a decrease in the proportion of cells with bipolar spindles (60.3%), and an increase in the proportion of cells with bipolar misaligned spindles (12.3%) and multipolar spindles (16.4%) (**Figure 24A, B**). This trend continued as cells treated with 200 nM and higher concentrations of C75 had a dramatic decrease

in the proportion of cells with bipolar aligned spindles and corresponding increase in cells with bipolar misaligned and/or multipolar spindles (**Figure 24A, B**). While these experiments need to be repeated for statistical analysis, they support that C75-treatment causes spindle phenotypes in several different TNBC cell types similar to those observed in other cancer cell lines. The small increase in cells with phenotypes at the lower concentrations, could explain why TNBC cells have lower IC₅₀ values, although a similar analysis would need to be done for the other TNBC cell types to confirm this. For example, there could be an increase in mitotic catastrophe or arrest caused by the disorganized/multipolar spindles.

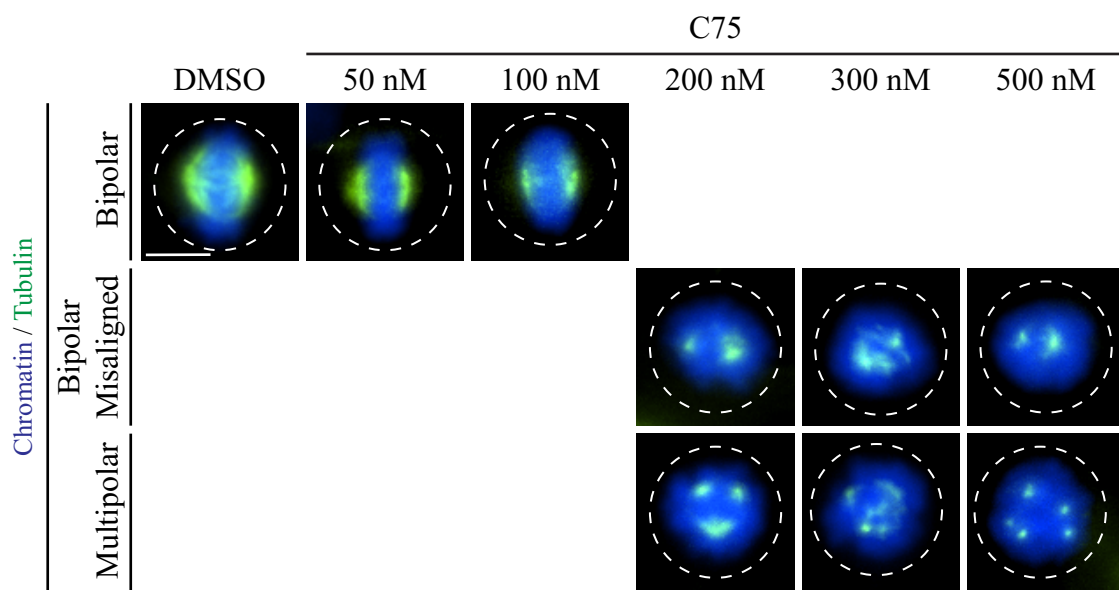
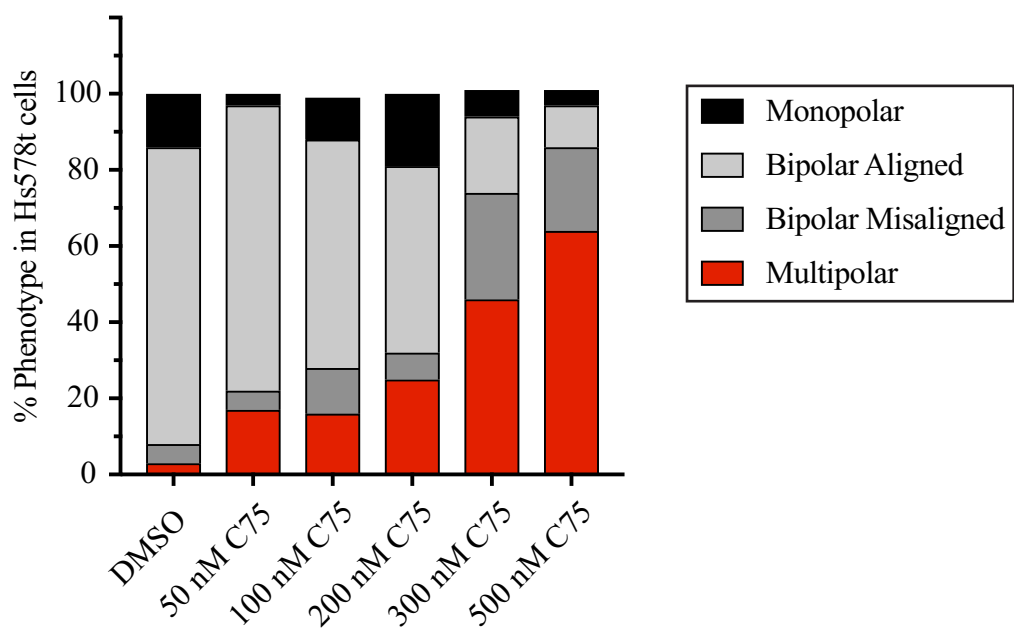
A**B**

Figure 24. C75 causes mitotic phenotypes in Hs578t cells. **A)** Images show fixed Hs578t cells co-stained for DAPI to visualize chromatin (blue) and tubulin (green) after treatment with varying concentrations of C75. Examples of cells with bipolar spindles, bipolar misaligned or multipolar spindles are shown. The scale bar is 10 μ m. **B)** A bar graph shows the proportion of spindle phenotypes caused by treatment with DMSO (control) or increasing concentrations of C75, for 8 hours. The spindle phenotypes that were analyzed are indicated; monopolar (black), bipolar aligned (light grey), bipolar misaligned (dark grey), and multipolar (red).

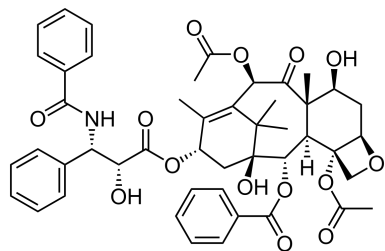
5.2 Efficacy of C75 in Taxol-resistant TNBCs

As described in Chapter 1, Taxol is used to treat TNBCs, as they lack the receptors required for targeted therapies that have been developed for other types of breast cancers. Patients with TNBC can have poor prognosis, especially if they develop resistance to Taxol as there are few alternative treatments. Since we identified TNBCs as a potentially ideal group of cancers to target with our new compounds, we wanted to determine if C75 (or a new lead) can synergize with paclitaxel (Taxol), as this would reduce the amount required for treatment, which could lower the risk of developing resistance. We also wanted to determine if C75 retains efficacy in cells that have gained resistance. Both types of data could support the use of C75 (or a new lead) in combination therapies, or as an alternative therapy when Taxol fails.

We determined how adding sub-threshold amounts of C75 affects the IC₅₀ caused by paclitaxel (**Figure 25A**) in A549, HeLa, HCT 116, and MDA-MB-231 cells (**Figure 25B**). While we have not yet analyzed the data for MDA-MB-231 cells, we observed a decrease in the IC₅₀ for paclitaxel in the other cell lines. In particular, adding 250 nM C75 changed the IC₅₀ for paclitaxel from 14.81 to 10.96, 7.02 to 2.28, and 12.84 to 8.64 for A549, HeLa, and HCT 116 cells, respectively (**Figure 25B**). It is important to note that the IC₅₀ for C75 is close to 400 nM for all three cell lines.

A

Taxol

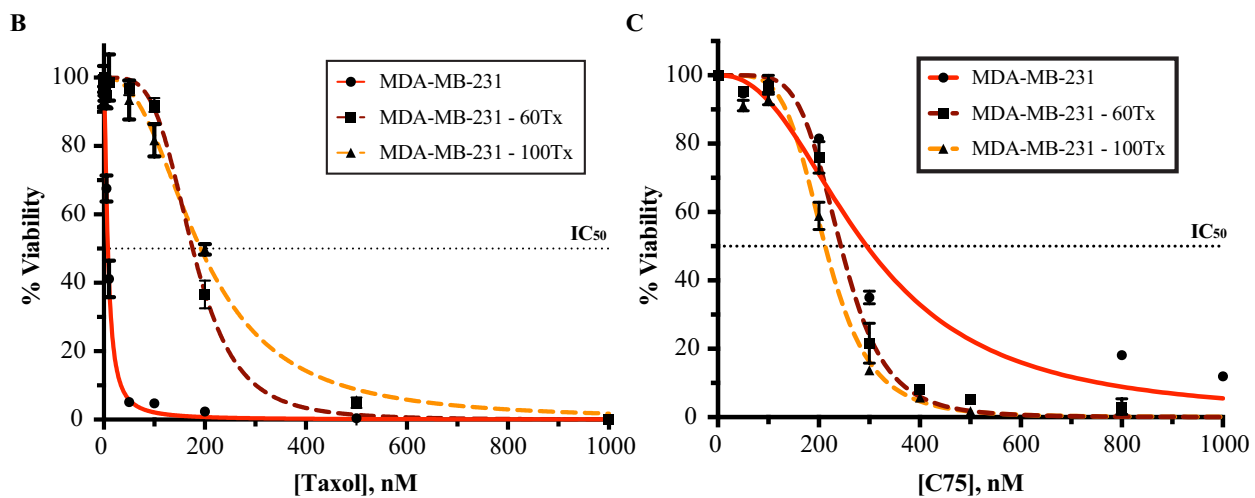
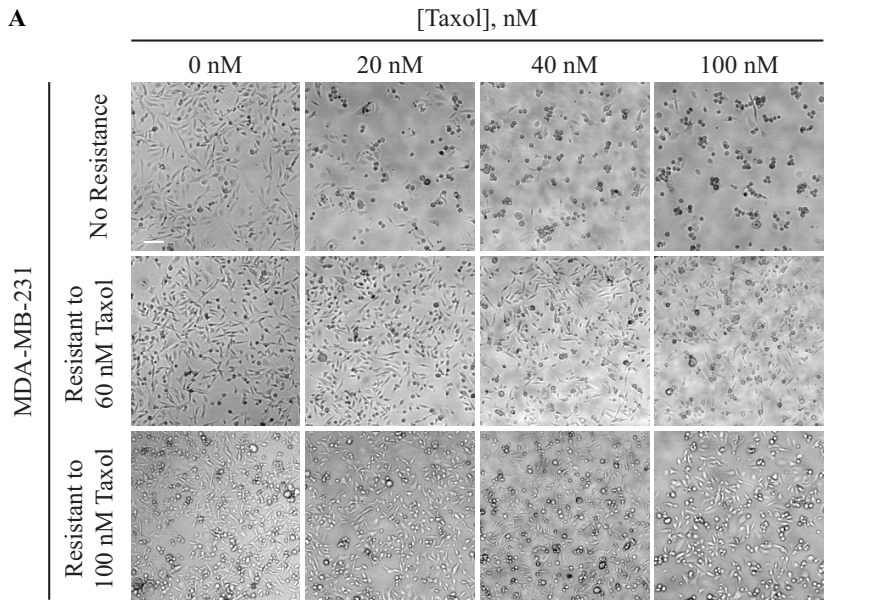


B

Cell Line	Viability IC ₅₀ , nM		
	C75	Taxol	Taxol + 250 nM C75
A549	377	14.81	10.96
HeLa	427	7.02	2.28
HCT 116	431	12.84	8.64
MDA-MB-231	255	1.68	TBD

Figure 25. A subthreshold dose of C75 lowers the IC₅₀ for Paclitaxel in different cell lines. A)

The molecular structure of Taxol is shown. **B)** A table shows the IC₅₀ values for different cell lines treated with C75, paclitaxel or a combination of both.



D

	IC ₅₀ , nM	
	C75	Taxol
MDA NR	294.6	8.02
MDA 60Tx	243.3	175.8
MDA 100Tx	212.6	191.8

Figure 26. Paclitaxel resistant cell line. **A)** A panel of images shows MDA-MB-231^{NR}, MDA-MB-231^{60Tx} and MDA-MB-231^{100Tx} cells after treatment with different concentrations of paclitaxel for 24 hours. The scale bar is 100 μ m. **B)** A line graph shows the % viability (Y-axis) of MDA-MB-231^{NR}, MDA-MB-231^{60Tx} and MDA-MB-231^{100Tx} cell lines after treatment with a range of Paclitaxel concentrations (X-axis) for 3 PDT. The IC₅₀ is indicated by the dotted line. **C)** A line graph shows the % viability (Y-axis) of MDA-MB-231^{NR}, MDA-MB-231^{60Tx} and MDA-MB-231^{100Tx} cell lines after treatment with a range of C75 concentrations (X-axis) for 3 PDT. The IC₅₀ is indicated by the dotted line. **D)** The table shows the IC₅₀ viability values for the graphs in **B)** and **C).**

This decrease shows that adding subthreshold amounts of C75 can indeed cause a stronger response to lower concentrations of paclitaxel. However, this needs to be done in TNBC cells. In MDA-MB-231 cells, the IC₅₀ for paclitaxel and C75 are 1.68 nM and 255 nM, respectively, and future studies will determine whether adding a sub-optimal concentration of C75 can reduce the viability of MDA-MB-231 cells when treated with a range of paclitaxel (**Figure 25B**).

Next, we generated MDA-MB-231 cells with varying levels of paclitaxel-resistance with the goal of testing changes in C75 efficacy in these cells. We created three heterogenous MDA-MB-231 cell lines that are resistant to 20, 60, and 100 nM paclitaxel, respectively (**Figure 26A**). Preliminary observations show that the overall morphology of MDA-MB-231 cells that are resistant to 60 and 100 nM paclitaxel (referred from now on as MDA^{60Tx} and MDA^{100Tx}, respectively) are similar to that of non-resistant MDA-MB-231 (MDA^{NR}) cells. Although there appears to be more rounded cells in the MDA^{100Tx} panel, these images were taken with a slightly different focal plane and are similar in appearance to the other cell lines. Treating the different cell lines with increasing concentrations of paclitaxel for 24 hours revealed that MDA^{NR} cells show reduced viability above 10 nM, while the MDA^{60Tx} cells showed reduced viability with 100 nM of paclitaxel, and MDA-MB-231^{100Tx} cells were not strongly impacted at any of the concentrations (**Figure 26A**). We then conducted a viability experiment on all three MDA cell lines treating them with either a range of Paclitaxel or C75 for 3 PDT (**Figure 26B, C**). When treated with Paclitaxel, the MDA^{NR} cells had an IC₅₀ of 8.02 nM, whereas both MDA^{60Tx} and MDA^{100Tx} cells had an IC₅₀ of 175.8 and 191.8 nM, respectively (**Figure 26D**). This revealed that both MDA^{60Tx} and MDA^{100Tx} cell lines are have a 22-24-fold increase in resistance to Taxol compared to the MDA^{NR} cell line. When MDA^{NR}, MDA^{60Tx} and MDA^{100Tx} were treated with C75 the IC₅₀ values were 294.6, 243.3 and 212.6 nM, respectively. This is interesting as it shows that C75 is most likely not

affected by the same mechanisms of resistance for Taxol found in the heterogenous population of these cell lines. Although speculative, there seems to be an inverse relationship between the cell lines with a higher resistance to Taxol and their IC₅₀ value when treated with C75.

Since the resistant cell lines were not generated clonally (*e.g.* have the same genetic changes), the heterogenous populations of cells could have accumulated several different changes that support resistance and some changes could also reduce C75 efficacy compared to others. A future experiment will clone individual cell lines to correlate changes in C75 efficacy with specific genetic changes.

5.3 Determining the changes in metabolic enzymes after C75 treatment

To better understand how C75 could react with enzymes *in vivo*, we conducted a metabolism study using extracted liver microsomes from mice. The goal of this assay is to identify the metabolites that are created when C75 is exposed to the liver microenvironment for metabolism and degradation. This helps us determine the reactivity of C75 and more specifically which chemical moiety is targeted by the liver during both phase 1 and 2 metabolism. The phase 1 metabolism is mainly done by cytochrome P450 (CYP) and phase 2 metabolism is done by UDP-glucuronosyl-transferase (UGT), sulfotransferase (SULT), glutathione-S-transferase (GST), *N*-acetyltransferase (NAT), and methyl-transferase (MT; **Muhamad and Na-Bangchang 2020**). In our first attempt at this assay we looked at metabolites generated in both phase 1 and phase 2 metabolism at 0- and 60-minutes using mice liver microsomes (MLM; **Figure 27A, B**). It revealed the metabolites and changes in C75 at both phases. This experiment will need to be repeated to see if they are consistently produced. The list of metabolites at 0 minutes can serve as a benchmark to compare changes in the concentrations of specific metabolites after 60-minutes. Phase 1

metabolites included stearyl and glutathione conjugations, while further modifications in phase 2 included the addition of a second glutathione moiety, as well as dehydration and methylation events. We need to repeat the experiment and calculate the concentrations of each metabolite to determine what proportion of the parent molecule (C75) is being converted into each identified metabolite.

This profiling will guide future modifications of the compound to retain stability and allow the molecule to remain biologically active for longer periods of time *in vivo*. In addition, we can identify any stable metabolites that might confer reactivity or toxicity, and guide modifications to the compound before its use *in vivo*.

A

Phase 1 Metabolites

0 minutes	Desaturation	-(H2)
	Desaturation, Nitro Reduction, GSH Conjugation 1	+(C10 H15 N3 O4 S)
	Oxidation, Oxidative Deamination to Ketone, Stearyl Conjugation	-(N) +(C18 H31 O3)
	Dehydration	-(H2)
	Oxidative Deamination to Ketone, Stearyl Conjugation	-(N) +(C18 H31 O3)
	Oxidation, Palmitoyl Conjugation	+(C15 H28 O2)
	Dehydration, Methylation	-(H2)
	Palmitoyl Conjugation	+(C15 H28 O2)
60 minutes	Hydration, Stearyl Conjugation	+(C18 H36 O2)
	Hydration, Oxidation, Stearyl Conjugation	+(C18 H36 O3)
	Reduction, Stearyl Conjugation	+(C18 H36 O2)
	Hydration, Stearyl Conjugation	+(C18 H36 O3)
	Thiourea to Urea, GSH Conjugation 1	+(C9 H13 N3 O7)
	Thiourea to Urea, GSH Conjugation 1	+(C9 H13 N3 O7)
	Reduction, Stearyl Conjugation	+(C18 H36 O3)

B

Phase 2 Metabolites

0 minutes	Desaturation	-(H2)
	Reduction, GSH Conjugation 2	+(C9 H17 N3 O7 S)
	Dehydration, Methylation	-(H2)
	Dehydration, Methylation	-(H2)
	Dehydration, Methylation	-(H2)
	Oxidative Deamination to Ketone, Oxidative Debromination	-(H2 Br N) +(O4)
	Oxidative Deamination to Ketone, Oxidative Debromination	-(H2 Br N) +(O4)
	Hydration, GSH Conjugation 2	+(C9 H17 N3 O7 S)
	Dehydration, GSH Conjugation 2	+(C10 H15 N3 O6 S)
	Dehydration	-(H2)
	Dehydration	-(H2)
	Dehydration, Desaturation, Palmitoyl Conjugation	+(C16 H26)
	GSH Conjugation 1	+(C10 H15 N3 O6 S)
	Desaturation, Nitro Reduction, GSH Conjugation 1	+(C10 H15 N3 O4 S)
60 minutes	Desaturation	-(H2)
	Desaturation	-(H2)
	Dehydration, Methylation	-(H2)
	Nitro Reduction, Oxidative Deamination to Ketone, GSH Conjugation 2	+(C10 H16 N2 O5 S)
	Reduction, GSH Conjugation 2	+(C9 H17 N3 O7 S)
	Hydration, GSH Conjugation 2	+(C9 H17 N3 O7 S)
	Dehydration, Methylation	-(H2)
	Thiourea to Urea, GSH Conjugation 1	+(C9 H13 N3 O7)
	GSH Conjugation 1	+(C10 H15 N3 O6 S)
	Dehydration	-(H2)

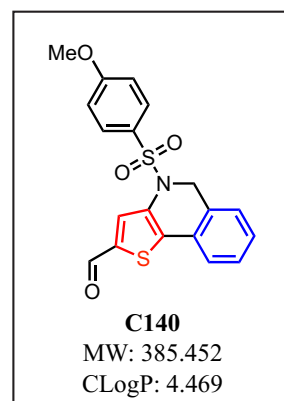
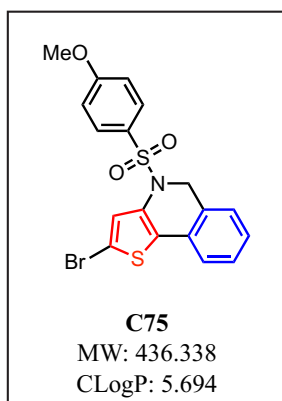
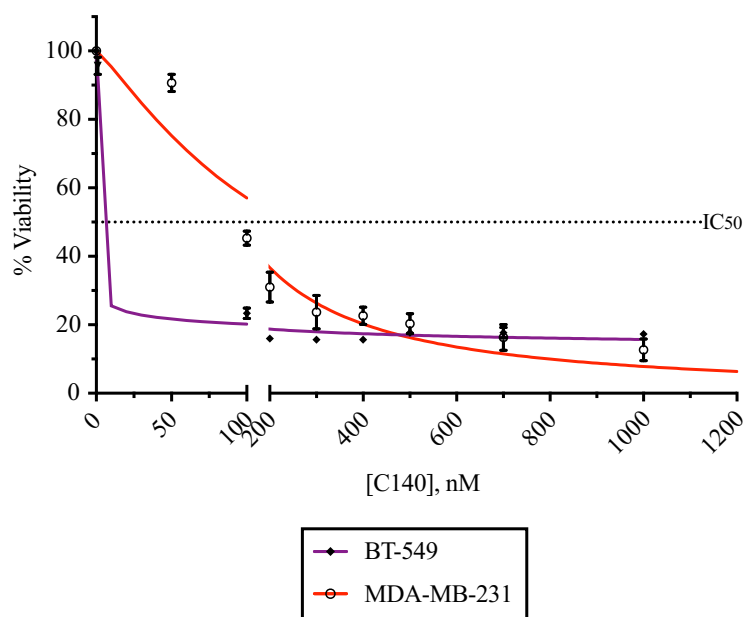
Figure 27. Metabolite profiles of C75. **A)** Tables show the metabolites generated during phase 1 metabolism of C75 after incubation with mice liver microsome (MLM) for 0 and 60 minutes. **B)** Tables show the metabolites generated during phase 2 metabolism of C75 after incubation with mice liver microsome (MLM) for 0 and 60 minutes. The chemical formulas indicate the addition or subtraction of that particular moiety on C75.

Future studies will aim to test other derivatives and conduct a comparative analysis to C75's metabolism profile to see which one yields favorable properties for *in vivo* use. The same study will also be done using human liver microsomes (HLM) to determine if the metabolism profiles of the MLMs differs from HLMs when C75 or another derivative is used. With the initiation of our *in vivo* studies on the pharmacokinetic and pharmacodynamic effects of C75 in mice, we will be able to obtain plasma samples from the mice over multiple timepoints allowing us to understand the compounds profile *in vivo*. With the data from this analysis, we can then compare the *in vitro* and *in vivo* studies to provide us with a clear understanding of how the compound is metabolized.

5.4 Finding new lead compounds

As mentioned in Chapter 3, we are using our high-throughput pipeline to identify new lead compounds with improved efficacy and selectivity. Ideally when moving to clinical studies, a lead compound should have efficacy that permits the use of low amounts of the drug for treatment. This depends on properties including solubility and metabolic reactivity. We recently found a derivative, C140, with improved properties and efficacy compared to C75. The structure of C140 in comparison to C75 is shown in **Figure 28A**. The main difference is an Oxygen vs. Bromine at the R3 position (**Figure 10A**). Although both are electron-withdrawing groups, Oxygen confers improved solubility, with a cLogP value of 4.469 for C140 vs. 5.694 for C75. The cLogP value describes the partition coefficient of a molecule in n-octanol/water, as a measure of its lipophilicity (**Ghose et al. 1998**). Ideally, cLogP values should be <5 because high lipophilicity could impact the solubility and bioavailability of a compound. Thus, the cLogP for C140 is more ideal vs. C75. In addition, the IC₅₀ values for C140 are 0.003 and 127 nM for BT-549 and MDA-MB-231 cells,

respectively vs. 185 and 263 nM for C75 (**Figure 28B, C**). However, the IC₅₀ for C140 in BT-549 cells requires additional experiments. This is due to the drastic change in viability between 0 nM and 100 nM. Thus, repeating the viability assay with a range of concentrations between 0 – 100 nM should provide a more accurate value. We are encouraged by the drop in IC₅₀ to close to or below 100 for two different TNBC cell lines. Further studies on solubility, permeability, and binding efficacy need to be done to understand how the chemistry is impacting the activity. If C140 has improved properties for *in vivo* use, it could potentially replace C75 as our lead compound.

A**B****C**

Cell Lines	Viability IC ₅₀ , nM
C140	
BT-549	0.003
MDA-MB-231	127

Figure 28. Identifying C140 as a new lead compound. **A)** The chemical structures of C75 and C140 are shown along with their molecular weight (MW) and CLogP values. **B)** A graph shows the viability curves of BT-549 (purple line) and MDA-MB-231 (red line) cells when treated with increasing concentrations of C140 for 3 population doubling times (PDT). The dotted line indicates the IC₅₀. **C)** The table indicates the IC₅₀ values for BT-549 and MDA-MB-231 cells when treated with C140.

Chapter 6: Discussion

6.1 Summary

This thesis describes a novel family of compounds with anti-cancer properties. This work originated from a collaboration with Dr. Forgione's lab who synthesized a thieonoisoquinoline scaffold amenable to modifications, which has the potential to probe molecular space and properties ideal for *in vivo* use. Of the initial derivatives, one caused reduced cancer cell viability prompting us to expand our partnership and design new derivatives. As described in Chapter 3, I developed a more robust methodology to screen these new derivatives and explore structure-activity-relationship (SAR) studies, which led us to identify our lead compound C75. Although our initial studies used HeLa and A549 cells, we also found that C75 has similar efficacy in other cancer cell lines (*e.g.* HCT 116), while it has lower efficacy in HFF-1 cells and normal patient-derived fibroblasts. Interestingly, its strongest effect seems to be in TNBC-derived cell lines (BT-549 and MDA-MB-231 cells), which is explored further in Chapter 5. In Chapter 3, I also found that increasing concentrations of C75 caused cancer cells to arrest in mitosis with defective spindles. I characterized this further in Chapter 4, where I performed additional analysis to show that C75 causes mitotic arrest and does not affect other stages of the cell cycle. Another student in the lab found that C75 disrupts microtubule polymerization *in vitro* and can compete with colchicine for tubulin-binding. This led me to compare the effects of C75 to colchicine in cells. Interestingly, while colchicine caused a reduction in microtubules and spindle pole collapse, C75 caused rapid microtubule loss, followed by fragmentation of the spindle poles, and microtubule repolymerization to form multipolar spindles. The spindle phenotype caused by C75 is similar to that caused by depletion of ch-TOG, a microtubule polymerase. Ch-TOG balances the activity of MCAK, a microtubule depolymerase to control microtubule length and organization, which is

over-expressed in several cancers. This suggests that C75 directly causes microtubule depolymerization, or indirectly does this by inhibiting ch-TOG causing ‘unchecked’ MCAK activity in cells. While these studies revealed the mechanism of action of C75 in cells, we also wanted to explore its commercial potential. As outlined in Chapter 5, our IC₅₀ data suggest that C75 has highest efficacy in TNBC cells. We imaged cells from different TNBCs (MDA-MB-231, Hs 578t cells) after treatment with C75 and determined that they have spindle phenotypes similar to other cancer cells, suggesting a similar mechanism of action. We also generated paclitaxel-resistant MDA-MB-231 cell lines that we will use to determine if C75 retains its efficacy, or if it is affected by the same mechanisms that give rise to paclitaxel resistance. Collectively, these and other studies are needed to help us test the ability of C75 to prevent or shrink TNBC-derived xenografts in mice. In addition, we are always designing and screening new derivatives with improved efficacy and selectivity that could be more suitable for *in vivo* use. We already identified C140, which has an improved cLogP (an indicator of solubility) and higher efficacy in TNBC cells compared to C75, and we are currently doing more studies to determine if this should become our new lead compound.

6.2 Developing high-throughput methodology

In Chapter 3, I describe a high-throughput pipeline that I developed for screening new derivatives. This methodology uses high-throughput instruments to increase the efficiency and accuracy of drug discovery. Although pharmaceutical companies rely on automated approaches to discover new chemical entities (NCE), they are less commonly used in academic labs due to limited accessibility to robots and other types of automated instrumentation. My main rationale for developing this pipeline was to take advantage of new technologies that recently became available

to researchers at Concordia and to render screening as independent as possible from human intervention. This automation increases speed and reduces human error, while creating a database of information on the screened molecules that is readily accessible. In my design, the first step was to automate cell culture dispensing into 96-well plates using the BioMek Liquid Handler. When done manually, pipetting errors can lead to the improper plating of cells and skew the experiment from its early stages. The second step involves using the ECHO Liquid Handler which can add minute, very precise volumes of compounds, saving both time and cost for the user. In addition to eliminating manual pipetting errors, this approach also permits the use of reduced volumes to limit the amount of solvent added to the cells and reduces waste. The third step allows the user to automate the acquisition of images of each well using the Nikon TiE microscope and stores these images into a user-friendly accessible database. The last step involves the use of macros to organize and present images, as well as numerical data, so that the user may spend more time on data analysis vs. organizing and processing. The current methodology has been of tremendous assistance in my work on drug discovery, although further optimization is possible. For example, improvements could be made to better integrate these steps into a single workflow, which should happen in the future as the University obtains additional infrastructure. Companies like Strateos are innovating high-throughput methodologies by building facilities capable of conducting large scale experiments remotely with input from the user via the cloud. This endeavour funded by Eli Lilly pharmaceuticals has brought us into a new era of streamlining biological experiments, and although it is currently quite costly, it likely will become more standard in the future.

6.3 Determining C75's mechanism of action in cells

In Chapter 4, we describe the mechanism of action of C75 in cultured human cells. C75 can compete with colchicine for the colchicine-binding pocket on tubulin and prevents microtubule polymerization *in vitro*. C75 causes reduced viability and mitotic arrest due to the formation of aberrant spindles similar to other microtubule-targeting drugs including colchicine. However, C75 has a different effect on microtubules in cells compared to colchicine. For example, in HeLa cells, colchicine causes a decrease in microtubules followed by gradual collapse of the spindle poles, and fragmentation of the poles is only observed after long periods of time (e.g. hours vs. minutes). However, C75 causes a decrease in microtubules and spindle pole fragmentation within minutes, followed by microtubule polymerization. We also observed that tubulin or ch-TOG at the spindle poles oscillate during recovery, leading to the formation of disorganized spindles. In support of their different spindle phenotypes, combining C75 and colchicine synergistically reduce cell viability and enhance spindle phenotypes when used at low concentrations.

Our findings shed some light on the mechanism of action of C75 and how it affects microtubules in cells. The spindle phenotypes are similar to those caused by the depletion of ch-TOG, which is a microtubule polymerase (**Gergely et al. 2003; Brouhard et al. 2008; Barr and Bakal 2015**). Many MAPs work together to form functional, bipolar spindles (**Petry 2016**). The loss of ch-TOG presumably causes an imbalance in the activities of other enzymes, including the microtubule depolymerase MCAK. Functions for MCAK include destabilizing microtubule ends to correct kinetochore attachments, which is controlled by Aurora B kinase phosphorylation, and focusing the asters into spindle poles via Aurora A kinase phosphorylation (**Andrews et al. 2004; Ems-McClung et al. 2013; Walczak et al. 2013; Zhang et al. 2008**). Ch-TOG-depleted cells have phenotypes consistent with these roles including disorganized spindle poles and misaligned sister

chromatids (**Gergely et al. 2003**). We similarly observed the formation of disorganized spindles and misaligned chromosomes in C75-treated cells. Based on this we speculate that: 1) C75 binds to tubulin dimers in a way that causes depolymerization of microtubules but has a high off-rate and new polymers can form due to local increases in the critical concentration of free tubulin, and/or, 2) C75 disrupts the microtubule or tubulin-binding site(s) of ch-TOG, mimicking ch-TOG loss-of-function. Ch-TOG has multiple TOG domains that associate with tubulin dimers to mediate their assembly into polymers, as well as a basic region that can mediate interactions with the microtubule lattice (**Widlund et al. 2011; Brouhard et al. 2008**). In support of this, we observed the accumulation and oscillation of ch-TOG between spindle poles in C75-treated cells, which could reflect the displacement of ch-TOG from microtubules or tubulin. In addition, the spindle phenotypes caused by C75 are restricted to metaphase, which could reflect its inhibition of an enzyme like ch-TOG with a similar window of requirement. Future studies will aim to perform a time-resolved experiment with purified ch-TOG and microtubule seeds in the presence and absence of C75. This will allow us to measure the change in microtubule dynamic and to test whether delocalization of ch-TOG at the plus-end of the microtubule arrests growth and/or causes depolymerization when C75 is present. It will be important to further dissect this mechanism and compare it to other well-known MTAs (i.e., colchicine, combrestatin A4, vinblastine), which will also help understand the critical requirement of ch-TOG in cancer cells that show an increased dependence on the polymerase.

Another microtubule-targeting compound, vinblastine, similarly has complex effects on microtubules which could contribute to its success as an anti-cancer drug. *In vitro*, vinblastine causes depolymerization at the minus ends, and prevents growth at the plus ends (**Panda et al. 1996**). In cells, 2 or 10 nM of vinblastine treatment causes disengagement of the mother and

daughter centrioles and altered ultra-architecture of centrioles, or reduced microtubule dynamics and multipolar spindles, respectively (**Jordan et al. 1992; Levrier et al. 2017; Wendell et al. 1993**). We propose that C75 shares some similarities with vinblastine with an accessibility and/or binding kinetics that favors microtubule depolymerization at the minus ends. But this accessibility appears to be restricted to cells in metaphase, as cells in other stages of the cell cycle do not appear to be affected at similar concentrations.

Vinblastine is one of the few microtubule-destabilizing drugs that has been successful in the clinic as an anti-cancer therapy. There are many factors that impact how well a compound functions *in vivo*, and it is difficult to know what concentrations are reached at the target cells (**Hughes et al. 2011**). The ability of vinblastine to cause spindle phenotypes at very low concentrations without disrupting the microtubule polymer mass could be ideal for minimizing side-effects. While C75 has a high IC₅₀ value by comparison (in the 300-400 nM range for HeLa, HCT 116 and A549 cells), its unique effect on microtubules and high selectivity for metaphase cells could make it an interesting compound to consider for *in vivo* use. Importantly, the design of our compound is such that the scaffold is amenable to modifications at three different sites, and we are constantly making new derivatives with improved IC₅₀ values and solubility that would replace C75 as our lead.

C75 causes spindle pole fragmentation prior to the oscillation of tubulin and ch-TOG at spindle poles. Centrosome integrity has been shown to rely on a TACC3-Clathrin-ch-TOG complex, and many microtubule-targeting drugs lead to the fragmentation of spindle poles, although this typically occurs after an extended period of time likely partly due to mitotic delay (e.g. hours; **Foraker et al. 2012; M. A. Jordan, Thrower, and Wilson 1992; Karki, Keyhaninejad, and Shuster 2017**). As mentioned above, low concentrations of vinblastine cause

disengagement of mother-daughter centrioles. In addition, cancer cells with high aneuploidy and amplified centrosomes typically rely on centrosome clustering mechanisms to form bipolar spindles (Leber et al. 2010; Ogden et al. 2012; Sabat-Pospiech et al. 2019). C75 may promote de-clustering and loss of centrosome integrity as visualized by γ -tubulin and centrin-2 staining, making it an attractive compound to explore for the treatment of cancers with supernumerary centrosomes (Sabat-Pospiech et al. 2019). Indeed, different cancer cell lines have different proportions of cells with multipolar spindles after C75 treatment, presumably due to different genetic changes in their background including those that could impact centrosome integrity, clustering and/or microtubule dynamics. We saw an increase in the proportion of A549 and HeLa cells with multipolar spindles, even at lower concentrations, suggesting that they are susceptible to de-clustering or fragmentation. Interestingly, we saw an increase in the proportion of HCT 116 cells with monopolar spindles at lower concentrations. With increased expression of Aurora A kinase and ch-TOG, these cells have increased assembly rates that could suppress C75 at lower concentrations (Ertynch et al. 2014). The tendency of spindle poles to move closer together was observed in other cell types, but only after extensive microtubule depolymerization. Identifying specific genetic changes and correlating these with amplified centrosomes or altered microtubule dynamics or regulation could predict how cells respond to C75-treatment.

6.4 Exploring the potential of our new compounds for *in vivo* use to treat TNBCs

In Chapter 5, we explored the potential application for our new anti-cancer compounds *in vivo*. As mentioned earlier, C75 has the highest efficacy in TNBCs (BT-549 and MDA-MB-231 cells), suggesting that our compounds could be ideal to treat TNBCs. As with most cancers,

TNBCs have accumulated a plethora of mutations and it will be interesting to test C75 or a lead compound in additional TNBC cell lines, and then compare the genomic profiles of the most sensitive cell types to determine which genetic changes they share. This kind of genetic profiling could predict which cancers to target using our compounds in the clinic. We observed that C75 causes the same range of spindle phenotypes in MDA-MB-231 and Hs 578t cells, suggesting that it has a similar mechanism of action in TNBC cells as in HeLa and A549 cells (*e.g.* Chapters 3 and 4). For example, Hs 578t cells display an increase in severity of multipolar/fragmented spindles with higher concentrations of C75. Although the data is preliminary, we will continue to explore C75's efficacy and mechanism of action in TNBC cells.

Taxol is commonly used to treat TNBCs, but repeated use can cause resistance. Therefore, it is important to determine if our compounds work in combination with Taxol and retain efficacy in Taxol-resistant cells. While we have not analyzed the data for MDA-MB-231 cells, we found that adding a sub-threshold concentration of C75 lowered the IC₅₀ for paclitaxel in A549, HeLa and HCT 116 cells. Furthermore, to understand how C75 efficacy is altered in paclitaxel-resistant TNBC cells, we successfully developed MDA-MB-231 cell lines that are resistant to 60 or 100 nM of paclitaxel. We then conducted a viability experiment using the paclitaxel resistant cell lines where they were treated with either paclitaxel or C75. The IC₅₀ values showed that both MDA^{60Tx} and MDA^{100Tx} had a much higher IC₅₀ value compared to the non-resistant counterpart. Although this was not the case with the C75 treatment, where both paclitaxel resistant cell lines had a similar IC₅₀ value to the non-resistant counterpart. Future studies will aim to create clonal lines derived from individual cells to identify more specific genetic changes that impact C75 efficacy by genomic sequencing, RNA seq and/or mass spectrometry. We predict that some of the genetic changes that commonly give rise to Taxol-resistance would not impact C75 efficacy. These include

1) specific mutations that make Taxol unable to bind to microtubules, since C75 binds to a different site, 2) the upregulation of alternate tubulin isoforms (e.g. β III-tubulin) which increase microtubules dynamics, since it retains the C75-binding site, and C75 destabilizes microtubules and would make them worse, and 3) the upregulation of drug efflux pumps that are more specific to some compounds vs. others (**Borges-Walmsley et al. 2003; O'Reilly et al. 2015; Eckford and Sharom 2009**).

From our preliminary metabolic studies, we identified metabolites related to a phase 1 and phase 2 metabolism using mice liver microsomes. This study will need to be repeated and have each metabolite quantified so that we may classify each as a major and minor metabolite. This will complement our *in vivo* studies that will be conducted in mice and allow us to draft a pharmacokinetic (PK) profile of C75. The PK data will give us an understanding on how well the molecule is absorbed, distributed, metabolized, and excreted (ADME) inside the live model and with our *in vitro* data we will know what metabolites to pay attention to and what to expect as well. Given that the *in vivo* model is more complex than our *in vitro* assay it is possible that we see a different metabolite profile altogether since they will be exposed to the vascular system of the mice and could react with factors such as albumin in the plasma, for example. This is speculative as only the live experiment will tell us what to pay attention to and in turn help us with any chemical modifications to better the compound's biological activity. Another important reason for conducting *in vitro* metabolism assay is to compare the metabolite profile of MLM versus human liver microsome (HLM) because it will shed light on potential differences between both models and any possible variations to expect. This will also influence the chemistry and through these cost-effective *in vitro* assays we will be in a better position to setup future *in vivo* studies.

Although we used C75 for the majority of our studies we are constantly generating new derivatives, and recently identified C140, with an IC₅₀ of 0.003 and 127 nM for BT-549 and MDA-MB-231 cells, respectively vs. 185 and 263 nM for C75. While 0.003 nM sounds incredible, it is inaccurate because we did not have concentrations of C140 below 100 nM in our IC₅₀ assay. It is likely that the IC₅₀ for C140 is below 100, but above 10 nM. Regardless, this increase in potency is encouraging as it is closer to the IC₅₀ for drugs that are currently used in the clinic (*e.g.* Taxol, vinblastine). Future studies will include repeating the viability assay to refine the IC₅₀ for C140 in BT-549 cells, and to determine the IC₅₀ in other TNBC cells as well as in other non-TNBC cells to assess selectivity. We also will perform the IC₅₀ assays in the paclitaxel-resistant MDA-MB-231 cells and verify that C140 has the same mechanism of action in cells as C75. If C140 has improved efficacy and selectivity, and a similar mechanism of action then it will replace C75 as our lead compound and we will proceed with *in vivo* studies.

6.5 Conclusions

There is a need to find new treatments for cancers. With only a handful of drugs that are commonly used, patients often gain resistance to these drugs leaving them with few alternatives. The most successful treatments were identified many decades ago, the majority of which were natural compounds derived from plants or trees. In addition to having limited quantities, these molecules are complex and difficult to modify (*e.g.* to improve solubility and other properties for *in vivo* use). In the last 20 years, there was a swing in the pharmaceutical industry to develop targeted therapies, where a potentially ideal molecule was identified, and compounds were synthesized to specifically alter its function. However, we now understand that most cancers are incredibly complex with extreme heterogeneity and a plethora of genetic changes that they

accumulate through progression. Thus, it is not surprising that the majority of these targeted therapies failed during clinical trials. We synthesized a new family of compounds amenable to modifications, and capable of probing molecular spaces, and returned to the idea that biology should dictate the most suitable candidates. This approach eliminates the assumption that a predetermined molecular target is the most ideal candidate, and we can modify compounds to improve their properties before moving them to the clinic. In addition, our in-depth studies of their mechanism of action in cells can help us better understand why some cancers could be more ideal to target compared to others. This time spent profiling cancers that are most suitable to target with our (lead) compounds should ensure that they have the best chance of success during trials. This emphasis on the earlier stages of testing should reduce the cost burden associated with clinical trials.

References

- Al-Bassam, Jawdat, and Fred Chang. 2011. “Regulation of Microtubule Dynamics by TOG-Domain Proteins XMAP215/Dis1 and CLASP.” *Trends in Cell Biology* 21 (10): 604–14. <https://doi.org/10.1016/j.tcb.2011.06.007>.
- Alqahtani, Fulwah Yahya, Fadilah Sfouq Aleanizy, Eram El Tahir, Hamad M. Alkahtani, and Bushra T. AlQuadeib. 2019. “Paclitaxel.” *Profiles of Drug Substances, Excipients and Related Methodology* 44: 205–38. <https://doi.org/10.1016/bs.podrm.2018.11.001>.
- Andrews, Paul D., Yulia Ovechkina, Nick Morrice, Michael Wagenbach, Karen Duncan, Linda Wordeman, and Jason R. Swedlow. 2004. “Aurora B Regulates MCAK at the Mitotic Centromere.” *Developmental Cell* 6 (2): 253–68. [https://doi.org/10.1016/S1534-5807\(04\)00025-5](https://doi.org/10.1016/S1534-5807(04)00025-5).
- Aysola, Kartik, Akshata Desai, Crystal Welch, Jingyao Xu, Yunlong Qin, Vaishali Reddy, Matthews Roland, et al. 2014. “Triple Negative Breast Cancer – An Overview.” *Proceedings of the National Academy of Sciences of the United States of America* 98 (19): 10869–74. <https://doi.org/10.4172/2161-1041.S2-001.Triple>.
- Barr, A. R., and F. Gergely. 2008. “MCAK-Independent Functions of Ch-Tog/XMAP215 in Microtubule Plus-End Dynamics.” *Molecular and Cellular Biology* 28 (23): 7199–7211. <https://doi.org/10.1128/mcb.01040-08>.
- Barr, Alexis R., and Fanni Gergely. 2007. “Aurora-A: The Maker and Breaker of Spindle Poles.” *Journal of Cell Science* 120 (17): 2987–96. <https://doi.org/10.1242/jcs.013136>.
- Barr, Alexis R., and Chris Bakal. 2015. “A Sensitised RNAi Screen Reveals a Ch-TOG Genetic Interaction Network Required for Spindle Assembly.” *Scientific Reports* 5 (April): 10564. <https://doi.org/10.1038/srep10564>.
- Barros, Teresa P., Kazuhisa Kinoshita, Anthony A. Hyman, and Jordan W. Raff. 2005. “Aurora A Activates D-TACC-MspS Complexes Exclusively at Centrosomes to Stabilize Centrosomal Microtubules.” *Journal of Cell Biology* 170 (7): 1039–46. <https://doi.org/10.1083/jcb.200504097>.
- Bhattacharyya, B, and J Wolff. 1974. “Promotion of Fluorescence upon Binding of Colchicine to Tubulin” 71 (7): 2627–31.
- Booth, Daniel G., Fiona E. Hood, Ian A. Prior, and Stephen J. Royle. 2011. “A TACC3/Ch-

- TOG/Clathrin Complex Stabilises Kinetochore Fibres by Inter-Microtubule Bridging.” *EMBO Journal* 30 (5): 906–19. <https://doi.org/10.1038/emboj.2011.15>.
- Borges-Walmsley, M. Ines, Kenneth S. McKeegan, and Adrian R. Walmsley. 2003. “Structure and Function of Efflux Pumps That Confer Resistance to Drugs.” *Biochemical Journal* 376 (2): 313–38. <https://doi.org/10.1042/BJ20020957>.
- Borisy, G. G., and E. W. Taylor. 1967a. “The Mechanism of Action of Colchicine. Binding of Colchicine-3H to Cellular Protein.” *The Journal of Cell Biology* 34 (2): 525–33. <https://doi.org/10.1083/jcb.34.2.525>.
- Borisy, G. G., and E. W. Taylor. 1967b. “The Mechanism of Action of Colchicine. Colchicine Binding to Sea Urchin Eggs and the Mitotic Apparatus.” *The Journal of Cell Biology* 34 (2): 535–48. <https://doi.org/10.1083/jcb.34.2.535>.
- Bray, Freddie, Jacques Ferlay, Isabelle Soerjomataram, Rebecca L. Siegel, Lindsey A. Torre, and Ahmedin Jemal. 2018. “Global Cancer Statistics 2018: GLOBOCAN Estimates of Incidence and Mortality Worldwide for 36 Cancers in 185 Countries.” *CA: A Cancer Journal for Clinicians* 68 (6): 394–424. <https://doi.org/10.3322/caac.21492>.
- Brinkley, William Bill R. 2016. “Supernumerary Centrosomes and Cancer : Boveri ’ s Hypothesis Revisited Views and Reviews Supernumerary Centrosomes and Cancer : Boveri ’ s Hypothesis Resurrected” 0169 (January 1998). [https://doi.org/10.1002/\(SICI\)1097-0169\(1998\)41](https://doi.org/10.1002/(SICI)1097-0169(1998)41).
- Brouhard, Gary J., Stear, Jeffrey H., Noetzel, Tim L. 2008. “XMAP215 Is a Processive Microtubule Polymerase.” *Growth (Lakeland)* 23 (1): 1–7. <https://doi.org/10.1038/jid.2014.371>.
- Brouhard, Gary J., and Luke M. Rice. 2018. “Microtubule Dynamics: An Interplay of Biochemistry and Mechanics.” *Nature Reviews Molecular Cell Biology* 19 (7): 451–63. <https://doi.org/10.1038/s41580-018-0009-y>.
- Byrnes, Amy E., and Kevin C. Slep. 2017. “TOG–Tubulin Binding Specificity Promotes Microtubule Dynamics and Mitotic Spindle Formation.” *The Journal of Cell Biology*. <http://jcb.rupress.org/content/early/2017/05/15/jcb.201610090>.
- Chamchoy, Kamonwan, Danaya Pakotiprapha, Pornpan Pumirat, Ubolsree Leartsakulpanich, and Usa Boonyuen. 2019. “Application of WST-8 Based Colorimetric NAD(P)H Detection for Quantitative Dehydrogenase Assays.” *BMC Biochemistry* 20 (1): 1–14.

- <https://doi.org/10.1186/s12858-019-0108-1>.
- Cheang, Maggie C U, David Voduc, Chris Bajdik, Samuel Leung, Steven McKinney, Stephen K. Chia, Charles M. Perou, and Torsten O. Nielsen. 2008. “Basal-like Breast Cancer Defined by Five Biomarkers Has Superior Prognostic Value than Triple-Negative Phenotype.” *Clinical Cancer Research* 14 (5): 1368–76. <https://doi.org/10.1158/1078-0432.CCR-07-1658>.
- Chen, Fei, Nicholas W.Y. Wong, and Pat Forgione. 2014. “One-Pot Tandem Palladium-Catalyzed Decarboxylative Cross-Coupling and C-H Activation Route to Thienoisoquinolines.” *Advanced Synthesis and Catalysis* 356 (8): 1725–30. <https://doi.org/10.1002/adsc.201300924>.
- Chou, Ting Chao. 2010. “Drug Combination Studies and Their Synergy Quantification Using the Chou-Talalay Method.” *Cancer Research* 70 (2): 440–46. <https://doi.org/10.1158/0008-5472.CAN-09-1947>.
- Cirillo, Luca, Monica Gotta, and Patrick Meraldi. 2017. *Cell Division Machinery and Disease*. Vol. 1002. <https://doi.org/10.1007/978-3-319-57127-0>.
- Conduit, Paul T, Alan Wainman, and Jordan W Raff. 2015. “Centrosome Function and Assembly in Animal Cells.” *Nature Reviews. Molecular Cell Biology* 16 (10): 611–24. <https://doi.org/10.1038/nrm4062>.
- Consolati, Tanja, Julia Locke, Johanna Roostalu, Zhuo Angel Chen, Julian Gannon, Jayant Asthana, Wei Ming Lim, et al. 2020. “Microtubule Nucleation Properties of Single Human GTuRCs Explained by Their Cryo-EM Structure.” *Developmental Cell* 53 (5): 603-617.e8. <https://doi.org/10.1016/j.devcel.2020.04.019>.
- Cronk, David. 2013. *High-Throughput Screening. Drug Discovery and Development: Technology in Transition*. Second Edi. Elsevier Ltd. <https://doi.org/10.1016/B978-0-7020-4299-7.00008-1>.
- Cutts, J. H., C. T. Beer, and R. L. Noble. 1960. “Biological Properties of Vincaleukoblastine, an Alkaloid in Vinca Rosea Linn, with Reference to Its Antitumor Action.” *Cancer Research* 20 (7): 1023–31.
- Dhamodharan, Rama, Mary Ann Jordan, Douglas Thrower, Leslie Wilson, and Patricia Wadsworth. 1995. “Vinblastine Suppresses Dynamics of Individual Microtubules in Living Interphase Cells.” *Molecular Biology of the Cell* 6 (9): 1215–29.

- [https://doi.org/10.1091/mbc.6.9.1215.](https://doi.org/10.1091/mbc.6.9.1215)
- Dominguez-Brauer, Carmen, Kelsie L. Thu, Jacqueline M. Mason, Heiko Blaser, Mark R. Bray, and Tak W. Mak. 2015. “Targeting Mitosis in Cancer: Emerging Strategies.” *Molecular Cell* 60 (4): 524–36. <https://doi.org/10.1016/j.molcel.2015.11.006>.
- Dumontet, Charles, and Mary Ann Jordan. 2010. “Microtubule-Binding Agents: A Dynamic Field of Cancer Therapeutics.” *Nature Reviews Drug Discovery* 9 (10): 790–803. <https://doi.org/10.1038/nrd3253>.
- Eckford, Paul D.W., and Frances J. Sharom. 2009. “ABC Efflux Pump-Based Resistance to Chemotherapy Drugs.” *Chemical Reviews* 109 (7): 2989–3011. <https://doi.org/10.1021/cr9000226>.
- Ems-McClung, Stephanie C., Sarah G. Hainline, Jenna Devare, Hailing Zong, Shang Cai, Stephanie K. Carnes, Sidney L. Shaw, and Claire E. Walczak. 2013. “Aurora B Inhibits MCAK Activity through a Phosphoconformational Switch That Reduces Microtubule Association.” *Current Biology* 23 (24): 2491–99. <https://doi.org/10.1016/j.cub.2013.10.054>.
- Ertych, Norman, Ailine Stoltz, Albrecht Stenzinger, Wilko Weichert, Silke Kaulfuß, Peter Burfeind, Achim Aigner, Linda Wordeman, and Holger Bastians. 2014. “Increased Microtubule Assembly Rates Influence Chromosomal Instability in Colorectal Cancer Cells.” *Nature Cell Biology* 16 (8): 779–91. <https://doi.org/10.1038/ncb2994>.
- Ferlay, J., M. Colombet, I. Soerjomataram, C. Mathers, D. M. Parkin, M. Piñeros, A. Znaor, and F. Bray. 2019. “Estimating the Global Cancer Incidence and Mortality in 2018: GLOBOCAN Sources and Methods.” *International Journal of Cancer* 144 (8): 1941–53. <https://doi.org/10.1002/ijc.31937>.
- Field, Jessica J., Arun Kanakkanthara, and John H. Miller. 2015. “Microtubule-Targeting Agents Are Clinically Successful Due to Both Mitotic and Interphase Impairment of Microtubule Function.” *Bioorganic and Medicinal Chemistry* 22 (18): 5050–59. <https://doi.org/10.1016/j.bmc.2014.02.035>.
- Fielding, AB, S Lim, K Montgomery, I Dobreva, and S Dedhar. 2011. “A Critical Role of Integrin-Linked Kinase, Ch-TOG and TACC3 in Centrosome Clustering in Cancer Cells.” *Oncogene* 30 (5): 521–34. <https://doi.org/10.1038/onc.2010.431>.
- Fink, Marc Y., and Jerry E. Chipuk. 2013. “Survival of HER2-Positive Breast Cancer Cells: Receptor Signaling to Apoptotic Control Centers.” *Genes and Cancer* 4 (5–6): 187–95.

- <https://doi.org/10.1177/1947601913488598>.
- Fitzgerald, Thomas J. 1976. “Molecular Features of Colchicine Associated with Antimitotic Activity and Inhibition of Tubulin Polymerization.” *Biochemical Pharmacology* 25: 1383–87.
- Fong, Ka-Wing, Yuk-Kwan Choi, Jerome B. Rattner, and Robert Z. Qi. 2008. “CDK5RAP2 Is a Pericentriolar Protein That Functions in Centrosomal Attachment of the β -Tubulin Ring Complex.” *Molecular Biology of the Cell* 19 (1): 115–25. <https://doi.org/10.1091/mbc.E07>.
- Foraker, Amy B., Stéphane M. Camus, Timothy M. Evans, Sophia R. Majeed, Chih Ying Chen, Sabrina B. Taner, Ivan R. Corrêa, Stephen J. Doxsey, and Frances M. Brodsky. 2012. “Clathrin Promotes Centrosome Integrity in Early Mitosis through Stabilization of Centrosomal Ch-TOG.” *Journal of Cell Biology* 198 (4): 591–605. <https://doi.org/10.1083/jcb.201205116>.
- Fox, J. C., A. E. Howard, J. D. Currie, S. L. Rogers, and K. C. Slep. 2014. “The XMAP215 Family Drives Microtubule Polymerization Using a Structurally Diverse TOG Array.” *Molecular Biology of the Cell* 25 (16): 2375–92. <https://doi.org/10.1091/mbc.E13-08-0501>.
- Fry, Andrew M., Josephina Sampson, Caroline Shak, and Sue Shackleton. 2017. “Recent Advances in Pericentriolar Material Organization: Ordered Layers and Scaffolding Gels.” *F1000Research* 6 (0): 1622. <https://doi.org/10.12688/f1000research.11652.1>.
- Funk, Laura C., Lauren M. Zasadil, and Beth A. Weaver. 2016. “Living in CIN: Mitotic Infidelity and Its Consequences for Tumor Promotion and Suppression.” *Developmental Cell* 39 (6): 638–52. <https://doi.org/10.1016/j.devcel.2016.10.023>.
- Gaetz, Jedidiah, and Tarun M. Kapoor. 2004. “Dynein/Dynactin Regulate Metaphase Spindle Length by Targeting Depolymerizing Activities to Spindle Poles.” *Journal of Cell Biology* 166 (4): 465–71. <https://doi.org/10.1083/jcb.200404015>.
- Ganem, Neil J., and Duane A. Compton. 2004. “The KinI Kinesin Kif2a Is Required for Bipolar Spindle Assembly through a Functional Relationship with MCAK.” *Journal of Cell Biology* 166 (4): 473–78. <https://doi.org/10.1083/jcb.200404012>.
- Ganem, Neil J., Kristi Upton, and Duane A. Compton. 2005. “Efficient Mitosis in Human Cells Lacking Poleward Microtubule Flux.” *Current Biology* 15 (20): 1827–32. <https://doi.org/10.1016/j.cub.2005.08.065>.
- Gergely, Fanni, Viji M. Draviam, and Jordan W. Raff. 2003. “The Ch-TOG/XMAP215 Protein

- Is Essential for Spindle Pole Organization in Human Somatic Cells.” *Genes and Development* 17 (3): 336–41. <https://doi.org/10.1101/gad.245603>.
- Ghose, Arup K., Vellarkad N. Viswanadhan, and John J. Wendoloski. 1998. “Prediction of Hydrophobic (Lipophilic) Properties of Small Organic Molecules Using Fragmental Methods: An Analysis of ALOGP and CLOGP Methods.” *Journal of Physical Chemistry A* 102 (21): 3762–72. <https://doi.org/10.1021/jp980230o>.
- Gigant, Benoît, Chunguang Wang, Raimond B.G. Ravelli, Fanny Roussi, Michel O. Steinmetz, Patrick A. Curmi, André Sobel, and Marcel Knossow. 2005. “Structural Basis for the Regulation of Tubulin by Vinblastine.” *Nature* 435 (7041): 519–22. <https://doi.org/10.1038/nature03566>.
- Gonçalves, A., D. Braguer, K. Kamath, L. Martello, C. Briand, S. Horwitz, L. Wilson, and M. A. Jordan. 2001. “Resistance to Taxol in Lung Cancer Cells Associated with Increased Microtubule Dynamics.” *Proceedings of the National Academy of Sciences of the United States of America* 98 (20): 11737–41. <https://doi.org/10.1073/pnas.191388598>.
- Goodson, Holly V., and Erin M Jonasson. 2018. “Microtubules and Microtubule-Associated Proteins.”
- Gutierrez-Caballero, C., S. G. Burgess, R. Bayliss, and S. J. Royle. 2015. “TACC3-Ch-TOG Track the Growing Tips of Microtubules Independently of Clathrin and Aurora-A Phosphorylation.” *Biology Open* 4 (2): 170–79. <https://doi.org/10.1242/bio.201410843>.
- Hanahan, Douglas, and Robert A. Weinberg. 2011. “Hallmarks of Cancer: The next Generation.” *Cell* 144 (5): 646–74. <https://doi.org/10.1016/j.cell.2011.02.013>.
- Hara, Masatoshi, and Tatsuo Fukagawa. 2018. “Kinetochore Assembly and Disassembly during Mitotic Entry and Exit.” *Current Opinion in Cell Biology* 52: 73–81. <https://doi.org/10.1016/j.ceb.2018.02.005>.
- Hari, Malathi, Hailing Yang, Changqing Zeng, Martin Canizales, and Fernando Cabral. 2003. “Expression of Class III β-Tubulin Reduces Microtubule Assembly and Confers Resistance to Paclitaxel.” *Cell Motility and the Cytoskeleton* 56 (1): 45–56. <https://doi.org/10.1002/cm.10132>.
- Hayden, J. H., S. S. Bowser, and C. L. Rieder. 1990. “Kinetochores Capture Astral Microtubules during Chromosome Attachment to the Mitotic Spindle: Direct Visualization in Live Newt Lung Cells.” *Journal of Cell Biology* 111 (3): 1039–45.

- <https://doi.org/10.1083/jcb.111.3.1039>.
- Hayward, Daniel, Tatiana Alfonso-Pérez, and Ulrike Gruneberg. 2019. “Orchestration of the Spindle Assembly Checkpoint by CDK1-Cyclin B1.” *FEBS Letters* 593 (20): 2889–2907. <https://doi.org/10.1002/1873-3468.13591>.
- Heald, Rebecca, and Alexey Khodjakov. 2015. “Thirty Years of Search and Capture: The Complex Simplicity of Mitotic Spindle Assembly.” *Journal of Cell Biology* 211 (6): 1103–11. <https://doi.org/10.1083/jcb.201510015>.
- Holmfeldt, Per, Sonja Stenmark, and Martin Gullberg. 2004. “Differential Functional Interplay of TOGp/XMAP215 and the KinI Kinesin MCAK during Interphase and Mitosis.” *EMBO Journal* 23 (3): 627–37. <https://doi.org/10.1038/sj.emboj.7600076>.
- Hood, Fiona E., Samantha J. Williams, Selena G. Burgess, Mark W. Richards, Daniel Roth, Anne Straube, Mark Pfuhl, Richard Bayliss, and Stephen J. Royle. 2013. “Coordination of Adjacent Domains Mediates TACC3-Ch-TOG-Clathrin Assembly and Mitotic Spindle Binding.” *Journal of Cell Biology* 202 (3): 463–78. <https://doi.org/10.1083/jcb.201211127>.
- Horwitz, Susan Band. 1992. “Mechanism of Taxol.” *Cancer* 13 (April): 134–36.
- Hoyt, M. Andrew, Laura Totis, and B. Tibor Roberts. 1991. “S. Cerevisiae Genes Required for Cell Cycle Arrest in Response to Loss of Microtubule Function.” *Cell* 66 (3): 507–17. [https://doi.org/10.1016/0092-8674\(81\)90014-3](https://doi.org/10.1016/0092-8674(81)90014-3).
- Hughes, J. P., S. S. Rees, S. B. Kalindjian, and K. L. Philpott. 2011. “Principles of Early Drug Discovery.” *British Journal of Pharmacology* 162 (6): 1239–49. <https://doi.org/10.1111/j.1476-5381.2010.01127.x>.
- Hussain, Rashad, and Wendy B. Macklin. 2017. “Integrin-Linked Kinase (ILK) Deletion Disrupts Oligodendrocyte Development by Altering Cell Cycle.” *Journal of Neuroscience* 37 (2): 397–412. <https://doi.org/10.1523/JNEUROSCI.2113-16.2016>.
- Hyman, Anthony A. 2005. “Boveri Revisited.” *The EMBO Journal* 24 (6): 1104–10. <https://doi.org/10.1038/sj.emboj.7600583>.
- Hymowitz, Sarah G., and Shiva Malek. 2018. “Targeting the MAPK Pathway in RAS Mutant Cancers.” *Cold Spring Harbor Perspectives in Medicine* 8 (11): 1–16. <https://doi.org/10.1101/cshperspect.a031492>.
- Iqbal, Nida, and Naveed Iqbal. 2014. “Human Epidermal Growth Factor Receptor 2 (HER2) in Cancers: Overexpression and Therapeutic Implications.” *Molecular Biology International*

- 2014: 1–9. <https://doi.org/10.1155/2014/852748>.
- Izawa, Daisuke, and Jonathon Pines. 2015. “The Mitotic Checkpoint Complex Binds a Second CDC20 to Inhibit Active APC/C.” *Nature* 517 (7536): 631–34.
<https://doi.org/10.1038/nature13911>.
- Jang, Chang Young, Judith A. Coppinger, Akiko Seki, John R. Yates, and Guowei Fang. 2009. “Plk1 and Aurora A Regulate the Depolymerase Activity and the Cellular Localization of Kif2a.” *Journal of Cell Science* 122 (9): 1334–41. <https://doi.org/10.1242/jcs.044321>.
- Johnson, Warren C. 1948. “The Edwin Smith Surgical Papyrus.” *Journal of Chemical Education*, 318–21. https://doi.org/10.1007/978-3-642-61320-3_6.
- Jordan, M. A., D. Thrower, and L. Wilson. 1992. “Effects of Vinblastine, Podophyllotoxin and Nocodazole on Mitotic Spindles. Implications for the Role of Microtubule Dynamics in Mitosis.” *Journal of Cell Science* 102 (3): 401–16.
- Jordan, Mary, and Kathy Kamath. 2007. “How Do Microtubule-Targeted Drugs Work? An Overview.” *Current Cancer Drug Targets* 7 (8): 730–42.
<https://doi.org/10.2174/156800907783220417>.
- Kamath, Kathy, Leslie Wilson, Fernando Cabral, and Mary Ann Jordan. 2005. “BIII-Tubulin Induces Paclitaxel Resistance in Association with Reduced Effects on Microtubule Dynamic Instability.” *Journal of Biological Chemistry* 280 (13): 12902–7.
<https://doi.org/10.1074/jbc.M414477200>.
- Karki, Menuka, Neda Keyhaninejad, and Charles B. Shuster. 2017. “Precocious Centriole Disengagement and Centrosome Fragmentation Induced by Mitotic Delay.” *Nature Communications* 8 (May): 1–12. <https://doi.org/10.1038/ncomms15803>.
- Kavallaris, M., C. A. Burkhardt, and S. B. Horwitz. 1999. “Antisense Oligonucleotides to Class III β-Tubulin Sensitize Drug-Resistant Cells to Taxol.” *British Journal of Cancer* 80 (7): 1020–25. <https://doi.org/10.1038/sj.bjc.6690507>.
- Kawamura, Eiko, Andrew B. Fielding, Nagarajan Kannan, Aruna Balgi, Connie J. Eaves, Michel Roberge, and Shoukat Dedhar. 2013. “Identification of Novel Small Molecule Inhibitors of Centrosome Clustering in Cancer Cells.” *Oncotarget*. Impact Journals.
<http://www.impactjournals.com/oncotarget/index.php?journal=oncotarget&page=article&op=view&path%5B%5D=1198&path%5B%5D=1571>.
- Khodjakov, Alexey, Lily Copenagle, Michael B. Gordon, Duane A. Compton, and Tarun M.

- Kapoor. 2003. “Minus-End Capture of Preformed Kinetochore Fibers Contributes to Spindle Morphogenesis.” *Journal of Cell Biology* 160 (5): 671–83.
<https://doi.org/10.1083/jcb.200208143>.
- Kinoshita, Kazuhisa, Tim L. Noetzel, Laurence Pelletier, Karl Mechtler, David N. Drechsel, Anne Schwager, Mike Lee, Jordan W. Raff, and Anthony A. Hyman. 2005. “Aurora A Phosphorylation of TACC3/Maskin Is Required for Centrosome-Dependent Microtubule Assembly in Mitosis.” *Journal of Cell Biology* 170 (7): 1047–55.
<https://doi.org/10.1083/jcb.200503023>.
- Kline-Smith, Susan L., Alexey Khodjakov, Polla Hergert, and Claire E. Walczak. 2004. “Depletion of Centromeric MCAK Leads to Chromosome Congression and Segregation Defects Due to Improper Kinetochore Attachments.” *Molecular Biology of the Cell* 15 (March 2004): 1146–59. <https://doi.org/10.1091/mbc.E03-08-0581>.
- Kozielski, Frank. 2015. “Kinesins and Cancer.” *Kinesins and Cancer* 12 (August): 1–271.
<https://doi.org/10.1007/978-94-017-9732-0>.
- Kumar, Ashok, Parduman R. Sharma, and Dilip M. Mondhe. 2016. “Potential Anticancer Role of Colchicine-Based Derivatives: An Overview.” *Anti-Cancer Drugs* 28 (3): 250–62.
<https://doi.org/10.1097/CAD.0000000000000464>.
- Kumar, Pankaj, and Rupali Aggarwal. 2016. “An Overview of Triple-Negative Breast Cancer.” *Archives of Gynecology and Obstetrics* 293 (2): 247–69. <https://doi.org/10.1007/s00404-015-3859-y>.
- Lara-Gonzalez, Pablo, Frederick G. Westhorpe, and Stephen S. Taylor. 2012. “The Spindle Assembly Checkpoint.” *Current Biology* 22 (22): R966–80.
<https://doi.org/10.1016/j.cub.2012.10.006>.
- Lauren E Harrison, Marina Bleiler, and Charles Giardina. 2017. “A Look into Centrosome Abnormalities in Colon Cancer Cells, How They Arise and How They Might Be Targeted Therapeutically.” *Physiology & Behavior* 176 (12): 139–48.
<https://doi.org/10.1016/j.physbeh.2017.03.040>.
- Leber, Blanka, Bettina Maier, Florian Fuchs, Jing Chi, Phillip Riffel, Simon Anderhub, Ludmila Wagner, et al. 2010. “Proteins Required for Centrosome Clustering in Cancer Cells.” *Science Translational Medicine* 2 (33). <https://doi.org/10.1126/scitranslmed.3000915>.
- Lebok, Patrick, Melike Öztürk, Uwe Heilenkötter, Fritz Jaenicke, Volkmar Müller, Peter

- Paluchowski, Stefan Geist, et al. 2016. "High Levels of Class III β -Tubulin Expression Are Associated with Aggressive Tumor Features in Breast Cancer." *Oncology Letters* 11 (3): 1987–94. <https://doi.org/10.3892/ol.2016.4206>.
- Leung, Ying Ying, Laura Li Yao Hui, and Virginia B. Kraus. 2015. "Colchicine-Update on Mechanisms of Action and Therapeutic Uses." *Seminars in Arthritis and Rheumatism* 45 (3): 341–50. <https://doi.org/10.1016/j.semarthrit.2015.06.013>.
- Levrier, Claire, Martin C. Sadowski, Anja Rockstroh, Brian Gabrielli, Maria Kavallaris, Melanie Lehman, Rohan A. Davis, and Colleen C. Nelson. 2017. " 6α -Acetoxyanopterine: A Novel Structure Class of Mitotic Inhibitor Disrupting Microtubule Dynamics in Prostate Cancer Cells." *Molecular Cancer Therapeutics* 16 (1): 3–15. <https://doi.org/10.1158/1535-7163.MCT-16-0325>.
- Li, Rong, and Andrew W Murray. 1991. "Feedback Control of Mitosis in Budding Yeast." *Cell* 66 (Cell Press): 519–31. [https://doi.org/10.1016/0092-8674\(81\)90015-5](https://doi.org/10.1016/0092-8674(81)90015-5).
- Li, Xiaotong, and Bruce Nicklas. 1995. "Mitotic Forces Control a Cell-Cycle Checkpoint." *Nature*.
- Liu, Pingyu, Yijun Wang, and Xin Li. 2019. "Targeting the Untargetable KRAS in Cancer Therapy." *Acta Pharmaceutica Sinica B* 9 (5): 871–79. <https://doi.org/10.1016/j.apsb.2019.03.002>.
- Liu, Yi Rong, Yi Zhou Jiang, Xiao En Xu, Ke Da Yu, Xi Jin, Xin Hu, Wen Jia Zuo, et al. 2016. "Comprehensive Transcriptome Analysis Identifies Novel Molecular Subtypes and Subtype-Specific RNAs of Triple-Negative Breast Cancer." *Breast Cancer Research* 18 (1): 1–10. <https://doi.org/10.1186/s13058-016-0690-8>.
- Livshits, Zhanna, Rama B. Rao, and Silas W. Smith. 2014. "An Approach to Chemotherapy-Associated Toxicity." *Emergency Medicine Clinics of North America* 32 (1): 167–203. <https://doi.org/10.1016/j.emc.2013.09.002>.
- Lok, Tsun Ming, Yang Wang, Wendy Kaichun Xu, Siwei Xie, Hoi Tang Ma, and Randy Y.C. Poon. 2020. "Mitotic Slippage Is Determined by P31comet and the Weakening of the Spindle-Assembly Checkpoint." *Oncogene* 39 (13): 2819–34. <https://doi.org/10.1038/s41388-020-1187-6>.
- Manning, Amity L., Neil J. Ganem, Samuel F. Bakhoum, Michael Wagenbach, Linda Wordeman, and Duane A. Compton. 2007. "The Kinesin-13 Proteins Kif2a, Kif2b, and

- Kif2c/MCAK Have Distinct Roles during Mitosis in Human Cells.” *Molecular Biology of the Cell* 18 (August): 2970–79. <https://doi.org/10.1091/mbc.E07>.
- Mantovani, Fiamma, Licio Collavin, and Giannino Del Sal. 2019. “Mutant P53 as a Guardian of the Cancer Cell.” *Cell Death and Differentiation* 26 (2): 199–212. <https://doi.org/10.1038/s41418-018-0246-9>.
- Martínez-Alonso, Diego, and Marcos Malumbres. 2020. “Mammalian Cell Cycle Cyclins.” *Seminars in Cell and Developmental Biology*, no. March: 0–1. <https://doi.org/10.1016/j.semcdcb.2020.03.009>.
- Martino, Emanuela, Giuseppe Casamassima, Sonia Castiglione, Edoardo Cellupica, Serena Pantalone, Francesca Papagni, Marta Rui, Angela Marika Siciliano, and Simona Collina. 2018. “Vinca Alkaloids and Analogues as Anti-Cancer Agents: Looking Back, Peering Ahead.” *Bioorganic and Medicinal Chemistry Letters* 28 (17): 2816–26. <https://doi.org/10.1016/j.bmcl.2018.06.044>.
- Massarotti, Alberto, Antonio Coluccia, Romano Silvestri, Giovanni Sorba, and Andrea Brancale. 2012. “The Tubulin Colchicine Domain: A Molecular Modeling Perspective.” *ChemMedChem* 7 (1): 33–42. <https://doi.org/10.1002/cmdc.201100361>.
- Mcintosh, J Richard. 2018. “Mitosis.”
- Miller, Kimberly D, Rebecca L Siegel, Chun Chieh Lin, Angela B Mariotto, Joan L Kramer, Julia H Rowland, Kevin D Stein, Rick Alteri, and Ahmedin Jemal. 2016. “Cancer Treatment and Survivorship Statistics , 2016” 66 (4): 271–89. <https://doi.org/10.3322/caac.21349>.
- Mills, Julia, Murat Digicaylioglu, Arthur T. Legg, Clint E. Young, Sean S. Young, Alasdair M. Barr, Lauren Fletcher, Timothy P. O’Connor, and Shoukat Dedhar. 2003. “Role of Integrin-Linked Kinase in Nerve Growth Factor-Stimulated Neurite Outgrowth.” *Journal of Neuroscience* 23 (5): 1638–48. <https://doi.org/10.1523/jneurosci.23-05-01638.2003>.
- Mitchison, Tim, and Marc Kirschner. 1987. “Dynamic Instability of Microtubules.” *BioEssays* 7 (4): 149–54. <https://doi.org/10.1002/bies.950070403>.
- Mittal, Karuna, Da Hoon Choi, Sergey Klimov, Shrikant Pawar, Ramneet Kaur, Anirban K. Mitra, Meenakshi V. Gupta, et al. 2016. “A Centrosome Clustering Protein, KIFC1, Predicts Aggressive Disease Course in Serous Ovarian Adenocarcinomas.” *Journal of Ovarian Research* 9 (1): 1–11. <https://doi.org/10.1186/s13048-016-0224-0>.

- Monda, Julie K., and Iain M. Cheeseman. 2018. "The Kinetochore-Microtubule Interface at a Glance." *Journal of Cell Science* 131 (16). <https://doi.org/10.1242/jcs.214577>.
- Muhamad, Nadda, and Kesara Na-Bangchang. 2020. "Metabolite Profiling in Anticancer Drug Development: A Systematic Review." *Drug Design, Development and Therapy* 14: 1401–44. <https://doi.org/10.2147/DDDT.S221518>.
- Musacchio, Andrea. 2015. "The Molecular Biology of Spindle Assembly Checkpoint Signaling Dynamics." *Current Biology* 25 (20): R1002–18. <https://doi.org/10.1016/j.cub.2015.08.051>.
- Nedeljković, Milica, and Ana Damjanović. 2019. "Mechanisms of Chemotherapy Resistance in Triple-Negative Breast Cancer-How We Can Rise to the Challenge." *Cells* 8 (9). <https://doi.org/10.3390/cells8090957>.
- Nigg, Erich A, and Andrew J Holland. 2018. "Their Deregulation in Disease" 19 (5): 297–312. <https://doi.org/10.1038/nrm.2017.127.Once>.
- Nithianantham, Stanley, Brian D. Cook, Madeleine Beans, Fei Guo, Fred Chang, and Jawdat Al-Bassam. 2018. "Structural Basis of Tubulin Recruitment and Assembly by Microtubule Polymerases with Tumor Overexpressed Gene (TOG) Domain Arrays." *eLife* 7: 1–33. <https://doi.org/10.7554/eLife.38922>.
- Noble, R. L., C. T. Beer, and J. H. Cutts. 1958. "Role of Chance Observations in Chemotherapy: Vinca Rosea." *Ann. N.Y. Acad. Sci.* 76: 882–94. <https://doi.org/10.1111/j.1749-6632.1958.tb54906.x>.
- O'Reilly, Elma A., Luke Gubbins, Shiva Sharma, Riona Tully, Matthew Ho Zhing Guang, Karolina Weiner-Gorzel, John McCaffrey, et al. 2015. "The Fate of Chemoresistance in Triple Negative Breast Cancer (TNBC)." *BBA Clinical* 3: 257–75. <https://doi.org/10.1016/j.bbaci.2015.03.003>.
- Ogden, a, P C G Rida, and R Aneja. 2012. "Let's Huddle to Prevent a Muddle: Centrosome Declustering as an Attractive Anticancer Strategy." *Cell Death and Differentiation* 19 (8): 1255–67. <https://doi.org/10.1038/cdd.2012.61>.
- Oliveira, Claire de, Sharada Weir, Jagadish Rangrej, Murray D. Krahn, Nicole Mittmann, Jeffrey S. Hoch, Kelvin K.W. Chan, and Stuart Peacock. 2018. "The Economic Burden of Cancer Care in Canada: A Population-Based Cost Study." *CMAJ Open* 6 (1): E1–10. <https://doi.org/10.9778/cmajo.20170144>.
- Olmsted, Joanna B., and Gary G. Borisy. 1973. "Microtubules." *Annual Review of Biochemistry*,

507–40.

- Orr, George A., Pascal Verdier-Pinard, Hayley McDaid, and Susan Band Horwitz. 2003. “Mechanisms of Taxol Resistance Related to Microtubules.” *Oncogene* 22 (47 REV. ISS. 6): 7280–95. <https://doi.org/10.1038/sj.onc.1206934>.
- Panda, Dulal, Mary Ann Jordan, Kevin Chin Chu, and Leslie Wilson. 1996. “Differential Effects of Vinblastine on Polymerization and Dynamics at Opposite Microtubule Ends.” *Journal of Biological Chemistry* 271 (47): 29807–12. <https://doi.org/10.1074/jbc.271.47.29807>.
- Panda, Dulal, Herbert P. Miller, and Leslie Wilson. 2002. “Determination of the Size and Chemical Nature of the Stabilizing ‘Cap’ at Microtubule Ends Using Modulators of Polymerization Dynamics.” *Biochemistry* 41 (5): 1609–17. <https://doi.org/10.1021/bi011767m>.
- Petry, Sabine. 2016. “Mechanisms of Mitotic Spindle Assembly.” *Annu Rev Biochem.* 85 (1): 659–83. <https://doi.org/10.1146/annurev-biochem-060815-014528>.
- Pickett, S. D. 2006. *Library Design: Reactant and Product-Based Approaches. Comprehensive Medicinal Chemistry II.* Vol. 4. Elsevier Inc. <https://doi.org/10.1016/b0-08-045044-x/00257-1>.
- Pihan, German A. 2013. “Centrosome Dysfunction Contributes to Chromosome Instability, Chromoanagenesis, and Genome Reprograming in Cancer.” *Frontiers in Oncology* 3 NOV (November): 1–26. <https://doi.org/10.3389/fonc.2013.00277>.
- Rieder, C. L., and S. P. Alexander. 1990. “Kinetochores Are Transported Poleward along a Single Astral Microtubule during Chromosome Attachment to the Spindle in Newt Lung Cells.” *Journal of Cell Biology* 110 (1): 81–95. <https://doi.org/10.1083/jcb.110.1.81>.
- Rieder, Conly L., Richard W. Cole, Alexey Khodjakov, and Greenfield Sluder. 1995. “The Checkpoint Delaying Anaphase in Response to Chromosome Monoorientation Is Mediated by an Inhibitory Signal Produced by Unattached Kinetochores.” *Journal of Cell Biology* 130 (4): 941–48. <https://doi.org/10.1083/jcb.130.4.941>.
- Roostalu, Johanna, Nicholas I Cade, and Thomas Surrey. 2015. “Complementary Activities of TPX2 and ChTOG Constitute an Efficient Importin-Regulated Microtubule Nucleation Module,” no. August. <https://doi.org/10.1038/ncb3241>.
- Rudkouskaya, Alena, Ian Welch, and Lina Dagnino. 2014. “ILK Modulates Epithelial Polarity and Matrix Formation in Hair Follicles.” *Molecular Biology of the Cell* 25 (5): 620–32.

- <https://doi.org/10.1091/mbc.E13-08-0499>.
- Sabat-Pospiech, Dorota, Kim Fabian-Kolpanowicz, Ian A. Prior, Judy M. Coulson, and Andrew B. Fielding. 2019. “Targeting Centrosome Amplification, an Achilles’ Heel of Cancer.” *Biochemical Society Transactions* 47 (5): 1209–22. <https://doi.org/10.1042/BST20190034>.
- Sakai, Takao, Shaohua Li, Denitsa Docheva, Carsten Grashoff, Keiko Sakai, Günter Kostka, Attila Braun, Alexander Pfeifer, Peter D. Yurchenco, and Reinhard Fässler. 2003. “Integrin-Linked Kinase (ILK) Is Required for Polarizing the Epiblast, Cell Adhesion, and Controlling Actin Accumulation.” *Genes and Development* 17 (7): 926–40. <https://doi.org/10.1101/gad.255603>.
- Scheer, Ulrich. 2018. “Boveri’s Research at the Zoological Station Naples: Rediscovery of His Original Microscope Slides at the University of Würzburg.” *Marine Genomics* 40 (February): 1–8. <https://doi.org/10.1016/j.margen.2018.01.003>.
- Schenone, Monica, Bridget K Wagner, Paul A Clemons, and Biology Program. 2017. “Biology and Drug Discovery.” *Nature Chemical Biology* 9 (4): 232–40. <https://doi.org/10.1038/nchembio.1199.Target>.
- Shapiro, Paul. 2002. “Ras-MAP Kinase Signaling Pathways and Control of Cell Proliferation: Relevance to Cancer Therapy.” *Critical Reviews in Clinical Laboratory Sciences* 39 (4–5): 285–330. <https://doi.org/10.1080/10408360290795538>.
- Simanshu, Dhirendra K., Dwight V. Nissley, and Frank McCormick. 2017. “RAS Proteins and Their Regulators in Human Disease.” *Physiology & Behavior* 176 (1): 139–48. <https://doi.org/10.1016/j.physbeh.2017.03.040>.
- Smith, Leah, Shirley Bryan, Prithwish De, Rami Rahal, Amanda Shaw, Donna Turner, CancerCare Manitoba, Manitoba K Hannah Weir, Ryan Woods, and Monika Dixon. 2018. “Canadian Cancer Statistics Advisory Committee. Canadian Cancer Statistics 2018.” *Stroke*. <https://doi.org/2018>.
- Stengel, C., S. P. Newman, M. P. Leese, B. V.L. Potter, M. J. Reed, and A. Purohit. 2010. “Class III B-Tubulin Expression and in Vitro Resistance to Microtubule Targeting Agents.” *British Journal of Cancer* 102 (2): 316–24. <https://doi.org/10.1038/sj.bjc.6605489>.
- Taylor, Stephen S., Edward Ha, and Frank McKeon. 1998. “The Human Homologue of Bub3 Is Required for Kinetochore Localization of Bub1 and a Mad3/Bub1-Related Protein Kinase.” *Journal of Cell Biology* 142 (1): 1–11. <https://doi.org/10.1083/jcb.142.1.1>.

- Triplet, Van Oostende, Jaramillo Garcia, and Haji Bik. 2014. “Anillin Interacts with Microtubules and Is Part of the Astral Pathway That Defines Cortical Domains Running Title : Journal of Cell Science JCS Advance Online Article . Posted on 2 July 2014” 2 (July): 3699–3710. <https://doi.org/10.1242/jcs.147504>.
- Uehara, Ryota, Yuki Tsukada, Tomoko Kamasaki, Ina Poser, Kinya Yoda, Daniel W. Gerlich, and Gohta Goshima. 2013. “Aurora B and Kif2A Control Microtubule Length for Assembly of a Functional Central Spindle during Anaphase.” *Journal of Cell Biology* 202 (4): 623–36. <https://doi.org/10.1083/jcb.201302123>.
- Ungrecht, Rosemarie, and Ulrike Kutay. 2017. “Mechanisms and Functions of Nuclear Envelope Remodelling.” *Nature Reviews Molecular Cell Biology* 18 (4): 229–45. <https://doi.org/10.1038/nrm.2016.153>.
- Walczak, Claire E., Sophia Gayek, and Ryoma Ohi. 2013. “Microtubule-Depolymerizing Kinesins.” *Annual Review of Cell and Developmental Biology* 29: 417–41. <https://doi.org/10.1146/annurev-cellbio-101512-122345>.
- Wang, Yuxi, Hang Zhang, Benoît Gigant, Yamei Yu, Yangping Wu, Xiangzheng Chen, Qinhuai Lai, Zhaoya Yang, Qiang Chen, and Jinliang Yang. 2016. “Structures of a Diverse Set of Colchicine Binding Site Inhibitors in Complex with Tubulin Provide a Rationale for Drug Discovery.” *FEBS Journal* 283 (1): 102–11. <https://doi.org/10.1111/febs.13555>.
- Weaver, Beth A. 2014. “How Taxol/Paclitaxel Kills Cancer Cells.” *Molecular Biology of the Cell* 25 (18): 2677–81. <https://doi.org/10.1091/mbc.E14-04-0916>.
- Weigelt, Britta, Felipe C. Geyer, and Jorge S. Reis-Filho. 2010. “Histological Types of Breast Cancer: How Special Are They?” *Molecular Oncology* 4 (3): 192–208. <https://doi.org/10.1016/j.molonc.2010.04.004>.
- Wein, Lironne, and Sherene Loi. 2017. “Mechanisms of Resistance of Chemotherapy in Early-Stage Triple Negative Breast Cancer (TNBC).” *Breast* 34: S27–30. <https://doi.org/10.1016/j.breast.2017.06.023>.
- Wendell, K. L., L. Wilson, and M. A. Jordan. 1993. “Mitotic Block in HeLa Cells by Vinblastine: Ultrastructural Changes in Kinetochore-Microtubule Attachment and in Centrosomes.” *Journal of Cell Science* 104 (2): 261–74.
- Widlund, Per O., Jeffrey H. Stear, Andrei Pozniakovsky, Marija Zanic, Simone Reber, Gary J. Brouhard, Anthony A. Hyman, and Jonathon Howard. 2011. “XMAP215 Polymerase

- Activity Is Built by Combining Multiple Tubulin-Binding TOG Domains and a Basic Lattice-Binding Region.” *Proceedings of the National Academy of Sciences of the United States of America* 108 (7): 2741–46. <https://doi.org/10.1073/pnas.1016498108>.
- Wieduwilt, M. J., and M. M. Moasser. 2008. “The Epidermal Growth Factor Receptor Family: Biology Driving Targeted Therapeutics.” *Cellular and Molecular Life Sciences* 65 (10): 1566–84. <https://doi.org/10.1007/s00018-008-7440-8>.
- Willems, Estelle, Matthias Dedobbeleer, Marina Digregorio, Arnaud Lombard, Paul Noel Lumapat, and Bernard Rogister. 2018. “The Functional Diversity of Aurora Kinases: A Comprehensive Review.” *Cell Division* 13 (1): 1–17. <https://doi.org/10.1186/s13008-018-0040-6>.
- Wong, Chi Heem, Kien Wei Siah, and Andrew W. Lo. 2019. “Estimation of Clinical Trial Success Rates and Related Parameters.” *Biostatistics* 20 (2): 273–86. <https://doi.org/10.1093/biostatistics/kxx069>.
- Woodruff, Jeffrey B., Oliver Wueseke, and Anthony A. Hyman. 2014. “Pericentriolar Material Structure and Dynamics.” *Philosophical Transactions of the Royal Society B: Biological Sciences* 369 (1650). <https://doi.org/10.1098/rstb.2013.0459>.
- Wordeman, L., and T. J. Mitchison. 1995. “Identification and Partial Characterization of Mitotic Centromere- Associated Kinesin, a Kinesin-Related Protein That Associates with Centromeres during Mitosis.” *Journal of Cell Biology* 128 (1–2): 95–105. <https://doi.org/10.1083/jcb.128.1.95>.
- Xiao, Hui, Pascal Verdier-Pinard, Narcis Fernandez-Fuentes, Berta Burd, Ruth Angeletti, Andras Fiser, Susan Band Horwitz, and George A. Orr. 2006. “Insights into the Mechanism of Microtubule Stabilization by Taxol.” *Proceedings of the National Academy of Sciences of the United States of America* 103 (27): 10166–73. <https://doi.org/10.1073/pnas.0603704103>.
- Xu, Xu Feng, Ting Li, Dong Dong Wang, Bing Chen, Yue Wang, and Zhe Yu Chen. 2015. “Integrin-Linked Kinase Is Essential for Environmental Enrichment Enhanced Hippocampal Neurogenesis and Memory.” *Scientific Reports* 5 (January): 1–16. <https://doi.org/10.1038/srep11456>.
- Y.C.Poon, Randy. 2016. “Cell Cycle Control: A System of Interlinking Oscillators.” *Methods in Molecular Biology* 1342: pp 3-19. <https://doi.org/10.1007/978-1-4939-2957-3>.
- Yang, Chia Ping Huang, and Susan Band Horwitz. 2017. “Taxol®: The First Microtubule

- Stabilizing Agent.” *International Journal of Molecular Sciences* 18 (8).
<https://doi.org/10.3390/ijms18081733>.
- Yin, Li, Jiang Jie Duan, Xiu Wu Bian, and Shi Cang Yu. 2020. “Triple-Negative Breast Cancer Molecular Subtyping and Treatment Progress.” *Breast Cancer Research : BCR* 22 (1): 61.
<https://doi.org/10.1186/s13058-020-01296-5>.
- Yüce, Özlem, Alisa Piekny, and Michael Glotzer. 2005. “An ECT2-Centralspindlin Complex Regulates the Localization and Function of RhoA.” *Journal of Cell Biology* 170 (4): 571–82. <https://doi.org/10.1083/jcb.200501097>.
- Yusuf, R Z, Z Duan, D E Lamendola, R T Penson, and M V Seiden. 2003. “Paclitaxel Resistance: Molecular Mechanisms and Pharmacologic Manipulation.” *Current Cancer Drug Targets* 3: 1–19.
- Zasadil, Lauren M, Kristen A Andersen, Dabin Yeum, Gabrielle B Rocque, Lee G Wilke, Amye J Tevaarwerk, Ronald T Raines, Mark E Burkard, and Beth A Weaver. 2014. “Cytotoxicity of Paclitaxel in Breast Cancer Is Due to Chromosome Missegregation on Multipolar Spindles.” *Science Translational Medicine* 6 (229): 229ra43.
<https://doi.org/10.1126/scitranslmed.3007965>.
- Zhang, Xiaotian, Masakazu Yashiro, Hong Qiu, Takafumi Nishii, Taro Matsuzaki, and Kosei Hirakawa. 2010. “Establishment and Characterization of Multidrug-Resistant Gastric Cancer Cell Lines.” *Anticancer Research* 30 (3): 915–22.
- Zhang, Xin, Stephanie C. Ems-McClung, and Claire E. Walczak. 2008. “Aurora A Phosphorylates MCAK to Control Ran-Dependent Spindle Bipolarity.” *Molecular Biology of the Cell* 19 (July): 2752–65. <https://doi.org/10.1091/mbc.e08-02-0198>.